Department of Physics and Astronomy

University of Heidelberg

Master thesis

in Physics

submitted by

Alexander Baumgärtner

born in Freiburg im Breisgau

2017

A new apparatus for trapping and manipulating single Strontium atoms

This Master thesis has been carried out by

Alexander Baumgärtner

at the

California Insitute of Technology

under the supervision of

Prof. Markus Oberthaler

Ein neues Experiment zum Einfangen und Manipulieren von einzelnen Strontium Atomen

Das Zusammensetzen von großen Atomgittern aus einzelnen optischen Tweezern ist eine neue Möglichkeit um defektfreie Vielteilchensysteme zu konstruieren. Die in dieser Thesis vorgestellte Arbeit legt den Grundstein, um diese Technik mit Strontium zu demonstrieren.
Dafür wurde ein Vakuumsystem entwickelt, welches Atomlebensdauern von über 40 Sekunden ermöglicht, während weiterhin ein Atomfluss beibehalten wird, der Laderaten der Magneto-optischen Falle von 170 ms erreicht. Magneto-optische Fallen mit 2×10^8 Atomen sowie das abbilden ersten Atome in optischen Tweezern wurden bereits realisiert.
In weiteren Untersuchungen haben wir eine Methode entwickelt um Atome in optischen Tweezern zu kühlen. Dies ist ein wichtiger Schritt um ein robustes Abbilden der Atome zu gewährleisten, was eine wichtige Rolle beim Sortieren der Atome spielt.
Dies ist der Ausgangpunkt für zukünftige Untersuchungen mit dem Ziel Quantensysteme mit einem hohen Grad an Kontrolle zu erzeugen, welche noch nie dargewesene Systemgrößen von tausenden Atomen erreichen können.

A new apparatus for trapping and manipulating single Strontium atoms

The assembly of large-scale arrays of individual neutral atoms in optical tweezers is a recently-demonstrated technique to create defect-free many-body systems. This thesis outlines the foundation towards the first realization of this technique with Strontium atoms.
To this end we designed and built a vacuum setup which allows for long vacuum lifetimes (tens of second) while maintaining high atomic flux for fast loading of the magneto-optical trap at rates of up to 170 ms. With this apparatus, we realized magneto-optical traps with up to 2×10^8 atoms and demonstrated the imaging of Strontium atoms inside of optical tweezers for the first time.
Furthermore, we developed a cooling scheme that allows for imaging and cooling of Strontium atoms inside the optical tweezers. This is crucial for the further steps of the experiment, in which we aim to image the atoms multiple times in order to rearrange.
This is the starting point for future work towards a fully controllable quantum system with unprecedented system sizes of several thousand constituents.

Contents

1 Introduction

Through continuous improvements in the control over quantum systems, simulations of quantum many-body physics with control over single constituents has become a common goal for several experimental platforms [1–4]. In solid state systems such as superconducting quantum interference devices [5, 6] or semiconductor nanowires [7], the primary challenge remains to isolate mesoscopic structures from their environment to prevent decoherence. Alternatively, atomic systems consisting of ions or ultracold atoms serve as small quantum systems by definition. Here, the coherent control over single constituents (i.e. particles) and manipulation of their interactions poses a significant obstacle in this field.

For many years, rf Paul traps have served as a suitable platform for this task due to their robustness and strong interactions [8, 9]. The interplay of their motional degrees of freedom and internal states coupled with external manipulation and the ability to perform read-out (using lasers) provides the necessary tools for quantum simulations in an analog [10] or a digital [11] manner.

Historically, developments in cold atoms have followed an entirely different pathway. At first glance, the weak interactions of neutral atoms along with their difficult detectability renders them unsuitable for simulations of strongly interacting systems. Regardless, due to the low temperatures and large system sizes, cold atoms have great potential to serve as a test platform for the principles of quantum statistics. The first realization of the Bose-Einstein Condensate (BEC) was a significant milestone for this field [12, 13], which spurred an entire research field dedicated to using cold atoms as an experimental platform for the theory of weakly interacting quantum systems [14].

Following, a big step towards the simulation of strongly correlated systems was the introduction of optical lattices into the field of cold atoms. The reduction of dynamics inside the wells of an optical lattice resulted in the interaction energy of the atoms to be of the same order of magnitude as the kinetic energy of the system, realizing strongly correlated phases (e.g. as in the Mott-insulator [15]). With the new capabilities to use cold atoms in a regime analogous to the conditions of strongly correlated electrons in a solid, new possibilities arose; soon, it became possible to use fermionic isotopes in the same regime [16].

The detection tools of the time permitted measurements of macroscopic properties only (such as the density or momentum distributions). The continuous improvements in optically accessing the atom cloud over the next few years led the *Greiner* group and the *Bloch* group to realize fluorescence imaging of single atoms inside the optical lattice, which enabled single site imaging of atoms in the strongly correlated regime with the *Quantum Gas Microscopes* (QGM) [17, 18]. As a result, this enabled addressing and readout of strongly correlated 2D quantum systems of up to several hundreds

of atoms. The extension to fermionic systems and continuous developments of new readout and preparation techniques revealed interesting results, such as the realization of large anti-ferromagnetic correlations in fermionic systems [19], or the Harper-Hofstadter-Model in the interacting regime [20]. These QGMs are state-of-the-art in cold atom experiments due to their extremely high complexity, in which (1) a degenerate gas is prepared, then (2) loaded into a 3D lattice, from which (3) a single layer within the 3D lattice is selected, and finally (4) imaged with a high resolution objective, thus resolving the individual atoms with sub-micron resolution. There is a different approach selected by some other groups: the optical tweezer.

Loaded from a MOT and cooled further inside the small trap [21], the idea is to build small quantum systems using a bottom-up approach with the ability to entrap them in separate beams, which allows for imaging to become remarkably easier. This platform has already been successfully used in creating small Hubbard building blocks [22, 23], as well as small spin systems interacting via Rydberg excitations [24]. The main challenge with this approach, however, is scalability. The probability of loading one atom into a tweezer is nondeterministic, with typical probabilities reported to lie within the range of 50% [25] to 90% [26]. This results in probabilities of realizing defect-free systems (of sizes larger than a few atoms) to vanish. By rearranging the arrays after the initial imaging sequence, this limitation has been overcome by two groups [27, 28], which enables scaling these systems to larger sizes with no apparent limit. The aforementioned idea of creating building blocks of spin systems has already been extended to realize 51-atom spin chains as a result of this promising technique [29].

For QGMs, the choice of atom type is restricted to those with suitable properties that allow them to be cooled to degeneracy. The requirements in the case of optical tweezers, however, is different. While scattering lengths play a secondary role, tweezer experiments require suitable MOTs for loading of the tweezers as well as potential trap wavelengths with desired properties (e.g. tight confinement, commercially available high laser power, or state-insensitive traps (i.e. *Magic Wavelengths* [30]).

Here, Alkaline-Earth atoms (such as strontium) have the potential to serve as a valuable extension to the typically used Alkali atoms. In metrology, strontium has received much attention due to its *Clock transition*, making it an ideal candidate for optical lattice clocks [31–33]. While a clock transition is a powerful tool in the context of quantum simulations [34], strontium offers many more properties that promise improvements in the context of optical tweezers. A very cold MOT that cycles on a singlet-to-triplet line is good for loading tweezers, and a magic wavelength between these two states of this MOT at 515 nm gives a small tweezer confinement at a wavelength where commercially available, high power laser systems exist. These are ideal conditions to scale this technology to larger system sizes. Beyond this, due to their two-electron valence shells and level structure, strontium atoms have appealing Rydberg properties. The second electron could allow for trapping of strontium Rydberg atoms under certain conditions, and isotopes without hyperfine structure promise a simplified level structure that could improve coherence issues demonstrated by current Rydberg systems.

In the framework of this thesis, we set the cornerstone towards an apparatus that

provides a versatile platform to investigate the properties of strontium atoms in optical tweezers and the connected capabilities of interactions between strontium Rydberg atoms.

Outline

This thesis, presented in 5 chapters, outlines the progress in building this experimental apparatus.

Chapter 1 provides an introduction into the physical concepts involved in laser cooling and atomic trapping, to provide a suitable framework to understand all necessary considerations in the design of our apparatus. Building on those concepts, the properties of atomic strontium in the context of laser cooling will be discussed.

Chapter 2 discusses the developed laser systems to cool and trap strontium. This begins with the decisions made between various laser technologies to the final preparation of the laser beams for the experimental setup.

Chapter 3 introduces our vacuum setup with all design considerations and final performance.

Chapter 4 shows how we create optical tweezers with our high resolution objective and introduces how we use an AOD to produce 1D arrays of tweezers.

Chapter 5 presents our first results by showing the characterization of our MOT and presents the preliminary signal from atoms trapped in the tweezers.

2 Laser cooling & Trapping of strontium

Today, magneto-optical traps and dipole traps serve as standard techniques for trapping and cooling neutral atoms [35, 36]. However, the atomic species selected and its internal structure have a strong influence over the design of the experiment. From the existing techniques for preparing atomic vapor to the design of the vacuum setup to the resulting laser systems that finally cool and trap the atoms, many design considerations need to be taken into account.

The goal of this chapter is to introduce all relevant properties of atomic strontium as well as provide an overview regarding the main aspects of laser cooling and trapping. Following, this will be used to describe magneto-optical traps for strontium as well as to derive the so-called *magic wavelengths* that play an crucial role in the design considerations of our experiment.

2.1 Review: Cooling & trapping atoms with light

The concepts of laser cooling and trapping are discussed extensively in current textbooks [37, 38] and review articles [35]. This section summarizes the unique properties of laser cooling that will later motivate the experimental techniques used and design decisions made by the group.

2.1.1 Doppler cooling

The framework to understand Doppler cooling involves an atom traveling with velocity v in a light field created by counter-propagating laser beams with intensity I, wavevectors $\pm k$, and detuning Δ from the bare transition frequency of the atom ω_0. The velocity of the atom then shifts the laser detuning Δ with respect to the Doppler shift to an effective detuning of $\Delta_{eff} = \Delta \mp kv$ where $\pm k$ are the wavevectors of the light field. This gives a velocity-dependent radiation pressure force [38]:

$$\begin{aligned} F(v,\Delta) &= F_k(v) - F_{-k}(v) = \hbar k \Gamma_{sc}(\Delta - kv) - \hbar k \Gamma_{sc}(\Delta + kv) \\ &= \hbar k \Gamma_{sc} \frac{s_0}{2} \left(\frac{1}{1 + s_0 + 4\frac{(\Delta - kv)^2}{\Gamma^2}} + \frac{1}{1 + s_0 + 4\frac{(\Delta + kv)^2}{\Gamma^2}} \right) \end{aligned} \tag{2.1}$$

where $s_0 = \frac{I}{I_{sat}}$ is the saturation parameter that quantifies the intensity in terms of the saturation intensity $I_{sat} \propto \omega_0^3 \Gamma$, which is proportional to Γ, the linewidth of the atomic transition. This force is plotted in fig. 2.1.

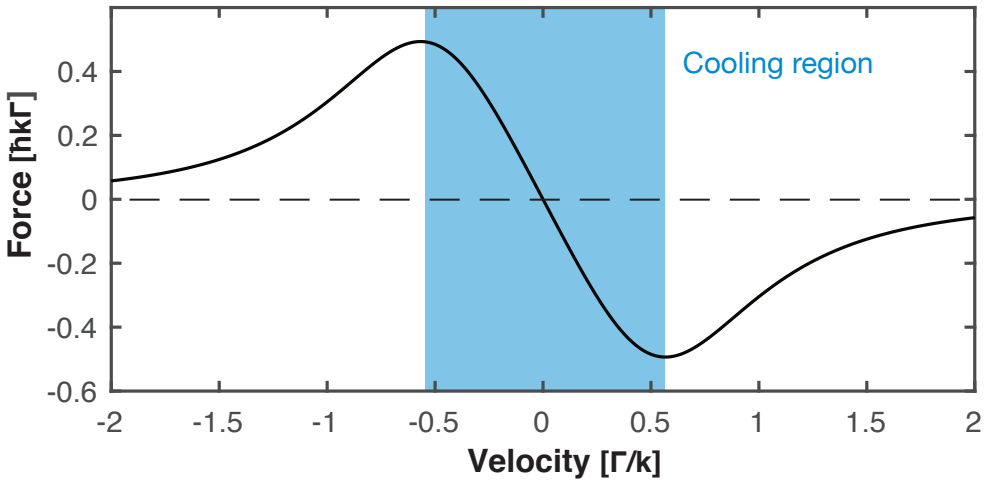

Figure 2.1: Dependence of light force on the velocity of the atom produced by two counter-propagating laser beams. The assumed saturation parameter s_0 is 0.5 and the detuning Δ is $\Gamma/2$. The blue region indicates a negative slope that indicates the cooling region where the light acts like a molasses.

By selecting a red detuning, the force near the zero velocity region indicates a linear damping force that leads to cooling. The final temperature of the gas is limited by the random walk that the atoms undergo under spontaneous re-emission of photons. The lower limit of the final temperature is given by the Doppler temperature [39]:

$$T_{\text{Doppler}} \approx \frac{\hbar\Gamma}{2k_{\text{B}}} \tag{2.2}$$

which can be reached only under the detuning $\Delta = \frac{\Gamma}{2}$. One remarkable result is that by considering fig. 2.1 and eq. 2.2, there exists a trade-off between the bandwidth of captured velocities and the lowest temperature that can be reached for a given linewidth rate. The trapping force and the range of velocities cooled (along with the lowest temperature that can be reached) grows linearly with the linewidth rate. One of the first realizations with the sodium is shown in ref. [40].

2.1.2 The Magneto-Optical Trap

To finally trap this atoms at this cold temperature, the magneto-optical trap (MOT) provides additional confinement within spatial degrees of freedom. Not only do atoms remain within a specific velocity range, but they also remain confined within a spatial volume. This is achieved by adding a magnetic field gradient in three dimensions to lift the degeneracy between magnetic sublevels to scatter spatial dependent photons from certain beams. The magnetic field gradient shifts the resonance frequency of atoms outside the center of the trap into resonance with the counter propagating beam (that has the correct polarization to drive the down-shifted transition), which results

in a force directing the atom towards the center of the trap. Similar to the scenario discussed in the previous section, a spatially-dependent force can be described using a magnetic-field-induced detuning $\Delta_{\text{mag. fields}} = \mu_B g_j m_j \frac{\delta B}{\delta x} x$. By linearizing the velocity and spatial dependency, the force is finally described by:

$$\boldsymbol{F}(v, \boldsymbol{x}) = \beta(\Gamma)\boldsymbol{v} - \beta(\Gamma)\kappa(g_j m_j)\frac{\delta B}{\delta \boldsymbol{x}}\boldsymbol{x} \tag{2.3}$$

where β is the linearized slope from the previously shown velocity-dependence of the force, κ is a magnetic structure-dependent pre-factor, and $\frac{\delta B}{\delta x}$ is the magnetic field gradient. This shows again that finally the linewidth rate Γ decides for a given magnetic field gradient the capture volume of the trap or in other words for higher magnetic field gradients that lead to higher trapping forces a higher linewidth rates allows for larger trap sizes.

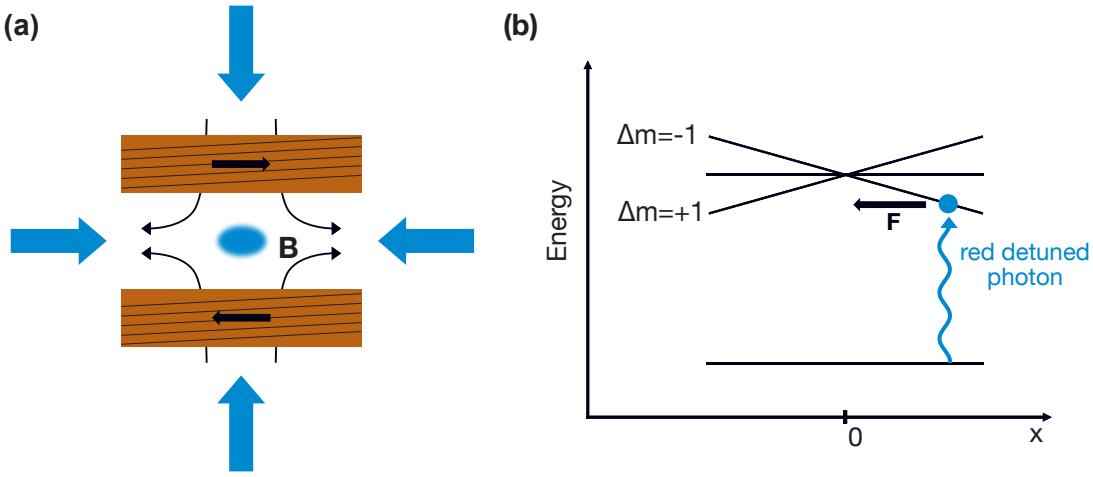

Figure 2.2: **(a)** Typical configuration of a MOT. The two coils are used in an anti-Helmholtz configuration to produce a quadrupole field that introduces the desired spatial detuning. **(b)** Graph that illustrates the spatial dependence of resonance that tunes atoms in the outer region of the MOT to resonance.

The principle is illustrated in fig. 2.2. The experimental realization of the MOT was a big step for the field [41] since it became possible to trap ensembles of millions of neutral atoms at temperatures of several hundreds of microkelvin and to investigate the physics in this regime.

2.1.3 Zeeman slower and 2D-MOT as atom sources

As previously discussed, the capture velocity and capture volume of MOTs is limited by the maximum light pressure of the chosen transition. A typical capture velocity for an alkali atom with a typical D-line linewidth of $\Gamma = 2\pi \times 6$ MHz is on the order of

$1 - 10$ m/s, which is two orders of magnitude smaller than the peak of the thermal distribution of a room temperature gas.

To realize MOTs with much higher numbers of atoms, techniques were developed to overcome this barrier by pre-cooling and pre-collimating the thermal atoms:

- The *Zeeman slower* uses a one-dimensional magnetic field gradient to overcome the limited capture range of red detuned laser beam by slowing atoms down while keeping them consistently resonant with the suitable magnetic shift. This was demonstrated for the first time with sodium [42].

- The *2D-MOT* adds to the quadrupole field produced by two coils using another pair of coils to eliminate the gradient in one direction - In this dimension the 2D MOT no longer provides spatial confinement. Instead of a trap, a continuously leaking, collimated atom beam arises. The beam is remarkably colder in the other two directions and spatially confined. This is ideal to overcome the confinement of a differential pumping stage, making it an ideal solution to reach low pressures in the 3D MOT region. For this purpose, the 2D MOT was realized the first time in ref. [43].

2.1.4 Dipole trap

Another way to trap atoms is through the use of a *dipole trap*. Far-detuned light interacts with atoms and traps them in an conservative potential formed by the beam profile of the laser beam. This can be understood by applying a semi-classical oscillator model, or as the result of intensity-dependent light shifts (i.e. quantum effects). Both pictures are described in detail in ref. [44]. The multi-level case is described in [37].

For a two-level system with a bare resonance frequency ω_0, linewidth Γ and a detuning Δ (which is much larger than Γ), the trap potential and the corresponding scattering rate Γ_{sc} is:

$$\begin{aligned} U(\boldsymbol{x}) &= \frac{3\pi c^2}{2\omega_0^3}\frac{\Gamma}{\Delta} I(\boldsymbol{x}) \\ \Gamma_{sc}(x) &= \frac{3\pi c^2}{2\hbar\omega_0^3}\left(\frac{\Gamma}{\Delta}\right)^2 I(\boldsymbol{x}) \end{aligned} \tag{2.4}$$

As a result, the intensity profile of the laser beam defines the trap potential for the atoms. The ideal dipole trap lies in a regime where the scattering rate Γ_{sc} is much smaller than the depth of the trap, which produces a nearly conservative. This can be achieved by selecting a sufficiently large detuning, since the scattering rate decreases faster than the potential depth for large detuning.

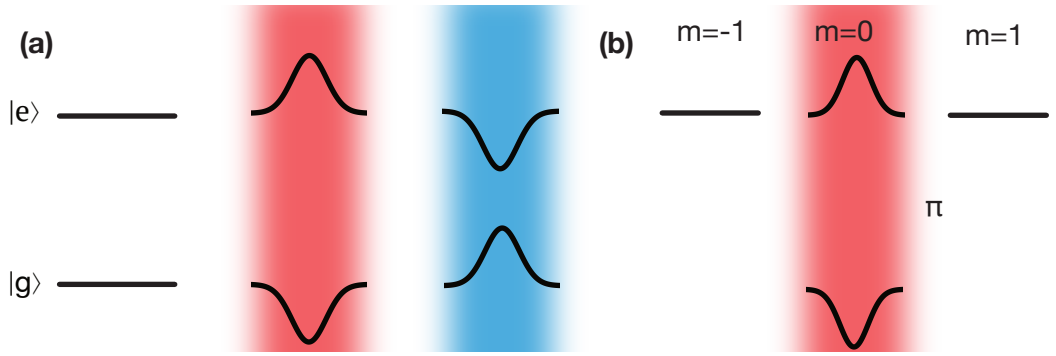

Figure 2.3: Illustration of the typical application of a dipole trap. **(a)** A red or blue detuned laser beam shifts the levels of a two-level system to either attract or repel the atom. **(b)**The polarization of the irradiated light field ultimately determines the states to which experience a light shift.

In general, more than one transition must be taken into account. By treating the effect of a far-detuned laser field as a second order perturbation in the electric field, where the proportionality of the potential to the intensity of the field remains conserved, the expression remains an analogous form:

$$\begin{aligned} U(\boldsymbol{x},\omega) &= -\frac{1}{2\epsilon_0 c}\alpha_i(\omega)I(\boldsymbol{x}) \\ \alpha_i(\omega) &= \sum_k \frac{2\omega_{ik} \mid \langle i \mid\mid \mathbf{d} \mid\mid k\rangle \mid^2}{3\hbar(\omega_{ik}^2 - \omega^2)} \end{aligned} \tag{2.5}$$

Here, i is the state of interest, α is the polarizability, and we sum over k, all the dipole matrix elements, weighted with respect to their detuning. This is a very general treatment that does not demonstrate the complexity of the problem (for example, distinguishing between magnetic sublevels results in polarization-dependent polarizability). This will be treated in more detail for the specific case of strontium in the next section.

For the quantum interpretation of the dipole trap, the detuned light field induces mixing between the states, which, in the red detuned case, pushes the levels apart (i.e. dressing). The dressed states are now separated by a larger energy difference, which can be relevant for exciting atoms while they remain trapped. In this picture the dressing field introduces a *light shift* that forms a conservative potential that the atoms see.

2.2 Strontium

This section will introduce atomic strontium and its relevant properties in the context of our experiment. With a brief history in the research field of cold gases, strontium is described in further detail in ref. [45].

2.2.1 Isotopes

strontium has four naturally occurring isotopes, three of which demonstrate bosonic statistics (^{84}Sr,^{86}Sr and ^{88}Sr) and the remaining shows fermionic statistics (^{87}Sr). They are listed together with their main properties in table 2.1

Mass [u]	**Statistic**	**Nuclear Spin**	**Scattering length [a_0]**	**Abundance [%]**
84	boson	0	123	0.56
86	boson	0	830	9.81
87	fermion	9/2	97	7.00
88	boson	0	-1	82.58

Table 2.1: Properties of the different stable Isotopes of strontium.

While the bosonic isotopes with a nuclear spin of $I = 0$ show an especially simple atomic structure which simplifies many experimental considerations, the fermionic isotope with a large nuclear spin of $I = 9/2$ provides an exceptionally difficult case for laser cooling (see next section). However, due to its fermionic characteristics, strontium 87 enables interesting physical models which can be implemented [46].

Another remarkable difference between the isotopes lies in their scattering lengths a_0, which determine the performance of evaporative cooling techniques. Here, the isotope with the highest abundance (^{88}Sr) is especially unsuitable.

2.2.2 Level structure

The level structure of strontium (fig. 2.4) shows the typical singlet-triplet manifolds due to its $S = 1$ electronic structure. This is a distinguishing feature that significantly enhances the strontium toolbox.

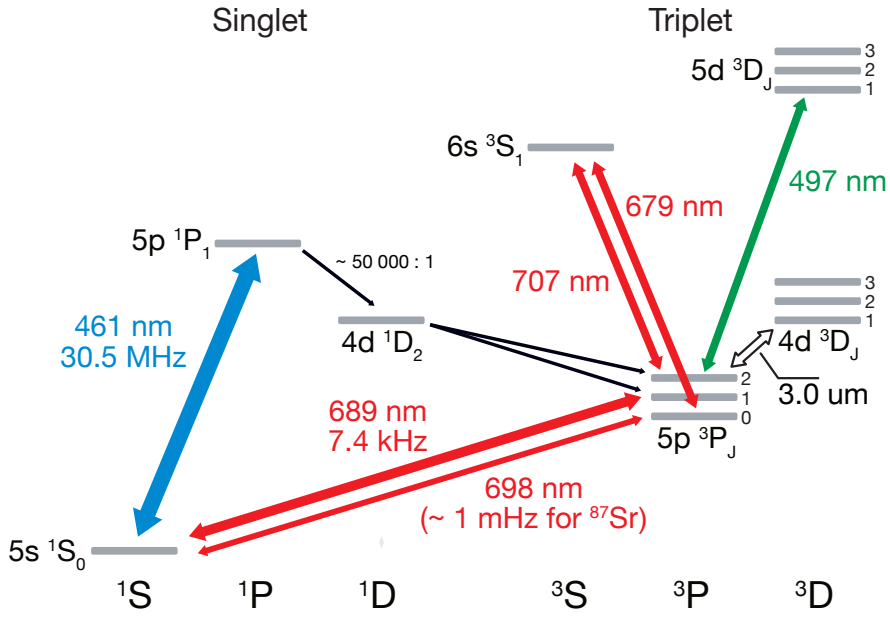

Figure 2.4: Level diagram of atomic strontium including all relevant optical transitions for laser cooling and trapping.

Here, a remarkable feature is shown in the intercombination lines ${}^1S_0 \rightarrow {}^3P_1$ and ${}^1S_0 \rightarrow {}^3P_0$ (^{87}Sr) which are forbidden in the strict picture of the quantum numbers S and J. However, due to fine and hyperfine structure mixing (^{87}Sr), ultra-narrow optical transitions are permitted (which is not available in alkali atoms).

In addition, the broad ${}^1S_0 \rightarrow {}^1P_1$ transition at 461 nm within the singlet manifold is approximately five times stronger than a typical alkali transition, which enhances the radiation pressure and simplifies the initial steps required for cooling.

Furthermore, strontium exhibits multiple higher-lying states in the triplet manifold within the visible range of light. In particular, this makes it possible to create interesting trap scenarios for dipole traps in which, for example, different states experience the exact same potential well (i.e. trap). These wavelengths are known as the *magic wavelengths*, and will be discussed in greater detail in section 3.3.

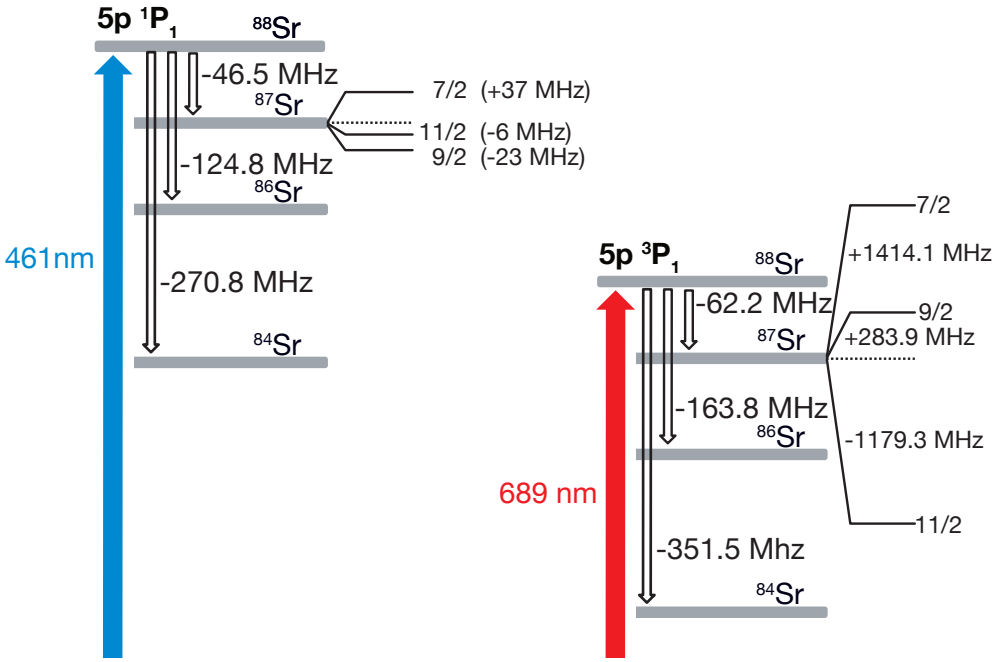

Figure 2.5: Energy shifts caused by isotope shifts and hyperfine splitting summarized for the two 'MOT' transitions. For the fermionic isotope ^{87}Sr, the dashed line indicates the quasi energy levels given by the isotope shifts only (separated from the hyperfine splitting, given by the solid).

The isotope shifts of the two main (i.e. MOT) transitions ${}^1S_0 \rightarrow {}^1P_1$ and ${}^1S_0 \rightarrow {}^3P_1$ are shown in fig. 2.5. The isotope shifts on the blue transition are small relative to typical isotope shifts of alkali atoms (several *GHz*), which enables an experiment capable of addressing all isotopes with a single laser system ([45]). In addition, the isotope shifts on the red transition are comparable to those of the singlet transition, whereas the hyperfine splitting is much larger, spanning 2.6 GHz.

2.3 Magneto-Optical Traps with Strontium

The coexistence of the broad ${}^1S_0 \rightarrow {}^1P_1$ transition and the narrow ${}^1S_0 \rightarrow {}^3P_1$ transition allows for a capture range over an extraordinarily broad transition. This enables the use of trapped atoms in a large MOT (with a large Doppler temperature) to load another MOT on the narrow intercombination line, in which extremely low temperatures (i.e. hundreds of nanokelvin) are possible. This has been achieved [47], and has been shown as a promising way to bring strontium close to degeneracy [48].

2.3.1 Blue MOT

The broad transition ${}^1S_0 \rightarrow {}^1P_1$ is not perfectly cyclic due to the presence of a small decay channel from the ${}^1P_1$ state into the ${}^1D_2$ state with a ratio of approximately $1 : 50,000$. From here, the atom further decays into the metastable triplet states within the ${}^3P_J$ manifold. From these states, the atoms can be re-pumped; historically, different states were attempted [45, 49]. However, all these states are extremely difficult to observe in absorption spectroscopy since it is nearly impossible to excite atoms thermally to the ${}^1D_2$ state. We decided to follow the scheme of the *Ye* group ([49]) and use the transitions from the ${}^3P_J$ manifold to the $6s\,{}^3S_1$ states, which allows atoms to be pumped back to ${}^3P_1$ and then decay back to the ground state ${}^1S_0$. The wavelengths of the two required transitions are 679 nm and 707 nm.

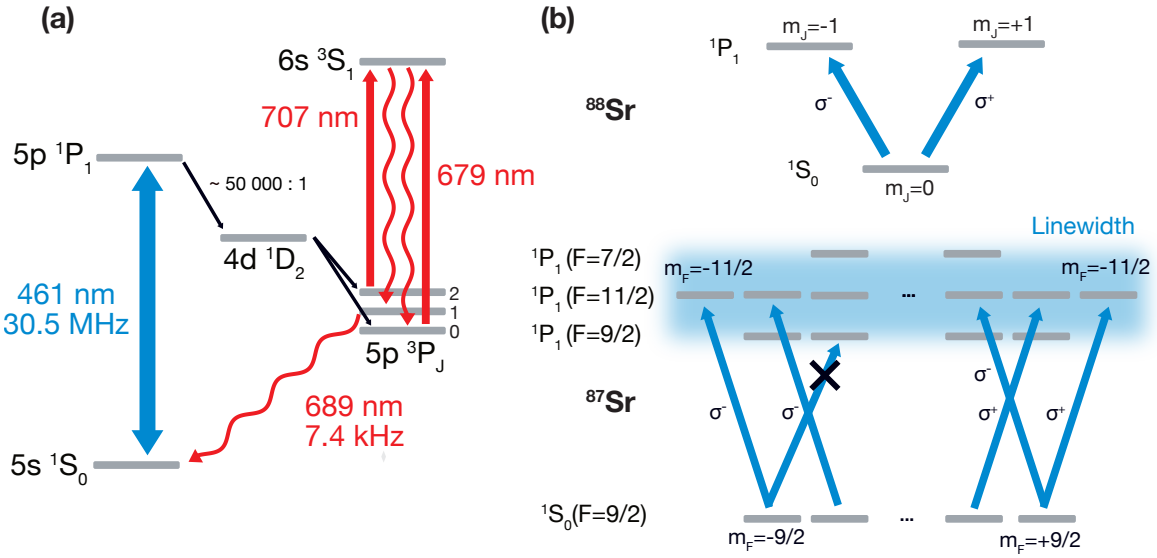

Figure 2.6: **(a)** Level diagram of the relevant states for the blue MOT with all involved re-pumping states.**(b)** This diagram shows the magnetic configuration for the bosonic and fermionic cases of the blue MOT. While the bosonic case is the ideal $L = 0 \rightarrow L = 1$ configuration, the fermionic case is more complex due to the existence of multiple hyperfine states which are not resolved.

Besides the small leakage, the ${}^1S_0 \rightarrow {}^1P_1$ transition is a typical (see fig. 2.6) situation where the m_J states build the desired V-configuration in which the ground state has no magnetic sublevels.

Fermions

Due to the hyperfine splitting of the fermionic isotope, the situation changes (shown in fig. 2.6). The excited state splits into three states with $F = 7/2$, $F = 9/2$ and

$F = 11/2$, and the only state fulfilling the $F' = F + 1$ condition to achieve a quasi V-shape configuration is the $F = 11/2$ state. The small hyperfine splitting and broad linewidth does not permit the isolation of this state, rendering the performance of the fermionic MOT to be worse than that of the bosonic MOT [45].

2.3.2 Red MOT

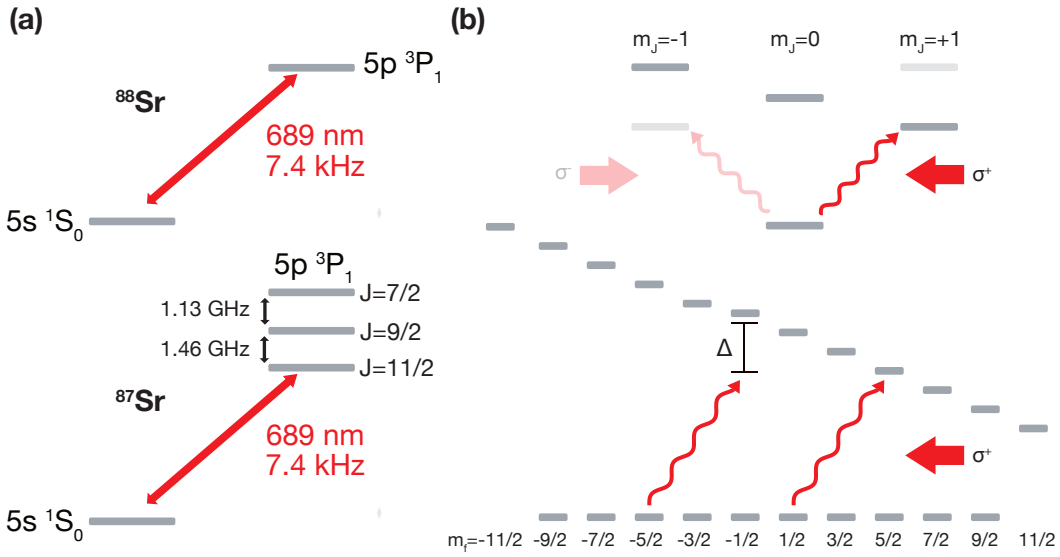

Figure 2.7: (a) This figure shows the ${}^1S_0 \rightarrow {}^3P_1$ transition for the bosonic and fermionic cases of the red MOT. On the red transition of the fermionic isotope, the hyperfine splitting is well resolved. **(b)** The magnetic structure for the bosonic isotopes is the ideal V-shaped structure. The fermionic case, however, has a unsuitable magnetic structure. The ground state has no magnetic splitting, while each magnetic sublevel has a different g-factor g_F. As a result, atoms in different magnetic states experience different effective detuning and the MOT does not function as desired.

The Red MOT can be used as a second cooling stage which cools the already cooled atom cloud of the blue MOT further. Since the linewidth difference between the two transitions is approximately four orders of magnitude, there is a significant mismatch in the ideal magnetic field gradients and the achieved bandwidths in velocity space of the two MOTs. To prevent this, the red transition can be artificially broadened and finally tapered down to the desired narrow linewidth. This was demonstrated for the first time in ref. [47]. The final match in magnetic field gradient can be reached either through a sudden quench in the magnetic field gradient [49], or by selecting a smaller gradient that functions for both MOTs [50], resulting in a trade-off between blue and red MOT performance.

The unique feature of the red MOT is the ability to reach extremely low tempera-

tures. Since the the Doppler temperature is 179 nK which is less than half of the recoil temperature (460 nK), the semi-classical picture in which only the internal states are treated quantum-mechanically are no longer appropriate. This is studied extensively in, for example, ref. [51].

Fermions

For the fermionic isotope, the red MOT is quite more complex. As shown in fig. 2.7, the magnetic structure of the ${}^1S_0 \rightarrow {}^3P_1$ transition does not match the usual MOT scheme in which the differential gyromagnetic ratio $\Delta g = g'_F - g_F$ for $\Delta m_F = \pm 1$ transitions is the same for all hyperfine levels. As a result, it is impossible to run the MOT with only one laser frequency. This can be solved (in part) by introducing a second beam that uses the ${}^1S_0(F = 9/2) \rightarrow {}^3P_1(F = 7/2)$ transition to keep the MOT cycling over a certain magnetic sublet range, achieving a time averaged cooling. This was demonstrated for the first time in ref. [52].

Summary of Temperatures

	Wavelength [nm]	**Doppler Temperature [μK]**	**Recoil Temperature [nK]**	**Sub-Doppler Temperature [μK]**
Sr	461	731	1029	–
Sr	689	0.179	460	–
Rb	780	146	361	50 (typical)

Table 2.2: Summary of the characteristic MOT temperatures of both strontium MOT transitions as well as the values for rubidium. The atomic structure of strontium does not allow for sub-Doppler cooling techniques, which are commonly used for alkali atoms. Despite the sub-Doppler cooling of Rubidium, the temperatures achievable by the red MOT are remarkably lower.

2.4 Magic wavelengths of Strontium

The variety of optical transitions in the triplet manifold produces a unique situation in which dipole traps with certain wavelengths cause the same light shifts for both the ${}^3P_J$ states as well as the ground state ${}^1S_0$. These are known as the *magic wavelengths*. They have been relevant in optical lattice clocks [53], in which identical light shifts for ${}^1S_0$ and the 'clock state' ${}^3P_0$ prohibits relative light shifts that alter the transition frequency due to changing lattice intensities.

Our proposed sideband cooling strategy within the tweezers (see section 6.2) requires similar conditions. In our case, a magic wavelength between ${}^1S_0$ and ${}^3P_1$ that is attractive ($\alpha > 0$) is required. The level structure, with the transition from ${}^1S_0$ to ${}^1P_1$ (at 461 nm) and the transitions from the triplet manifold ${}^3P_J$ to the ${}^3D_J$ manifold (around 495 nm), suggests that there is a magic crossing with positive polarizability in

the green sector of the visible spectrum, which has not been reported thus far in the literature. For this, we performed our own calculations of polarizabilities of all states provided by documented spectroscopy data. Relevant references are [54–60].

2.4.1 Polarizability of a multi-state atom

Beginning from section 3.3, formula 2.5 must be investigated in greater detail. A good introduction is given in ref. [49], where this equation is analyzed for the clock state. Rewriting eq. 2.5 and replacing the dipole matrix element with A_{ik} gives:

$$\alpha_i(\omega) = 6\pi\epsilon_0 c^3 \sum_k \frac{A_{ik}}{\omega_{ik}^2(\omega_{ik}^2 - \omega^2)} \tag{2.6}$$

where i and k can be either magnetic sublevels or whole fine structure manifolds, and the implied dipole operator specifies a selected light polarization. Different light polarizations couple different magnetic sublevels to one another, which leads to different polarizabilities. These are not distinguished in literature; for higher lying states, this is not done for fine structure manifolds. The decay time into underlying manifolds is quoted with the lifetime τ_L. These can be related with the Clebsch-Gordan coefficients and can be computed via:

$$\frac{\tilde{A_{ik}}}{\tau_L} = \frac{(2J_i+1)\begin{Bmatrix} J_i & J_k & 1 \\ L_K & L_i & S \end{Bmatrix}^2}{\sum_{J=|L_i-S|}^{|L_i+S|}(2J+1)\begin{Bmatrix} J & J_k & 1 \\ L_K & L_i & S \end{Bmatrix}^2} \sum_{m_k=-J_k}^{J_k} (2J_k+1)\begin{pmatrix} J_i & 1 & J_k \\ m_i & p & -m_k \end{pmatrix}^2 \tag{2.7}$$

where J's are the total angular momenta, L's the electron angular momenta levels which define the manifolds, m's are the magnetic sublevels, and p defines the light polarization as a spinor. The curly braces are 6j-symbols and the parentheses are 3j-symbols. The calculated $\tilde{A_{ik}}$ requires a correction factor $\zeta(\omega_{ik})$ since eq. 2.7 cannot take into account the change of the dipole matrix element, due to the fine structure splitting ($A_{ik} \propto \hbar\omega_{ik}$). The correction factors can be found in ref. [49].

With this formula, a suitable magic crossing for the ${}^1S_0 \rightarrow {}^1P_1$ transition was found. These results were cross-checked by reproducing the magic crossing of the ${}^1S_0 \rightarrow {}^3P_0$ transition. The results can be found in fig. 2.8, in which a magic crossing at $\lambda_\mathrm{m} = (515 \pm 3)$ nm was identified. The consequences will be discussed in chapter 6.

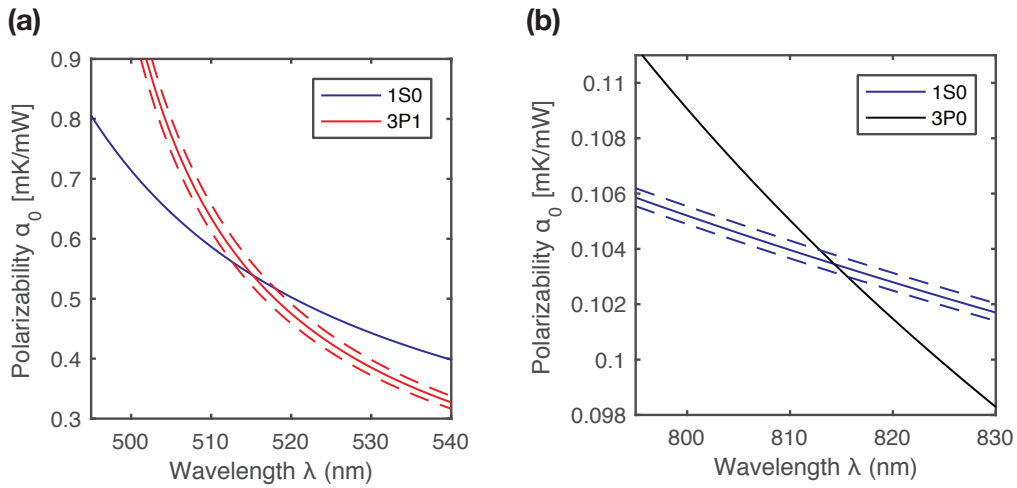

Figure 2.8: (a) Magic wavelength crossing at 515 nm for the $^1S_0$ and $^3P_1$ state with the error bars due to discrepancies found in literature. The polarizability α_0 is given in [mK/mW], assuming a dipole trap waist of 500 nm. The $^3P_1$ state magnetic quantum number is 0 and the assumed light is linearly polarized. **(b)** Magic wavelength crossing at $\approx$ 813 nm for the $^1S_0$ and $^3P_0$ state. The assumed light is linearly polarized, and the assumed dipole trap waist is 800 nm. The $^3P_0$ has no error bars (on the scale of the plot), assuming the precise values quoted by the atom clock community [53].

2.4.2 Polarization dependence of polarizability

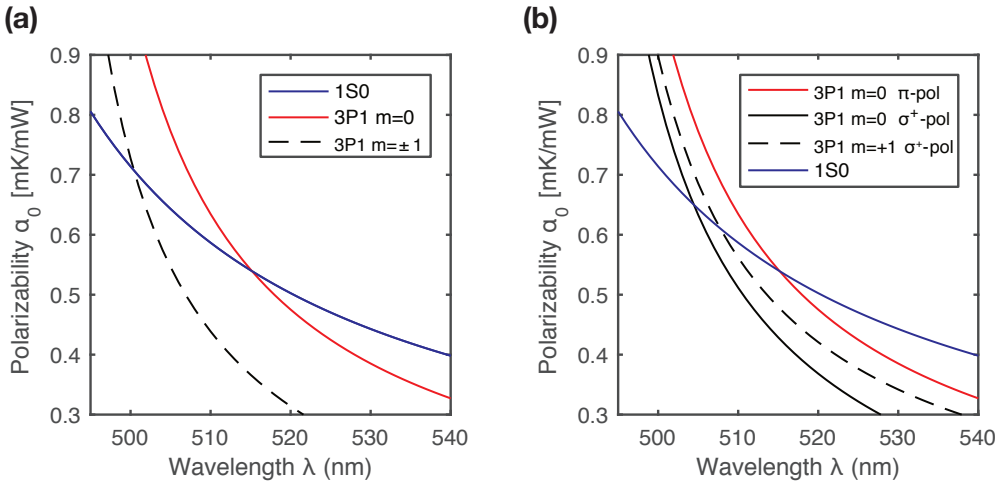

Figure 2.9: (a) The polarizability of $^3P_1$ shows a magnetic sublevel-dependence. The dashed line shows that for the $m = +1$ state, the polarizability changes (in comparison to $m = 0$), resulting in a change in the magic wavelength crossing for this state. **(b)** Corresponding to the sublevel dependence, the polarizability also depends on the light polarization, which is shown by the solid and dashed black lines.

After calculating the magic wavelength, we further explored the consequences of this calculation. This was particularly apparent in the dependence of the polarizability on the polarization and magnetic levels of the $^3P_1$ state, which is demonstrated in fig. 2.9. A change in polarization can easily affect the magic wavelength crossing on the order of several nanometers. This is especially critical, since other groups that used high-NA objectives to make optical tweezers came to the realization that the high-NA introduces spatially-dependent polarizations [61] which would cause, in our case, non-magic conditions at certain points located within the trap.

3 Laser systems

This chapter introduces our various laser systems and discusses our strategy as to how we stabilize these systems to achieve the desired wavelengths. Since one of the major advantages of strontium is the wide range of optical transitions, our laser systems have become quite extensive. This will be discussed in greater detail within our outlook regarding future steps, in which we look to upgrade our laser systems to incorporate flexibility.

3.1 Blue System

Due to the broad ${}^1S_0 \rightarrow {}^1P_1$ transition and its strong scattering force, the blue laser system is used to pre-cool the hot atoms (i.e. through the Zeeman slower and 2D MOT), to trap the atoms in the 3D MOT, and finally to image the atoms inside the optical tweezers. The broad linewidth is accompanied by a high saturation power of $I_{sat} = 42\frac{\mathrm{mW}}{\mathrm{cm}^2}$, resulting in an overall power consumption of several hundreds of milliwatts of 461 nm light.

There are two different pathways that can achieve this requirement:

- For the past few years, it has been possible to purchase laser diodes in the blue range commercially [1], capable of delivering output powers of up to 100 mW. However, this would require more than one laser since the output power of a single diode is too low. This can be solved by using, for example, offset locks ([62]). Such a setup is realized in ref. [63]. Recently, it has been shown that for applications with low coherence requirements (e.g. the Zeeman slower), high power multi-mode diodes could be used [64].
- Second harmonic generation (SHG) in crystals enhanced by cavities has become a standard technique, in which conversion efficiencies of over 50% are possible over the whole near infrared range. The halved frequency of the transition (at 922 nm) lies in the near-infrared regime, in which it is easier to build laser systems of high power. Either laser diodes amplified by tapered amplifiers or Titanium:Sapphire lasers can be used to deliver powers of up to few watts.

3.1.1 Second harmonic generation laser system

We selected a commercial SHG system from *Toptica AG*[2]. This system is an assembly of an External Cavity Diode laser (ECDL) at 922 nm, a Tapered Amplifier (TA), optics

[1] For example, from *Nichia*, Model NDB4216E-E
[2] Exact model: *Toptica DL SHG pro*

to fix the beam shape, as well as a bow-tie cavity with a BBO crystal for the frequency doubling. Following, another optical assembly is used to create the ideal beam shape for fiber coupling. The laser wavelengths and powers at each step are:

	Wavelength [nm]	Laser power [mW]
ECDL	922	22
TA	922	$1,700 - 1,800$
SHG	461	$880 - 900$
Fiber-coupled	461	$650 - 700$

Table 3.1: Laser power of the blue laser system starting from the diode laser to the final laser power of 461 nm light in the optical fiber.

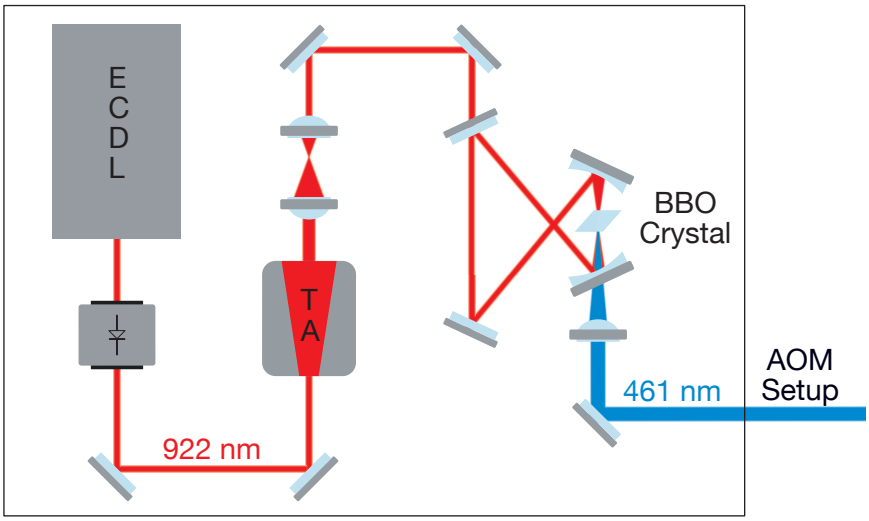

Figure 3.1: Schematic of the components of our *Toptica* SHG pro laser system. An external cavity diode laser seeds a tapered amplifier to achieve doubling in a bow-tie cavity using a BBO crystal. The cavity length is stabilized with a piezo in one of the mirrors and transmission feedback through an internal photodiode.

The linewidth of the bow-tie cavity is larger than the laser linewidth, which ensures tunability of the laser while the cavity is only locked to maximize the power of the 461 nm light. It is then possible to have feedback to the ECDL laser, locking to an atomic transition.

3.1.2 AOM setup

The generated laser light is distributed to its different applications using Acousto-Optical Modulators (AOMs), which split the laser into multiple beams at the desired

detuning from the bare ${}^1S_0 \rightarrow {}^1P_1$ resonance. The main considerations for the design of the AOM setup have been:

- Due to the relatively large linewidth of this transition, the capture range is also large for a given laser power. Here, we want a red-detuning of 600 MHz to the bare transition, which is challenging to achieve with AOMs (which will be discussed in greater detail).
- The small isotope shifts allow us to cover all stable isotopes with AOM detunings. This is demonstrated in ref. [45].
- In certain regimes, optical tweezers introduce large detunings between ${}^1P_1$ and ${}^1S_0$. To drive the transition for the fluorescence imaging, ideally, the light shifts have to be captured.

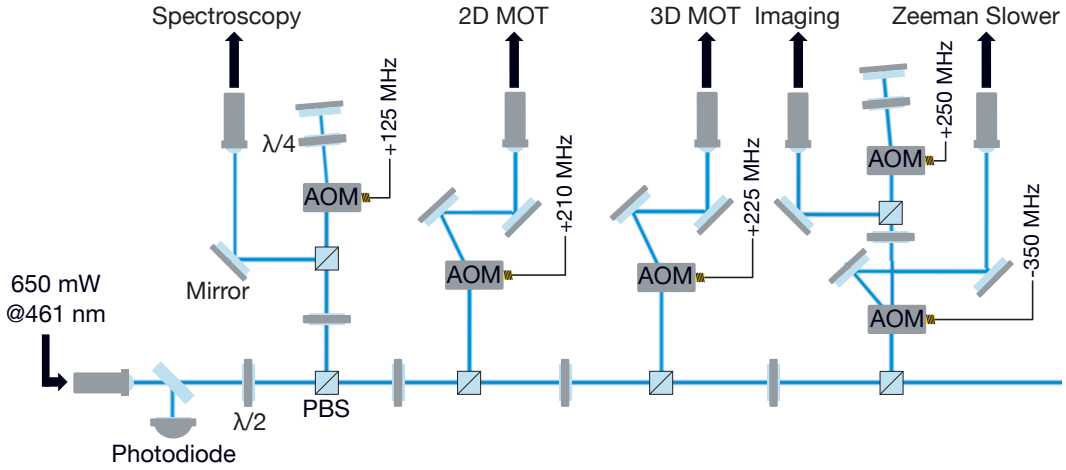

Figure 3.2: AOM setup to divide power into several beams and to adjust the frequency to the desired detuning. The schematic shows all optics used (except additional optics implemented to stabilize and monitor the power, as well as additional mirrors for beam routing).

Inspired by [45], we decided to bridge the 600 MHz step to the Zeeman slower by lifting the path to the spectroscopy with an double pass AOM [3] to offset the detuning of the the bare laser by 250 MHz relative to the spectroscopy. With this AOM, we can also switch between ^{88}Sr and ^{87}Sr (68 MHz apart), which is possible with the bandwidth of a usual double pass AOM. The system of the *Schreck* group is able to reach all isotopes, which requires a bandwidth of 270 MHz (see fig. 2.5). [4].

[3] All our used AOMs are from the *IntraAction* ATM-Series

[4] This is achieved by AOMs which can handle very small beams for enhanced bandwidth. For example, the *Gooch & Housego* Model. 3350-199

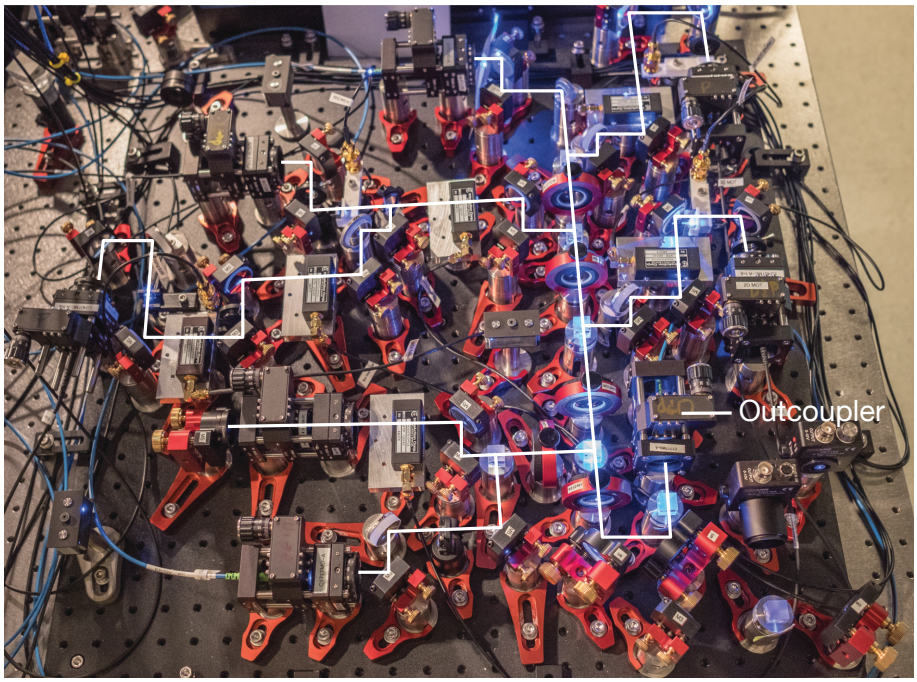

Figure 3.3: Photo of our AOM setup to distribute the blue laser beam. White lines are shown to improve the visibility of the beam paths.

3.1.3 Spectroscopy cell

In order to stabilize the blue laser system to the wavelength of the transition, we decided to build a heated spectroscopy cell, which is also known as a 'heatpipe' ([65]). This is required since the melting point of strontium is 777 °C, rendering the vapor pressure of strontium very low at room temperature. Using the Clausius-Clapeyron equation and the ideal gas law, the atomic density n is estimated by:

$$n(T) = \frac{P(T)}{k_B T} = \frac{10^{-9450/T+10.62-1.31log(T)}}{k_B T} \tag{3.1}$$

where P is the pressure in millibar and T is the temperature in Kelvin. By comparing room temperature with a heating temperature of 350 °C which can be easily achieved, the improvement of vapor density (and thus the gain in absorption) is:

$$\frac{n(T = 350\,^\circ\mathrm{C})}{n(T = 20\,^\circ\mathrm{C})} = 1.1 \times 10^{15} \tag{3.2}$$

while the the velocity distribution density around $|\mathbf{v}| = 0$ (the important measure in Doppler-free spectroscopy) decreases only on the order of 10.

With this improvement in density, it is even possible to see the intercombination line ${}^1S_0 \rightarrow {}^3P_1$ as it is demonstrated in [45].

Another unique feature of strontium is that it coats glass surfaces fairly quickly. This introduces challenges during the design process of the spectroscopy cell, since the glass windows of the cell have either a comparable temperature to the heated part of the cell to prevent coating, or must be placed in a way such that the density of strontium is much smaller compared to the heated section. The second approach can be achieved by increasing the distance between the windows and the heated section, and by adding a buffer gas to the cell to prevent the transport of atoms from the heated section to the windows.

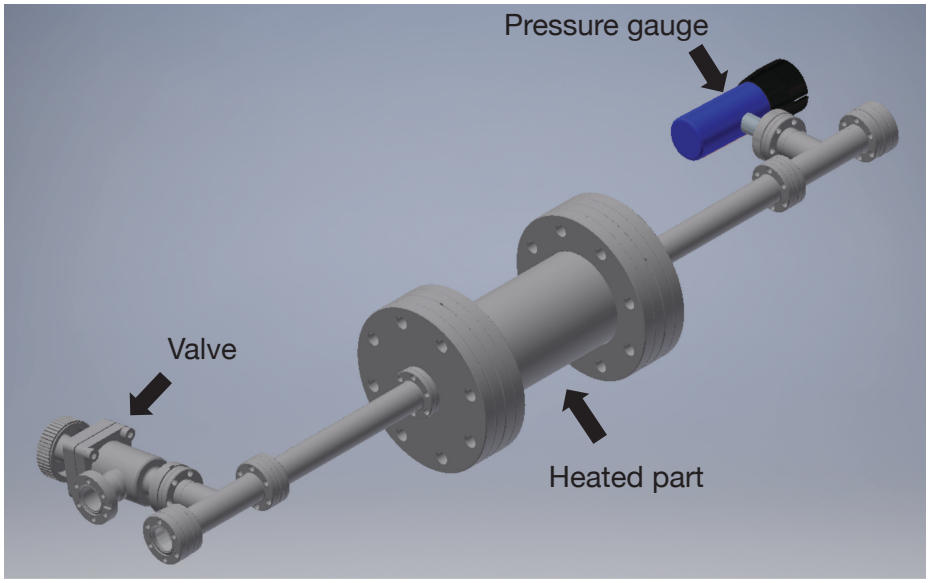

Figure 3.4: CAD drawing of the strontium heat pipe. The valve is used to pump down the pipe and to finally inject the Argon buffer gas, while the pressure gauge monitors the pressure inside the cell. The bucket in the middle has a length of 120 mm and encases the strontium atoms. In addition, it is covered in insulation and is heated by a band heater The viewports have a diameter of 16.4 mm.

Inspired by the design in [45], we took the second approach by designing a spectroscopy system with a heated bucket (in which the strontium atoms are located) and two glass windows which are further out. A drawing is show in fig. 3.5.

The bucket in the middle is heated by a band heater and the cell is mounted on copper mounts next to the bucket and work as a heat sink to keep the tubes that connect the bucket with the windows cold. We filled the cell after a bake out with Argon and and run it at an Argon pressure of $\approx$ 10 mTorr and heat it according to the temperature sensor mounted on the bucket to 450 °K. We expect the temperature of the strontium to be significantly lower on the order of 350 °K. A typical spectroscopy signal can be seen in fig. 3.6

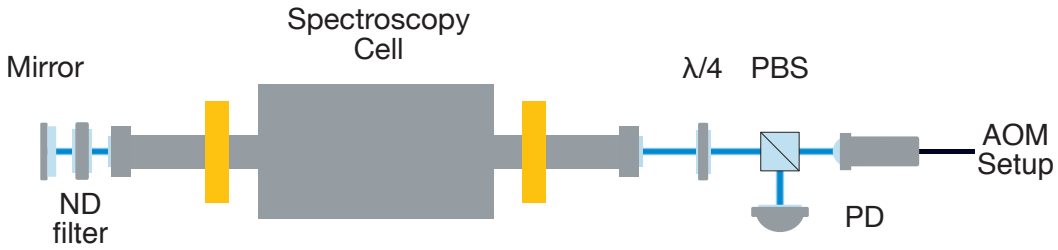

Figure 3.5: Setup for Doppler-free spectroscopy. Here, the probe beam is the attenuated retro-reflected pump beam. In this configuration, the probe and pump beams have orthogonal polarizations. For the given magnetic sublevel configuration of strontium, this should not affect the contrast of the signal.

In order to lock the laser to the ${}^1S_0 \rightarrow {}^1P_1$ transition, we decided to use Doppler-free spectroscopy. The optical setup used to achieve this is shown in 3.5. To provide feedback to the laser, we use a Pound-Drever-Hall lock (PDH) [66]. To phase-modulate the signal, we directly modulate the current for the 922 nm diode laser with a frequency of 20 MHz. The measured error signal [5] is then used as feedback to the diode laser via a digital PID controller realized by the laser controller [6].

A typical spectroscopy signal and corresponding error signal can be found in fig. 3.6. The dominant abundance of ^{88}Sr ensures that this absorption line is clearly visible. Due to the high bandwidth required for the photodiode and the low sensitivity of typical Silicon photodetectors for 461 nm light, the best signal was achieved with a slightly power broadened configuration, at which the slope of the error signal is of the highest quality.

[5] To produce the modulation and finally mix the signal, we used the *Toptica* PDH-box
[6] *Toptica* DLpro laser controller

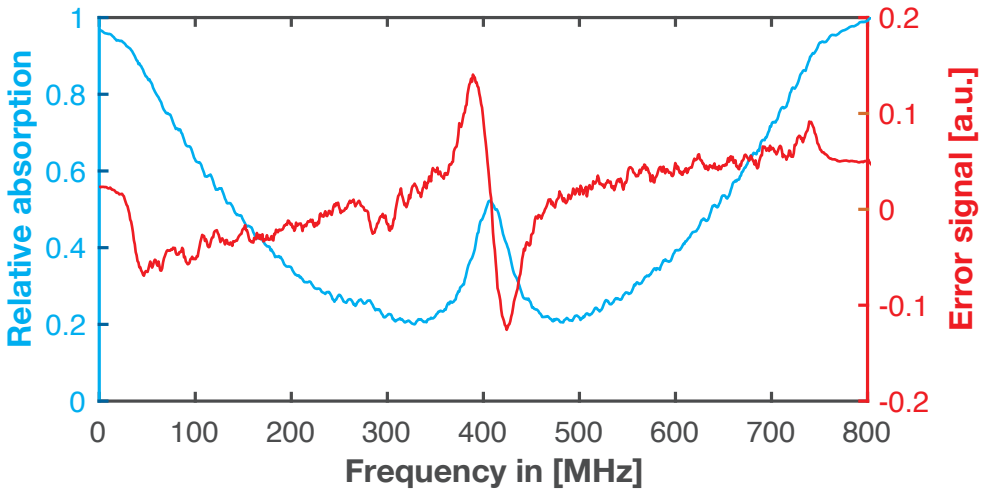

Figure 3.6: Typical Doppler-free spectroscopy of our setup. The blue line shows the Doppler-broadened absorption line of the $^1S_0 \rightarrow {}^1P_1$ transition, and the dip in the middle shows the frequency to which we are stabilizing. The red line shows the generated error signal that is used for feedback. The setup is optimized for the best qualitative slope in the error signal. The plot is achieved by sweeping the grating of the diode laser, and the frequency calibration is performed using a wavemeter.

3.1.4 Future improvements

As mentioned above, there is a need for high laser powers, a large span of frequencies to cover all possible detunings within one isotope, as well as the ability to switch between isotopes. Several improvements are envisioned for the future to upgrade from our current system and achieve several of these goals. The general idea is shown in fig. 3.7.

Our current setup splits the beam into different paths in order to change the frequency. Alternatively, any of these could be picked up for an offset lock of an additional ECDL laser. In particular, an offset lock in the spectroscopy junction of our current setup could be used to achieve the detunings required by each isotope, without losing power in the process.

A similar setup would work for our imaging system, in which initial investigations have shown that in certain circumstances, extremely large light shifts must be overcome.

3.1.5 Repumpers

Over the past two decades, several repumping schemes have been developed. There is the 497 nm $^3P_2 \rightarrow {}^3D_2$ repump transition used by the *Schreck* group [45]. A newer scheme developed by the *Killian* group [67] and recently used by the *Weidemüller* group [68] is the use of the $^3P_2 \rightarrow 5p^2\ {}^3P_2$ transition at 481 nm. Here, the linewidths are

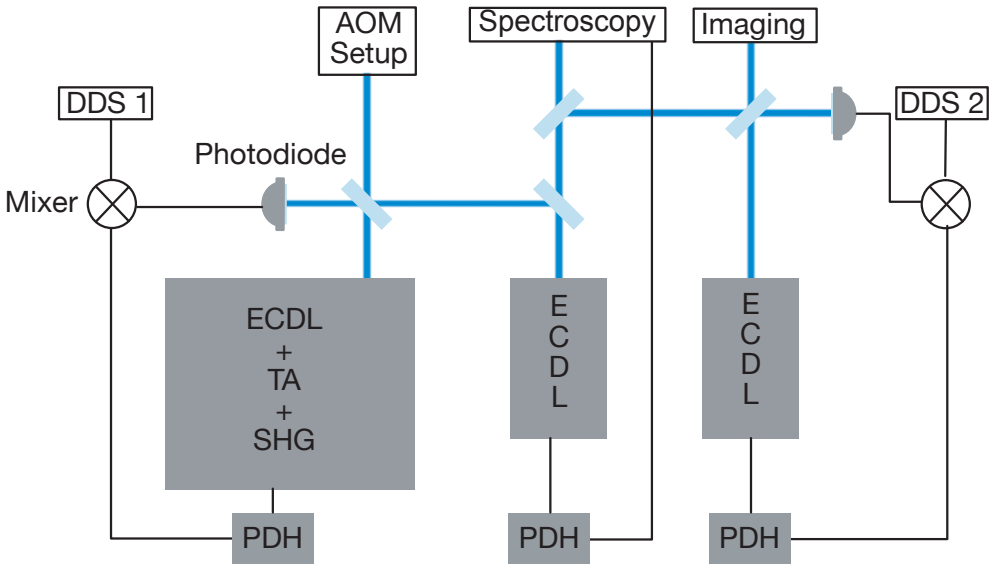

Figure 3.7: A potential future setup for the blue laser system. The left laser system shows our existing laser system extended by a separate spectroscopy system and imaging laser. By changing two Direct Digital Synthesizers (DDS), the detunings between the systems could be adjusted in real time.

larger ($\approx$ 12 MHz compared to $\approx$ 2 MHz), which makes repumping without a lock much easier. Another scheme used by the *Ye* group [49] is to use two transitions. The $^3P_2 \rightarrow {}^3S_1$ transition at 707 nm is used to repump the lost atoms in the metastable $^3P_2$ state, and the $^3P_0 \rightarrow {}^3S_1$ transition at 679 nm is used to repump the atoms that decayed from the $^3S_1$ into the undesired $^3P_0$ state. Recently, it has been shown that it may be possible to lock the 707 nm transition to an atomic signal observed in a hollow-cathode lamp [69].

We selected the final scheme mentioned above, in which simple ECDLs[7] can be locked with state-of the art wavemeters at sufficiently high accuracies [8].

[7] Both lasers are *Toptica* DL100 ECDL lasers together with the DL100 controller.
[8] We us a *HighFinesse* WS-7 wavemeter with multi-channel option to use it simultaneously for both laser. The quoted absolute accuracy is 30 MHz

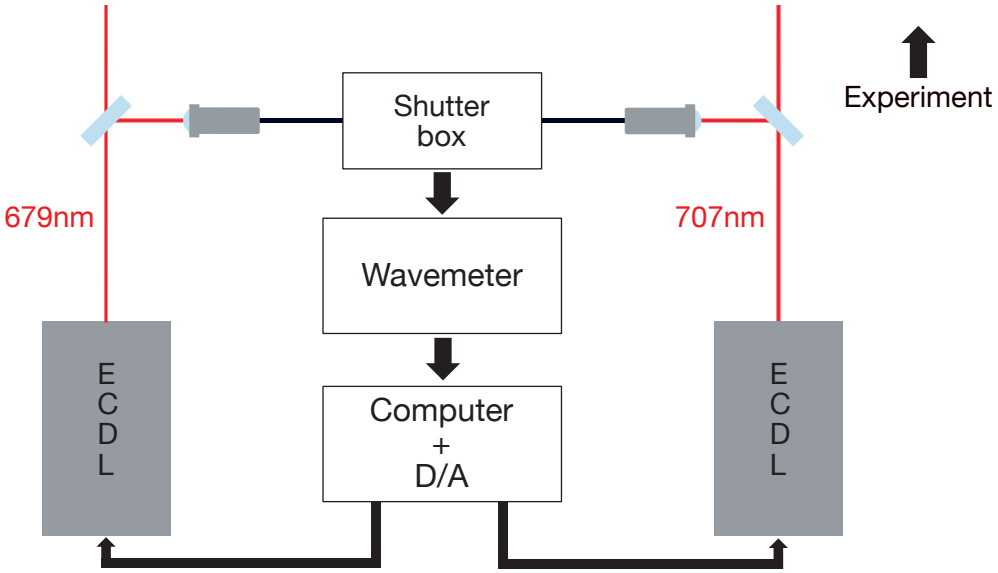

Figure 3.8: Locking scheme to lock repumper lasers to their respective atomic transitions. The two ECDL lasers send a negligible amount of power to the shutter box of the wavemeter. The wavemeter is connected to a computer with a D/A converter that feeds back to the lasers.

A schematic of our setup is shown in fig. 3.8. In order to optimize the performance of the repumpers, the laser intensity should be on the order of the saturation power over the the capture volume of the MOT (on the order of 1 cm^3). This is difficult to achieve with our current ECDLs, which are incapable of delivering high powers. The laser powers and the corresponding saturation powers are given in the following table:

	Linewidth [MHz]	**Sat. power [mW/cm^2]**	**Max. intensity [mW/cm^2]**
679 nm	1.5	0.59	3.0
707 nm	7.4	2.441	0.3

Table 3.2: Saturation powers for the two repumping transitions compared with the available laser intensities of the ECDLs in the experiment.

For fermionic strontium, the repump states also demonstrate hyperfine splitting. For the 707 nm transition, this is on the the order of 5.5 GHz. Our approach towards efficient repumping is to center the ECDL on its mode-hop-free range, and to modulate the frequency with the piezo of the ECDL as fast as possible to effectively spread the laser power over a frequency comb spanning 5.5 GHz. We can then lock to the wavemeter since its integration time is slower than the modulation described. However, since the span of the frequency comb is very power inefficient, an alternative approach is shown in ref. [70], in which a broadband EOM addresses all hyperfine levels with the desired detuning from the center transition and could be easily implemented.

3.2 Red System

The primary challenge involved in the red laser system lies in the 7.4 kHz linewidth of the $^1S_0 \rightarrow {}^3P_1$ transition, which introduces two major obstacles. First, since this linewidth is two orders of magnitudes smaller than the short-term stability of a state-of-the-art ECDL, observing a spectroscopy signal would require pre-narrowing of the laser. Second, a challenge is the spectroscopy signal of such a narrow transition itself. The Doppler broadening in a thermal gas drastically lowers the contrast in usual spectroscopy techniques, rendering the the observation quite challenging. However, this has been realized by several groups ([45, 49]).

Since pre-narrowing would have been necessary, we decided to go a different route. By narrowing down the laser with a Fabry-Perot Cavity that not only has a narrow linewidth on a short time scale but also provides a good absolute frequency reference, a lock to a spectroscopy signal can be avoided entirely.

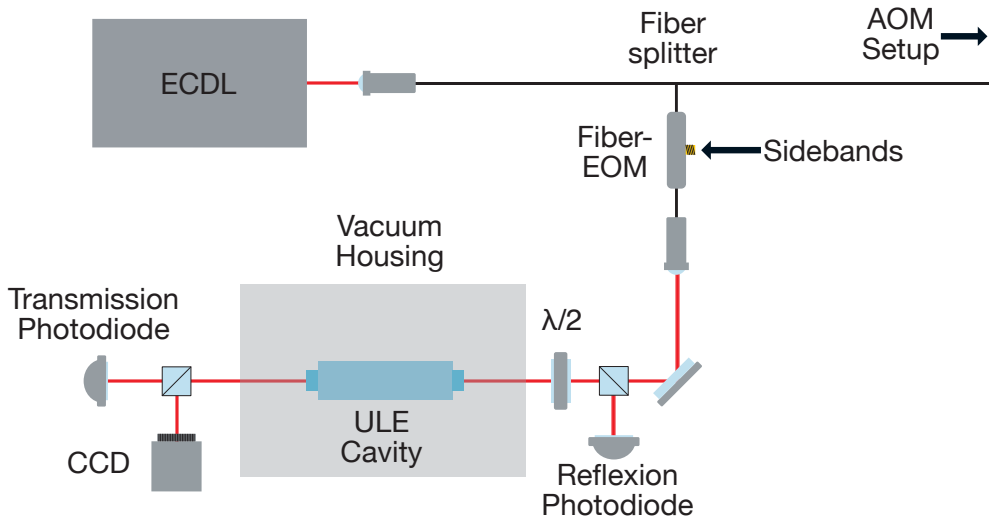

Figure 3.9: Red laser setup to lock to the ULE cavity. A negligible amount of the ECDL output power travels through a broadband fiber-EOM to the vacuum-housed cavity. The PBS and $\lambda/2$ waveplate are used to monitor the back-reflection and function as an additional isolator. The transmitted light after the cavity is split between a CCD camera and a photodiode. The camera is used to ensure that the laser is locked, and the photodiode finally allows the laser to be locked to the cavity transmission line.

Cavities using Ultra Low Expansion (ULE) glass have shown tremendous improvements over the last few years, capable of achieving linewidths on a subhertz level which has become quite standard [71]. By using the zero-crossing of the temperature

[9] The used ECDL is a *Toptica* DLpro with an especially narrow AR coated diode. The cavity system is from *StableLasers Inc.*, offered as a turn-key solution including the optics, optoelectronics, electronics and the vacuum housed ULE cavity.

expansion coefficient, absolute frequency stabilities on the order of ≈ 1 Hz per day can be achieved. Our system is shown in fig. 3.9[9]. Besides the cavity, the core of the system is a broadband EOM that offers the flexibility to change the laser frequency from the absolute frequency reference of the cavity to the desired wavelength of the transition. This is illustrated in fig. 3.10. In addition, the EOM is used to imprint the sidebands for the PDH lock to the cavity transmission line respectively the corresponding EOM sideband.

The electronics enabling such fast feedback include a synthesizer that mixes the offset frequency with the signal of the local oscillator for the PDH lock, and a *Toptica* Falc - an extended PID controller with several integrators and a bandwidth of up to 10 MHz. The finesse of the cavity is approximately $20,000$, which results in a cavity linewidth of around 75 kHz. Quoted by *StableLasers inc.*, this should ultimately allow for linewidths of the locked laser of below 1 kHz, while the the cavity drifts less then 50 kHz per day.

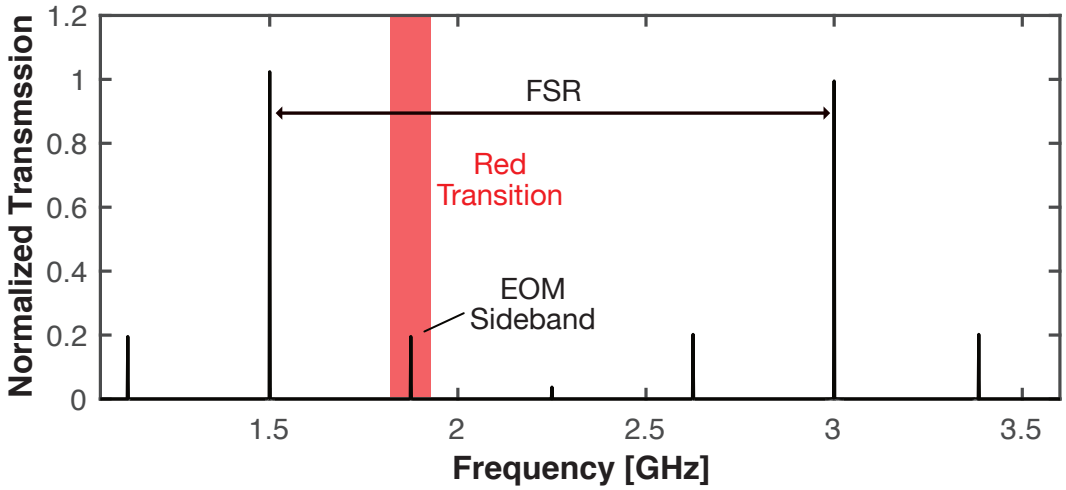

Figure 3.10: The absolute frequency of the cavity modes is fixed by the length of the resonator. The Free Spectral Range (FSR) between the equidistant modes is 1.5 GHz. The broadband EOM allows for sidebands to be placed over nearly the whole range ($\pm$20 to $\pm$750 MHz), which finally allows the laser to be locked to an arbitrary setpont (e.g. the bare transition frequency of the ${}^1S_0 \rightarrow {}^3P_1$ transition).

3.2.1 AOM Setup

From the red laser system, we receive up to 14.5 mW. with regard to the low saturation intensity of 2.94 $\frac{\mu W}{cm^2}$, this is sufficient for simple operations on the ${}^1S_0 \rightarrow {}^3P_1$ transition. In order to increase the loading efficiency from the blue MOT to the red MOT, the laser light is artificially broadened by approximately three orders of magnitude. For a short time, this brings the saturation intensity of the red transition back to the order of normal Alkali atom intensities of a few $\frac{mW}{cm^2}$. Along with the large intensities we are

planning to use for sideband cooling (see chapter 6), we decided to amplify the ECDL with a TA built in-house[10]. This gives us up to 150 mW of laser power after coupling the amplified beam into a fiber.

Following the fiber, this amplified light is split up in a manner analogous to the blue system. Since the linewidth of the red transition is three orders of magnitude smaller than the blue, the detunings for the different applications are all within 1 MHz. As a result, the AOM is needed only for modulation and for switching. It is worth mentioning that the noise and stability of RF sources (on a kilohertz level) must be considered. Here, we use DDS-based drivers [11] which include on-board frequency reference that should, in principle, provide long term stability on a level of a few hertz.

A diagram of the preliminary AOM setup is shown in fig. 3.11. We have already implemented one AOM to begin already exploring the influence of on-resonant light of the ${}^1S_0 \rightarrow {}^3P_1$ transition on the blue MOT to find the red transition.

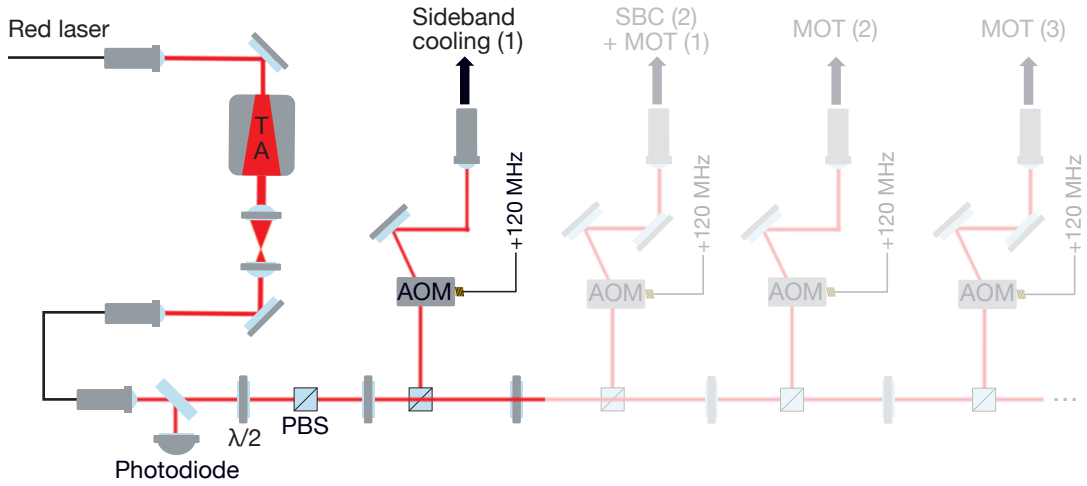

Figure 3.11: Preliminary AOM setup for the red laser. The output of the red laser system is amplified by a TA and coupled into the fiber to guide it to the splitting system. Long term, the light will be split to at least five fibers for different beams needed. The transparent part of the system has not been built thus far. The existing path is used to conduct initial tests on the ${}^1S_0 \rightarrow {}^3P_1$ transition.

3.3 Green System

The 515 nm laser light to create our tweezers (see magic wavelengths section) is provided by a frequency-doubled 1030 nm laser. Fortunately, 1030 nm lies within the range of operation of Ytterbium-doped fiber amplifiers; apart from 1064 nm, it is the most common high power near-infrared laser wavelengths.

[10] The used TA chip is from *Eagleyard* Model *EYP-TPA-0690*
[11] We use the *Time Base DIM-3000* driver

A novelty in second harmonic generation of infrared lasers is the use of mode matched poled PPMgLN crystals ([72, 73], which achieve doubling efficiencies on the order of 30 % without cavity enhancement. Not only does this simplify the design of the doubling systems, it also improves the beam quality of the doubled light due to a single pass through the surface of the crystal. These systems are commercially available [12], capable of delivering up to 10 W. For our purposes, they are ideal since we can use them (without fiber) to achieve a large power overhead for future scaling to larger sizes of tweezer arrays. A schematic of our laser system is shown in fig. 3.12.

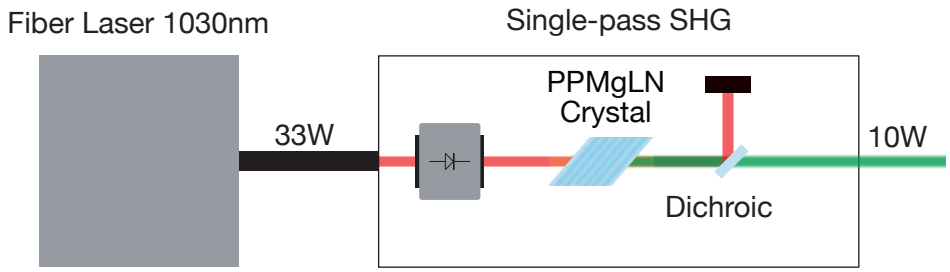

Figure 3.12: Doubling of 1030 nm light through a PPMGLN Crystal in a single pass configuration. The residual red light following the crystal is filtered by a dichroic mirror and the 515 nm light travels into free space out of the laser head.

[12] We use a laser system from *Azur Light Systems* with an output power of up to 10 W.

4 Apparatus

Simplicity, long vacuum lifetimes, and maximized optical access were the main goals for the design of the vacuum system of this experiment. This chapter introduces our vacuum setup, from the atom source to the glass cell.

4.1 Design

We aim to build an experiment which remains as simple and compact as possible, while maintaining properties such as high vacuum lifetimes and optical access. We designed our Ultra High Vacuum (UHV) system with the following considerations:

- To maximize the optical access to the trapped atoms, we use a glass cell to allow high Numerical Apertures (NA) from at least four directions.
- To maximize vacuum lifetimes while maintaining high atomic flux of strontium atoms, the source and the final main chamber must be separated. Here, advanced pre-cooling and confinement techniques such as 2D-MOTs and Zeeman slowers are needed.
- For simplicity and lower cycle times, the cold atom cloud should not be transported. This implies that the 3D-MOT will be loaded in the glass cell.
- By keeping the vacuum setup as small as possible, the whole setup can be mounted on a translation stage. This would allow for further changes in the setup without disturbing the sensitive optics around the glass cell through simply removing the chamber.

4.2 Atom source

For the atom source, we use a commercial solution from *AOSense*. This is an assembly consisting of (1) a nozzle oven that heats the atomic strontium and pre-collimates it with capillaries, (2) pumps to keep low vacuum conditions inside the atom source, (3) permanent internal magnets to generate magnetic fields for two 2D-MOTs and a Zeeman slower, (4) viewports with internal mirrors to guide the light through the 2D-MOTs, (5) a heated window for the Zeeman slower, and (6) a differential pumping stage. The whole product is delivered pre-baked under UHV conditions. A drawing of the atom source is shown in fig. 4.1

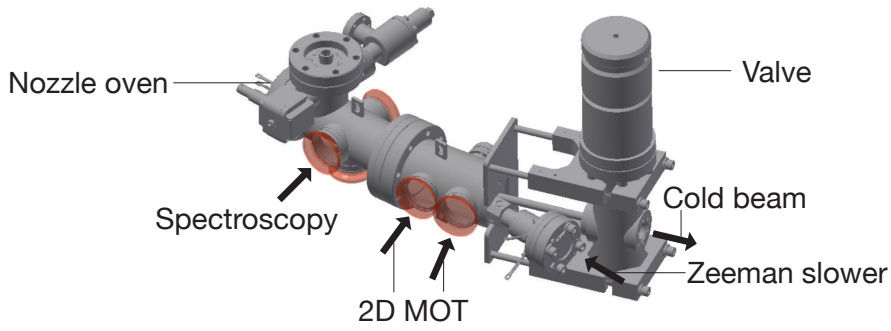

Figure 4.1: Drawing of the atom source from *AOSense*. The orange windows show the various access points to the atom beam. The deflected atom beam finally travels through the differential pumping tube that terminates in a Valve.

The spectroscopy window (see in fig. 4.1) provides access to test the performance of the oven. Here, we can observe the uncooled atom beam from the oven. The range over which the oven can be operated with practical values of hot atom flux is from 400 °C to 500 °C, which corresponds to flux between 1.5×10^{12} 1/s to 8.2×10^{13} 1/s. The quoted flux values were confirmed by measuring the absorption of the atom beam. Two typical absorption profiles are shown in fig. 4.2. It is remarkable that the absorption lines are narrower than that of a thermal cloud of atoms of the same temperature by a factor of ten, which demonstrates the effect of the collimating capillaries.

Following the spectroscopy window, the oven guides the hot atom beam between the magnets of the Zeeman slower inside the vacuum and enters the two 2D-MOTS, which angle the cooled atom beam with respect to the hot atom beam in order to guide it through the differential pumping stage.

For the 2D-MOTs and the Zeeman slower, we must prepare tailored beams with pre-simulated optimal detunings and given shapes. The chosen beam sizes and detunings are:

	Beam size [mm^2]	**Detuning [MHz]**	**Power [mW]**
Zeeman slower	10×10	-600	100
2D-MOT(1)	6×24	-40	15
2D-MOT(2)	6×24	-40	30

Table 4.1: Laser power of different cooling beams entering the atom source.

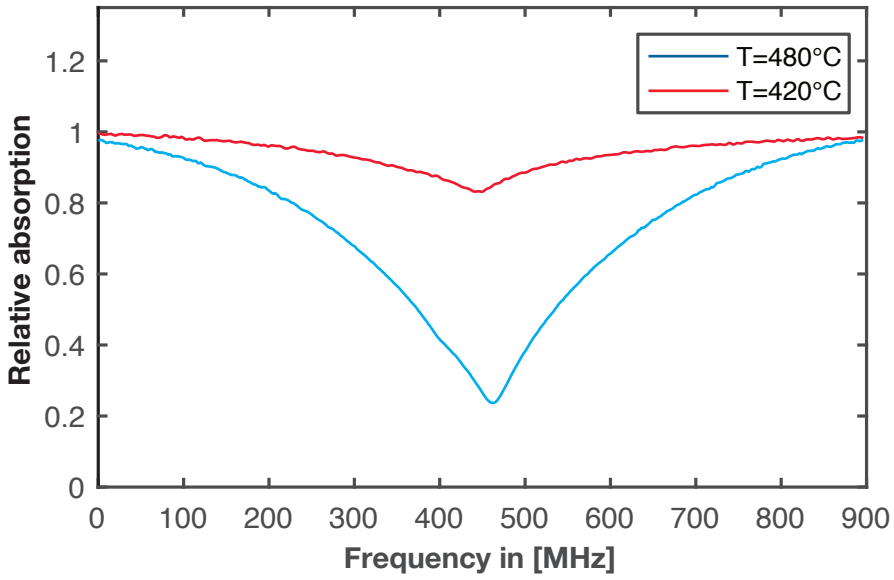

Figure 4.2: Absorption profile of the atom beam for two different oven temperatures scanned over 900 MHz. The full width at half maximum (FWHM) is on the order of 100 MHz.

4.3 The UHV system

In order to achieve low pressures on the order of 10^{-11} Torr, we selected an intermediate section of the vacuum system between the atom source and the glass cell, dedicated to reaching higher pumping speeds. The final design is shown in fig. 4.3.

The main source of atoms within the intermediate chamber is the conducted pressure of the atom source through the differential pumping stage. By varying the temperature of the oven from 350 °C to 480 °C, the pressure inside the atom source rises from 1.1×10^{-10} Torr to 1.2×10^{-8} Torr. This pressure is dominated by outgasing hydrogen inside the heated elements of the oven section. To maintain pressures on the order of 10^{-11} Torr independently of the oven temperature, we estimated a required pumping speed of 500 L/s to oppose the flow through the differential pumping stage. To achieve this, we selected a Titanium sublimation pump [1] for inside the chamber, as well as an additional ion pump [2] to enhance pumping of noble gases. With the estimated surface area of 550 cm^2, we estimate a pumping speed of 1400 L/s, which would be sufficient to achieve desired pressures on the order of 1×10^{-11} Torr or lower.

To measure the pressure in the main chamber, we use the ion pump current. Under the assumption that the pressure is dominated by one type of atom/molecule (typically Hydrogen molecules in similar setups), the current can be directly translated into a pressure. By varying the oven temperature from 20 °C to 480 °C, we measure

[1] *Gamma Vacuum* Model *360819* with 3 filaments
[2] *Gamma Vacuum* Model *75SCX*

pressures which increase from 2×10^{11} Torr and 4×10^{11} Torr. Thus, the pumping speed within this range is sufficient for eliminating the atom source atom flux. At temperatures beyond 480 °C, we measure a pressure which rises monotonically.

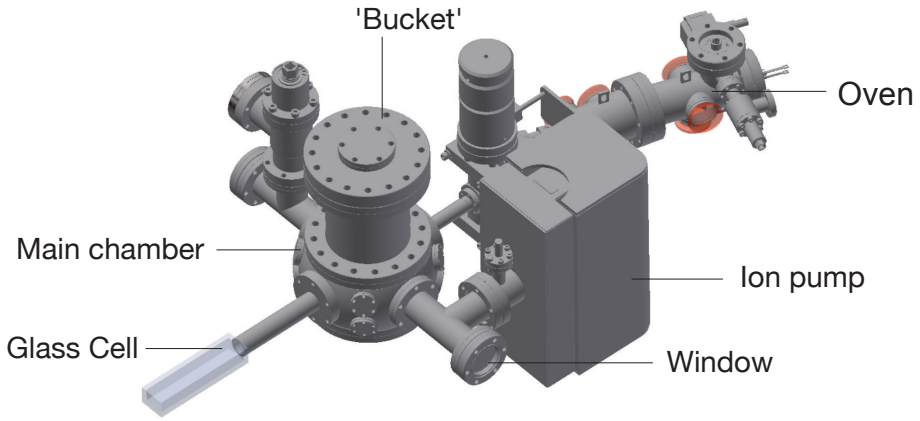

Figure 4.3: CAD drawing of the vacuum setup of our experiment. The 'Bucket' shows the attached vessel to increase the volume for the Titanium sublimation pump, which is not shown in the figure for visibility purposes. The left tee enables access to the vacuum, and the right tee is dedicated for the ion pump. Both tees have windows on the ends to be able to observe the atom beam. The main chamber is connected to the oven with a short bellows .

The final pressure in the glass cell - which sets the lifetimes of the atoms - is then determined by the balance between the outgasing of the glass cell and the effective pumping through the metal-to-glass transition due to the low pressure of the main chamber. Here, lifetime measurements of the atoms is the most precise indicator to measure this. This is shown in chapter 7.

4.3.1 Baking procedure

Since the baking procedure of a UHV system is a controversial topic, our approach will be briefly discussed.

The main purpose of this procedure is to rid the vacuum setup of remaining water. In principle, this can be achieved with any temperature above 100 °C, while higher temperatures can only accelerate the baking procedure. Similar work as shown in ref. [74] demonstrate that baking at temperatures beyond 300 °C can further improve the vacuum. As a result, we decided to bake all steel sections of the setup at 400 °C, which includes the main chamber, the tees, and the bucket. For this, we closed all open flanges and replaced all sensitive components (such as the glass cell and the viewports) with blanks. During the high temperature bake, we decided to keep the setup under vacuum by keeping it connected to a turbo-molecular pump.

After several days, we assembled the whole setup including the glass cell, all pumps, and the atom source, and proceeded to bake the entire experiment. Here, the temperatures permitted were much lower. Since the glass cell is optically contacted, we were able to heat it up to 280 °C to get as clean a vacuum setup as possible. We maintained these temperatures for approximately two weeks before we began cooling the entire setup, which spans an entire day.

4.3.2 Translation stage

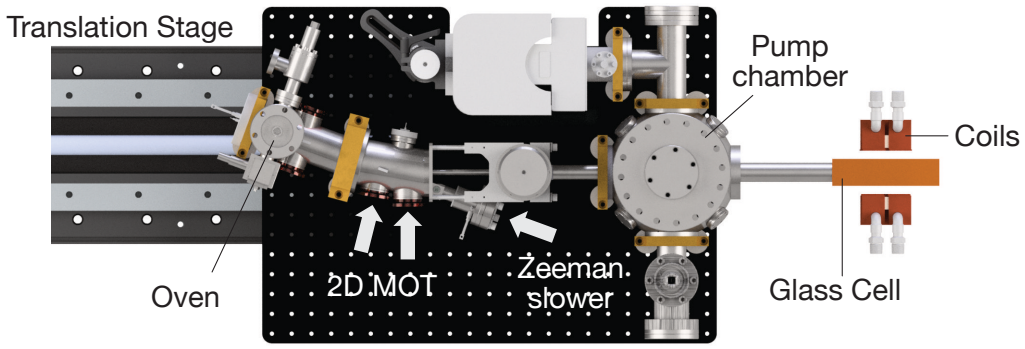

Figure 4.4: CAD drawing of the experimental setup with the breadboard that hosts the experiment, as well the translation stage that allows the experiment to be moved to the left end of the optical table.

A special feature of our setup is its compactness. The whole vacuum setup (including the atom source) is mounted on a 584 mm×432 mm aluminum breadboard [3], which can be mounted further on a translation stage [4]. This is shown in fig. 4.4. This allows us to translate the vacuum setup from the center to the end of the optical table, within a distance of 107 cm. This enables possibilities such as changing the glass cell or rebaking the chamber without disturbing the optics surrounding the glass cell. It has also simplified the alignment of our high resolution objectives, which has been extremely helpful thus far.

[3] *Base Labs tools* custom made
[4] *LinTech* Model *251242-WC0-1-S021-M00-C000-L00-E00-B00*

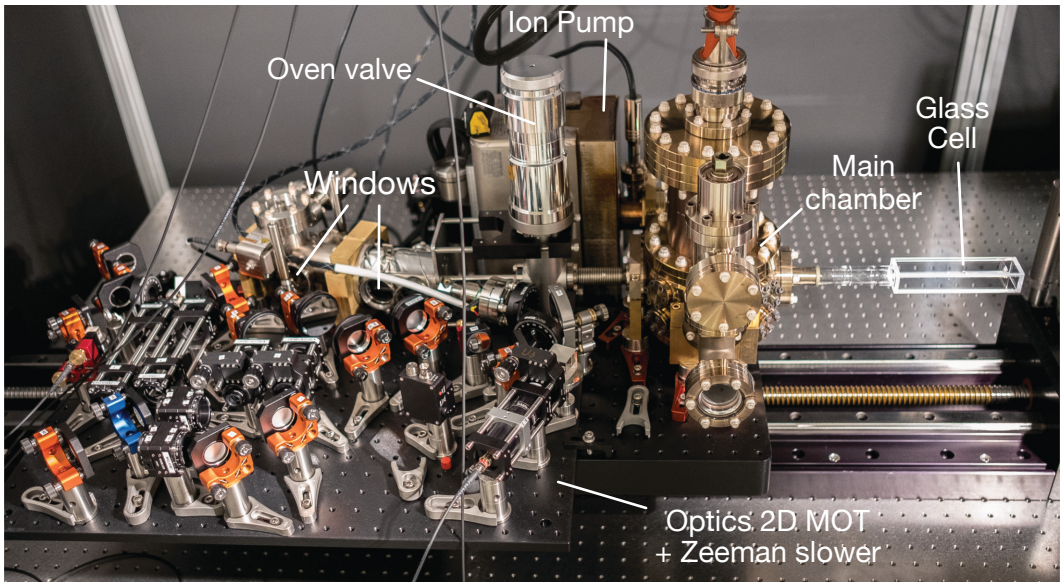

Figure 4.5: Picture of the assembled vacuum setup mounted on the translation stage. The optics for the Zeeman slower and the 2D MOTs are attached to the main breadboard to move along the translation stage. The translation stage is retracted, which makes it possible to work on these optics.

4.3.3 Glass Cell

The core of the entire experiment is the glass cell [5]. Here, we trap the atoms in the 3D MOTs and perform high resolution manipulation of individual atoms.

The cell is made of quartz glass, where each surface of the rectangular cuboid is optically contacted. As discussed previously, this permitted baking of the entire setup at temperatures up to 280 °C. The quartz glass is also beneficial for applications with UV light, since its transmission at wavelengths of < 350 nm is higher in comparison to high-tech glasses such as N-BK7. One of the wide, outer surfaces of the glass cell is AR coated, which enhances the transmission between 461 nm and 915 nm. A drawing of the glass cell with its dimensions is shown in fig. 4.6.

[5] *Japan Cell* Model *custom*

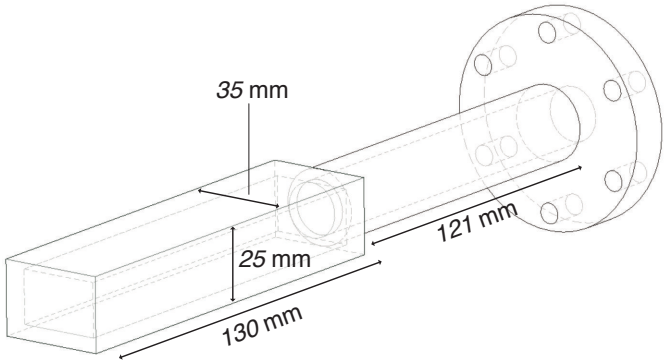

Figure 4.6: Dimensions of the glass cell. The two wide surfaces with side lengths of 35 mm allow for theoretical numerical apertures of up to 0.8, while the narrower surfaces of 25 mm allow for NA's of up to 0.6. The metal-to-glass transition has a length of 121 mm, which simplifies the beam routing surrounding the glass cell.

The thicknesses of the glass plates of the wider and narrower surfaces are 3.5 mm and 4 mm, respectively, while the flatness of the surfaces is $\lambda/8$ for the uncoated surfaces.

4.4 Optical layout

In our current setup, we aim to explore the blue MOT on the ${}^1S_0 \rightarrow {}^1P_1$ transition to see if we are already capable of trapping our first atoms in optical tweezers using this relatively hot MOT. This allows us to test the performance of our vacuum setup, providing insights regarding decisions for future upgrades to our system (which will be discussed in chapter 9). The beams of the setup are shown in fig. 4.7, with the corresponding beam sizes and saturations are listed in table 4.2.

The most distinctive feature of our setup is the two high resolution objectives[6], placed above and below the glass cell. Taking into account the thickness of the glass surface, they have a working distance of 15.1 mm, which allows for a distance of 2.5 mm between the objectives and the glass cell. The high resolution setup will be discussed in further detail in chapter 6. Due to the geometric restrictions of the objectives, however, the typical beam configuration with three orthogonal beams is not possible.

Here, we decided to compromise on the two MOT beams in the plane of the two objectives, and angle them such that they intersect at a 120° angle. This allows for beam diameters on the order of $\approx$ 15 mm without clipping on the objectives, which should allow for good MOT performance.

[6] *Mitutoyo* Model *G Plan Apo 50X*, NA=0.5

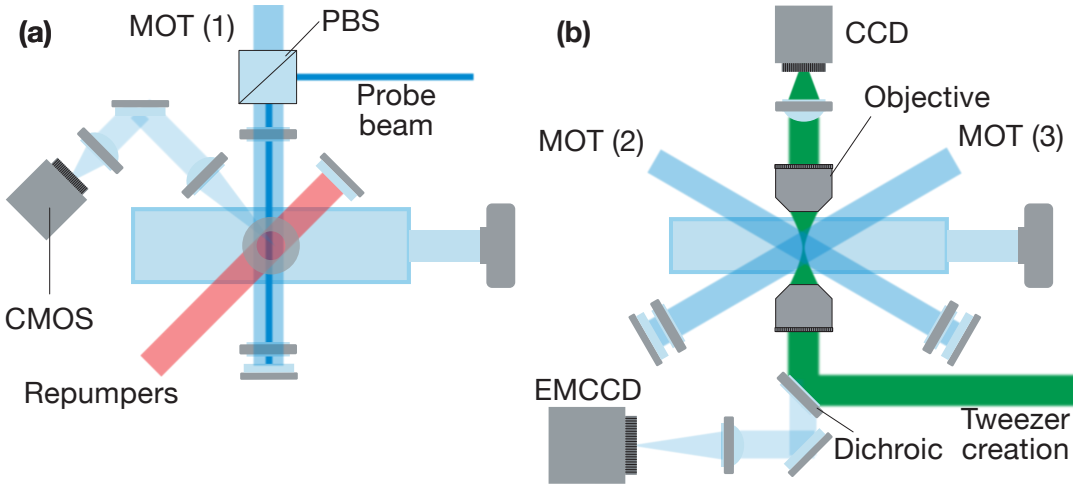

Figure 4.7: **(a)** Top view of the optical layout. For simplicity, the coils are excluded. The MOT axis is overlapped with a smaller probe beam. Along one axis at 45° lie the overlapped repumpers, with the imaging system set up orthogonally.**(b)** Side view of the experimental setup. The MOTs intersect at a smaller angle than the typical MOT configuration. The incoming tweezer beam is shown in green, which traverses both objectives before it is captured by the upper CCD camera. The fluorescence of the tweezers is collected by the lower objective and split by a dichroic to the lower left EMCCD camera.

Along the horizontal plane, we direct two overlapped repumper beams, retro-reflected to enhance the intensity. Orthogonal to the repumper beams, we built an imaging system to observe the MOT via fluorescence imaging, which can be collected by either a camera or an amplified photo diode (depending on whether spatial information regarding the MOT is needed in addition to numbers of atoms).

	Beam diameter [mm]	**Detuning [MHz]**	**Saturation parameter**
MOT (1)	18	-25	0.1
MOT (2&3)	18	-25	0.2
Probe beam	0.6	$+100... + 200$	30
Repumpers	20	0	$0.5 - 1$

Table 4.2: Beam size, detuning and saturation of all beams entering the glass cell.

For all larger beams, we used separate collimators from *Schäfter+Kirchhoff*[7] to avoid excessive use of telescopes and to simplify the optics surrounding the glass cell. The beams entering end exiting the objectives will be discussed in chapter 5.

[7] *Schäfter+Kirchhoff* Model *60FC-L series*

4.4.1 MOT Imaging System

To quantitatively evaluate our MOT, we built a low resolution imaging system with a 4f-system to image the atom cloud on a CMOS chip [8]. We de-magnify the image by a factor of two by selecting the focal lengths $f_1 = 100$ mm and $f_2 = 50$ mm (see fig. 4.8).

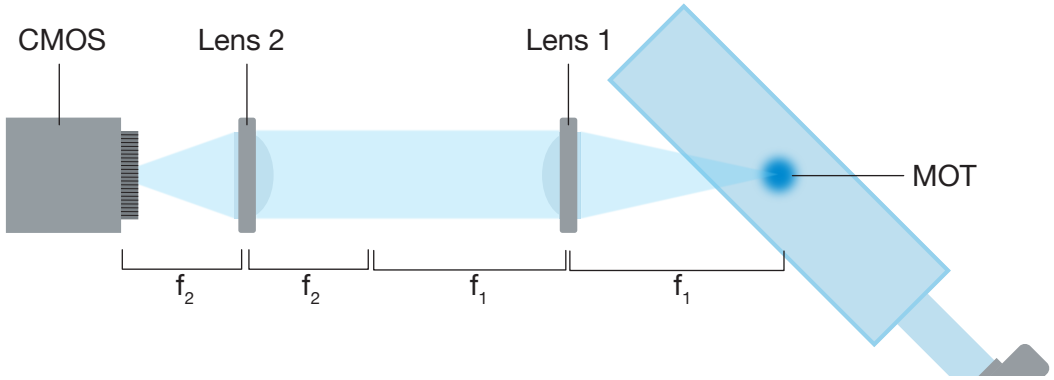

Figure 4.8: MOT imaging system to record fluorescence images of the MOT. The two plano-concave lenses (with diameters of 25.4 mm) form a 4f-system.

With these focal lengths and lens sizes of 25.4 mm, we achieve an effective NA of 0.126, which covers a solid angle Ω of 0.048 sr. This implies that our imaging system collects 0.38% of all emitted photons. Along with the Quantum Efficiency (QE) and the photon-to-digital count ratio of our camera [9], we arrive at a calibration factor of $\alpha = 1,970 \frac{\text{Photons}}{\text{Pixelcount}}$. This will become important later when evaluating the recorded MOT images.

4.4.2 Coils

To generate the magnetic field gradients required for the MOT, which are on the order of 50 G/cm, we use two copper coils in an anti-Helmholtz configuration. Given the currents necessary for these gradients, the coils require active cooling, which we achieve by placing them into a water-cooled copper holder (shown in fig. 4.9).

The bare coils[10] have inner and outer diameters of 40 mm and 60 mm, respectively. With 74 windings, their calculated resistance is 0.3 Ω. By applying currents of up to 25 A [11] with a distance of 6.5 cm between the inner surfaces of the coils, we achieve magnetic field gradients of up to 70 G/cm.

[8] *Pointgrey* Model *GS3-U3-32S4M-C*
[9] This can be calculated by the capacity of each pixel (which, in our case, is given as $10,482e^-$) and the pixel bit-depth
[10] The coils are winded by *Custom Coils, Inc.*
[11] We us a power supply from *Delta Elektronika* Model *SM 35-45*

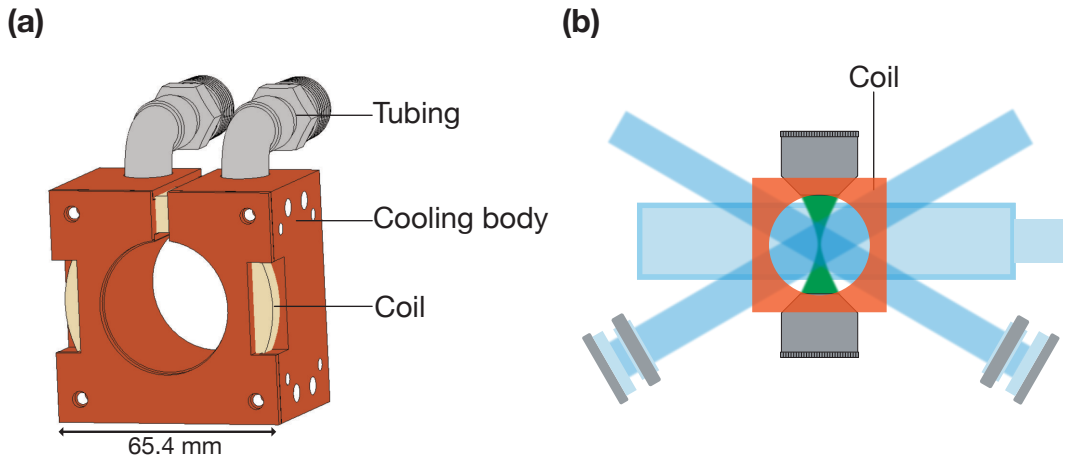

Figure 4.9: **(a)** Drawing of the copper holder with the inserted coil. **(b)** Coil included in the optical layout.

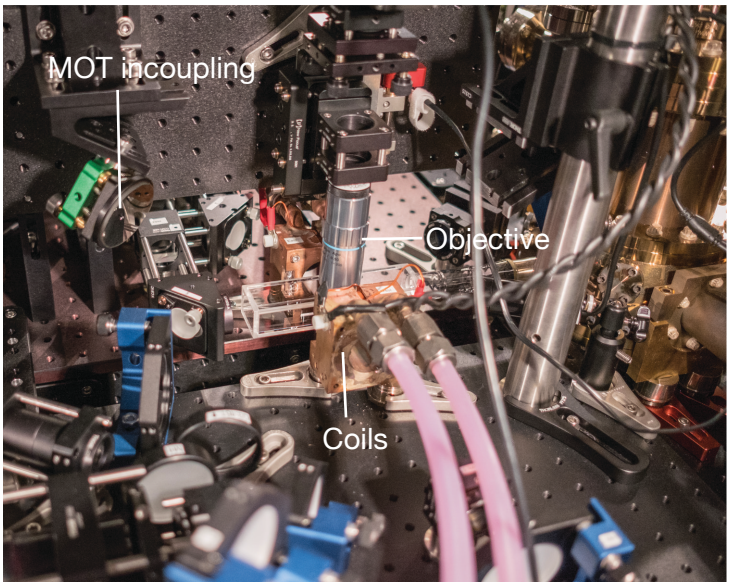

Figure 4.10: Photo of the current setup with both objectives included. In this picture, an older version of the imaging system on the end of the glass cell is shown. The in-coupling mirror demonstrates how the 60° beams are routed.

5 Generation of Tweezer Arrays

Since the 515 nm laser system and our optical layout with the two high resolution objectives have already been introduced, this chapter will discuss how we experimentally realized near-diffraction-limited tweezers as well as the techniques used to characterize these tweezers on the order of hundreds of nanometers. Building on this, we will introduce the usage of Acousto-Optical Deflectors (AODs) to multiply optical tweezers through multi-tone RF signals. This is already demonstrated in ref. [28].

5.1 Diffraction-limited Tweezers

The classical usage of an objective is to image an object that emits light. In the limit of an infinitely small object, the image produced by the objective is the point spread function (PSF), the smallest feature that the imaging system is capable of producing. The out-going beam of an objective would be a uniform wavefront with the size of the back aperture of the objective. Since we want to generate the smallest traps possible that the objective can produce, we want to reverse this and direct the largest possible beam into the objective. The geometry of the tweezer (i.e. the out-going beam) then follows the same formulas that are already well-known from imaging theory [**?**].

For our NA=0.5 objectives, we expect, at a wavelength of $\lambda = 515$ nm, a transverse and longitudinal tweezer waist (both defined by a $1/e^2$ threshold) of:

$$\begin{aligned} w_{\text{transverse}} &= 438 \text{ nm} \\ w_{\text{longitudinal}} &= 2873 \text{ nm} \end{aligned} \tag{5.1}$$

In practice, however, it is easier to work with an input Gaussian beam, which changes the absolute size and shape of the beam. Here, the size of the tweezer can be calculated using Fourier optics (as shown in ref. [75]) and is on the order of 10% larger than the Abbe limit, and is quite sensitive to the waist of the incoming Gaussian beam.

The relevant physical quantity is the trap frequency inside the tweezer. While - in theory - there is a one-to-one relation between the trap frequency and the structure size (assuming that the functional dependency is known), it is practical to define the tweezer by the curvature of the center of the tweezer, which can then be used to describe the trap frequency. With this, we can calculate a corresponding tweezer size, which we assume has a Gaussian shape. Here, it should be noted that the typical picture of Gaussian laser beams is not fully suitable in this context. The Gaussian beam that is clipped at an aperture (i.e. the objective) does not satisfy the conditions required by its relevant formulas, which can lead to wrong implications.

Experimentally, we investigated our tweezers by sending a collimated Gaussian 515 nm beam with a diameter of $\approx$ 4 mm into the objective, which is close to the

diameter of the back focal plane. After the objective, we use a 3.5 mm glassplate to imitate the glass cell, and then a high resolution objective [1] with an NA of 0.9 to image the tweezer. Due to the higher NA of this objective, this imaging system has a higher resolution (than the system used to create the tweezer), thus avoiding further convolution with another PSF of the same scale. By scanning the z-position of the NA=0.95 objective [2] across the waist of the tweezer, it is possible to image transverse profiles for different values of z, producing a 3D map of our tweezer. An illustration of this technique is shown in fig. 5.1.

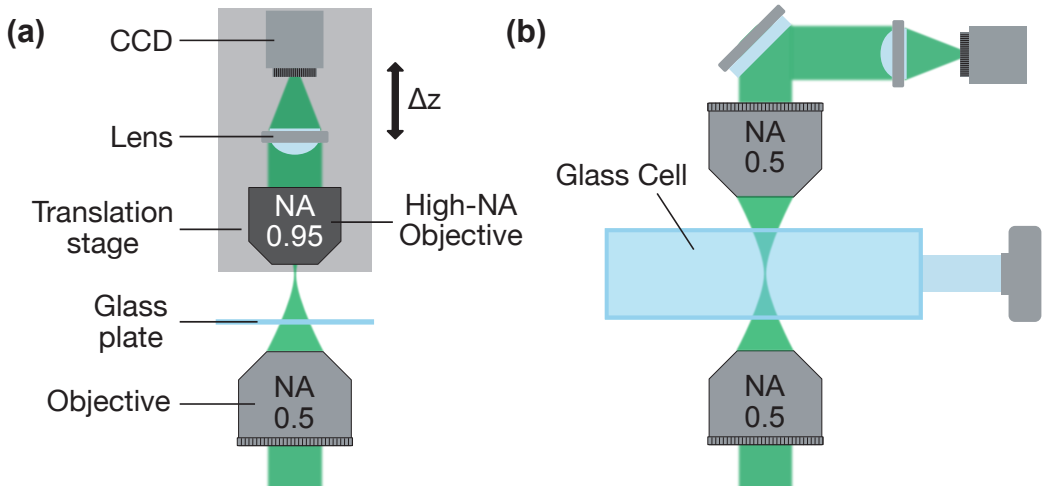

Figure 5.1: (a) Setup used to investigate our tweezer, which is imaged after the glass plate with a high NA (NA=0.95) objective. The imaging system is calibrated with a pinhole and allows for scanning along the axial direction (z) to model the 3D intensity distribution of the tweezer. **(b)** Setup in the final experiment. Here, the same objective is used to image the tweezer. This light is also imaged on a CCD camera, which is used to ensure that the tweezer remains aberration free at any point during the experiment. Due to the same NA of the imaging objective and the objective used to create the tweezer, the information captured by this measurement is limited.

It is important to note that this measurement is only valid near the waist of the tweezer, where the wavefront is flat. It is only at the waist where the imaged plane corresponds to the transverse profile of the tweezer.

With this technique, we finally extract the longitudinal and transverse curvatures by fitting a Gaussian to the relevant part of these profiles. Following this, the measured values for our tweezers are:

[1] *Nikon* Model *PLAN FL 100X OBJECTIVE, NA=0.9*
[2] We move the objective with a picomotor actuated stage from *Newport*

$$\begin{aligned} w_{\text{transverse}} &= 536\ \text{nm} \\ w_{\text{longitudinal}} &= 3,806\ \text{nm} \\ \frac{\omega_{\text{transverse}}}{\omega_{\text{longitudinal}}} &= \frac{w_{\text{longitudinal}}}{w_{\text{transverse}}} = 7.1(6.5) \end{aligned} \tag{5.2}$$

where $\omega_{\text{transverse}}$ and $\omega_{\text{longitudinal}}$ are the trap frequencies, and the value in the bracket is the theoretical ratio calculated using Fourier optics. The experimental data that was used for these measurements is shown in fig. 5.2. The measured transverse waist of the tweezer (of 536 nm) as well as the ratio of trap frequencies (of 7.1) is off by 10% compared to theoretical calculations. This is unsurprising due to high sensitivity to aberrations [76], and is quite comparable to tweezers created by other groups [76, 77]. The remarkable difference is the size of the tweezer, which is intrinsically smaller due to the wavelength of 515 nm in comparison to Rubidium experiments (in which the tweezer wavelength is typically between 805 nm and 850 nm). The smaller tweezer sizes result in an increase in trap frequencies. In contrast, the ratio between transverse and longitudinal confinement is influenced only by the NA of the objective.

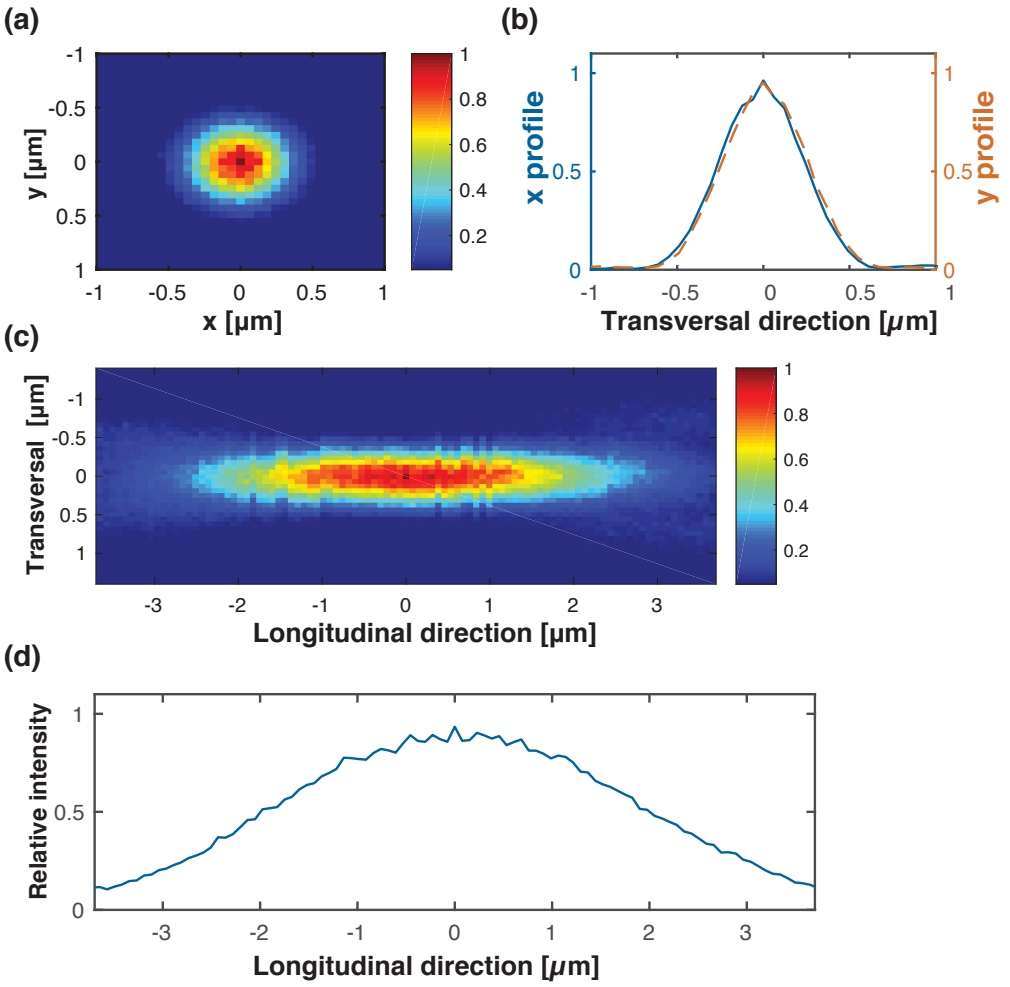

Figure 5.2: **(a)** Transverse profile of the tweezer imaged with the CCD camera via the second objective. The amplitude is normalized to the peak intensity. **(b)** Transverse intensity profile integrated over one dimension to extract the profile of the corresponding direction. For the final evaluation of trap frequencies, only the interval within $\pm$ 100 nm are considered. **(c)** Longitudinal tweezer profile analogous to (a). **(d)** Longitudinal intensity profile calculated by finding the height of each transverse cut of (c). The trap frequencies are extracted by fitting only to the $\pm$ 1 μm interval about 0.

5.2 Acousto-Optical Deflectors

To pave the way for constructing arrays of tweezers, we decided to use an Acousto-Optical Deflector (AOD) that we drive with multi-tone RF signals, which allows for the generation of multiple beams simultaneously.

An AOD is an acousto-optical device that is quite similar to typical AOMs (which are used to shift frequencies), but is specifically designed to deflect beams. The underlying mechanism remains, in which the photons passing through the crystal of the device undergo elastic scattering events with phonons, which are generated by the RF field that drives the crystal. For a deflection angle θ_D, this means:

$$\sin(\theta_D) = \frac{\hbar \mathbf{k}_{\text{Phonon}}}{\hbar \mathbf{k}_{\text{Photon}}} = \frac{c}{v_{\text{Sound}} f_{\text{Photon}}} f_{\text{RF}} \tag{5.3}$$

where $\mathbf{k}_{\text{Phonon/Photon}}$ are the wavevectors of the light and sound waves, c is the speed of light, v_{Sound} is the speed of sound in the crystal for the relevant propagation mode, and f_{RF} is the applied RF frequency. Therefore, in order to maximize the deflection bandwidth $\Delta\theta_D$ of an AOD, it is favorable to have a low speed of sound and a large frequency bandwidth Δf_{RF}.

This is precisely how shear wave AODs work [78, 79] - by using a slow shear wave along the $[110]$ axis in a TeO_2 crystal, the deflection is strongly increased. As a result, the anisotropic nature of this scattering process allows for a strongly extended bandwidth (of up to 50 MHz) to be reached.

The final resolution of the AOD (i.e. the number of distinguishable light beams that can be produced by the AOD) is set by the ratio of the deflection bandwidth to the divergence of the incoming light beam. Following Fourier optics, this defines the ratio between the maximum distance between light beams and the size of the beam itself in the Fourier plane. Ideally, an AOD would also have a large aperture to allow for large beams, thus minimizing the divergence of the the largest incoming beams. A measure for the resolution can then be defined, assuming the divergence of a Gaussian beam by:

$$N = \frac{\Delta\theta_D}{\theta_{\text{Beam}}} = \frac{2\Delta f_{\text{RF}} w_{\text{Beam}}}{v_{\text{Sound}}} \tag{5.4}$$

where w_{Beam} is the waist of the incident beam. For our AOD[3] with an aperture size of 7.5 mm^2, this corresponds to a resolution of 577 beams. For simplicity, we use the AOD with a beam size of 4 mm since the back focal plane of our objective has the same diameter, which still allows for several hundreds of resolved beams.

To map the deflection in the AOD to spatially distinguished tweezers, we built a 4f-telescope to image the deflection plane of the AOD with a 1-to-1 telescope to the back focal plane of the objective. In the simple picture of Fourier optics, this implies that the 4 mm beams with various incident angles are finally mapped to small tweezers, separated by a distance proportional to the difference in their incident angles. This is illustrated in fig. 5.3.

[3] *AA Opto Electronic* Model *DTSX-400* crystal cut for 515 nm

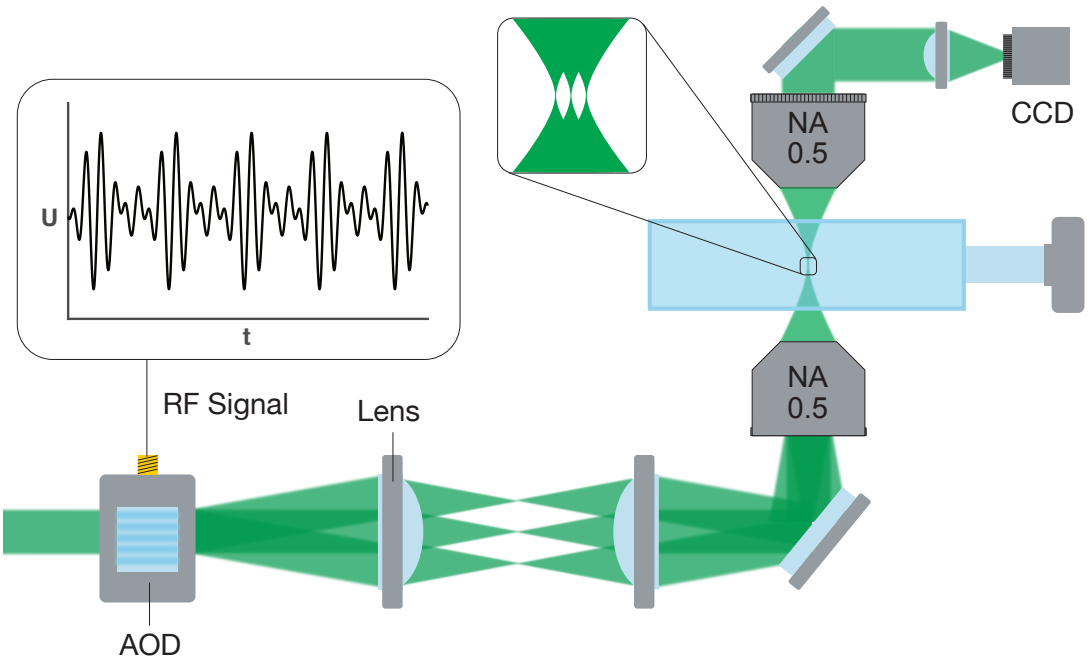

Figure 5.3: Illustration of our 4f-system that images the deflection plane of the AOD to the back focal plane of the objective. The two lenses have the same focal length of 250 mm, which was selected to be large to simplify the alignment process. The three different beams are achieved through the superposition of three equidistant frequency tones that are sent to the AOD.

By sending multiple frequencies to the AOD simultaneously, the crystal becomes occupied by phonons which correspond to the different frequencies. In the first order, this is simply linear - the AOD deflects each beam independently, the intensity of which depend only on the single Fourier components of the RF signal. In the most general form, the waveform is:

$$U(t) = \sum_{i=1}^{N} A_i \sin(2\pi(f_{\text{offset}} + i\Delta f + \phi_i)) \tag{5.5}$$

where N is the desired number of tweezers, A_i is the amplitude of each RF tone, f_{offset} is the offset frequency of the AOD, Δf is the frequency spacing between the tweezers, and ϕ_i is the individual phase of each component.

For $N\Delta f$ less than the bandwidth of the AOD, this RF waveform - in principle - would generate an array of equidistant tweezers, which can be uniformized by simply adjusting the amplitude A_i for each frequency component. This would compensate for the deflection efficiency of the AOD, which is independent of the individual phases ϕ_i. In reality, this simplified picture breaks down. In particular, the system is strongly influenced by non-linearities in the regime of large numbers of tweezers and high desired deflection efficiencies. In the extreme case for our RF electronics, the same phase

is selected for all frequency components, resulting in a pulsed RF signal which is unfavorable for the piezo-electronics and for amplification. On the other hand, the crystal of the AOD itself demonstrates nonlinear behavior; at high RF powers, higher order frequency mixing can be observed. These phenomena are reported in more detail in ref. [28]. This has been irrelevant for us thus far since (1) we use the AOD only for low tweezer numbers, and (2) we have a relatively high power laser system. As a result, we can avoid such effects simply by using smaller deflections. To avoid electronic non-linearities, random phases are selected for each RF tone. By fine-tuning the amplitudes A_i, it remains possible to create small, uniform arrays. An image of a tweezer array generated by our setup is shown in fig. 5.4.

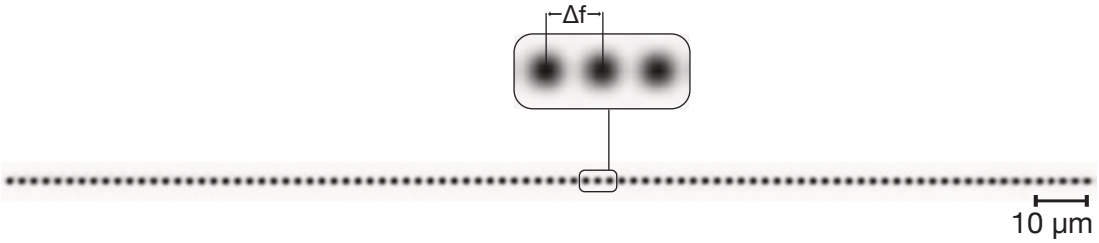

Figure 5.4: Image of an array of 90 equidistant tweezers imaged by the second *Mitutoyo* objective on a CCD camera. The frequency spacing between the tweezers is 556 MHz, which is the equidistant spacing over the bandwidth of 50 Mhz. This corresponds to an inter-tweezer spatial separation of approximately 1.5 μm.

5.2.1 RF Electronics to realize tailored frequency combs

The main advantage of using AODs is their fast respond time (on the orders of 10 μs), which is limited by the amount of time required by a RF wave to travel through the crystal. This is required to rearrange the array in real-time, as demonstrated in ref. [28]. Modifying such a complex RF waveform on this timescale is quite challenging not only digitally but also on the analog side, since the size of the data becomes large very quickly.

In order to lay out the requirements for the RF system, the required timescales and corresponding data volumes are demonstrated in table 5.1. For this, we assume a device with a sampling rate of 200 MS/s, which is a realiztic requirement for our bandwidth of 50 MHz. The assumed depth of each sample point is 16 bits, since this is the typical standard used to avoid digitization errors. Finally, the assumed resolution in frequency space for the AOD is 1 kHz, which sets a required duration for a cyclic waveform of 1 ms. The rearrangement time is adapted from [28] of 3 ms.

	Time [μs]	Frequency [kHz]	Sample points	Data volume [Mb]
Singe sample point	0.005	200,000	1	2×10^{-6}
AOD response	6.5	153	1,300	0.0026
Cycling waveform	1,000	1	200,000	0.4
Rearrangement	3,000	0.33	600,000	1.2
1 second signal	1×10^6	0.001	2×10^8	400

Table 5.1: Relevant timescales with corresponding digital requirements for the RF electronics used for the AOD.

Ideally, the data transfer would be done in real time, which requires a transfer rate of 400 Mb/s between the digital evaluation of the imaging and the RF device. Since this lies at the limit for all commercially available connectors, we selected an arbitrary waveform generator (AWG) that is a PCI card [4], since the bandwidth of its internal PCI connectors is up to 2.8 GB/s. With this device, we wish to explore future possibilities for rearrangement of tweezers using AODs.

[4] *Spectrum Instrumentation* Model *M4i.6622-x8*

6 Imaging technique

In this chapter, we propose a scheme for fluorescence imaging of strontium atoms in tweezers, which must be capable of imaging single atoms on a time scale of 100 ms without heating the atoms out of the tweezer. This is needed for realistic rearrangement schemes [27, 28], since two images of the same atom must to be captured on a timescale over which vacuum-induced losses can be neglected. For this, we make use of the narrow ${}^1S_0 \rightarrow {}^3P_1$ transition to cool the atoms inside the tweezer, while we image them with the broad ${}^1S_0 \rightarrow {}^1P_1$ transition. This scheme will be described in the follow chapter along with our initial numerical simulations to demonstrate the potential of this technique.

6.1 Single atom fluorescence imaging

Currently, the concept of fluorescence imaging of single atoms is realized with a large number of various species of atoms. However, the underlying principle remains consistent: the atom scatters resonant light, which is collected by an imaging system. In general, since the recoil of the scattered light heats the atom, the challenge is to collect a sufficient number of photons prior to the atom exiting the trap. This was realized for the first time inside a MOT, due to the trap depths of a few Kelvin [80]. However, the spatial resolution of the atom trapped in the MOT is too low for experiments such as QGMs and tweezer sequences.

The first deterministic loading and imaging of single atoms confined in an optical tweezer was achieved by trapping single Rubidium atoms projected with a high NA objective and imaged with the MOT beams. This provided access to the spatial information of the atom for the first time [25].

In QGMs, imaging is much more challenging. Since the lattice spacing must be on the order of 500 nm to reach the strongly correlated regime, the point spread functions of neighbouring lattice sites through the imaging system usually overlap. As a result, a larger signal-to-noise ratio is required to truly resolve single atoms in the optical lattice. Since the final depth of optical lattices is limited, additional cooling is also required. Here, rubidium has shown the ability for polarization gradient cooling inside of optical traps, which allowed for the construction of the first QGMs [17, 18], in which a few thousand photons per atom could be collected.

For modern tweezer experiments, the requirements are quite similar, in which the imaging time and the temperature inside the trap must be such that they permit an imaging sequence before the atoms interact [21, 26]. Here, typical time scales for imaging are on the order of tens of microseconds [21, 28].

Over the last few years, similar schemes for other atom species have been shown.

It should be noted that for potassium and lithium QGMs, suitable cooling processes must be different from their respective scattering processes, which ensure the collection of photons. In both cases, coherent Raman sideband cooling have been successfully implemented [81, 82], in which a Raman process is used to cool the atoms, and a pump process is used to collect photons. Similar to our proposed scheme, the imaging technique in ref. [83] uses the intercombination line of Ytterbium for cooling, and further enhances the number of scattered photons using the broad singlet transition.

Strontium atoms in 515 nm traps

The two main transitions allowing for cycling from the ground state (thus suitable for imaging of atoms) are the $^1S_0 \rightarrow {}^1P_1$ transition (at 461 nm) and the $^1S_0 \rightarrow {}^3P_1$ (at 689 nm), both of which have been discussed in chapter 2.

The initial observation is that the level structure for both transitions do not allow for explicit sub-Doppler cooling methods, in which imaging and cooling could be achieved using the same transition with a reasonable cycling speed. Alternatively, one could imagine Doppler cooling; however, this is not possible due to the extreme linewidths of the two transitions. While the $^1S_0 \rightarrow {}^1P_1$ is extremely broad (i.e. Doppler cooling on this transition would require very deep tweezer traps), the $^1S_0 \rightarrow {}^3P_1$ is so narrow that scattering photons on this transition would result in an extremely slow imaging scheme. Table 6.1 illustrates the energy scales (and thus the timescales) for a strontium atom in a typical tweezer.

	Frequency [MHz]	**Temperature [mK]**	**Blue recoil [$\frac{\hbar^2 k^2}{2m}$]**
$\mathbf{U_{trap}}$ **@2 mW**	22.2	**1.08**	**2,120**
$\omega_{\mathbf{trans.}}$ **@2 mW**	**0.203**	0.0093	**18.22**
$\omega_{\mathbf{long.}}$ **@2 mW**	**0.029**	0.0013	2.55
$\mathbf{T_D}$ **@461 nm**	15.25	**0.731**	**1,433**
$\mathbf{T_D}$ **@689 nm**	0.0037	0.000179	0.351
Recoil @461 nm	0.0011	0.00051	1.0
Recoil @689 nm	0.0047	0.00023	0.45

Table 6.1: Energy scales for a tweezer at 515 nm with an exemplary power of 2 mW, compared with the energy scales of the $^1S_0 \rightarrow {}^1P_1$ and the $^1S_0 \rightarrow {}^3P_1$ transition.

This table demonstrates the power of our tweezer at 515 nm; with 2 mW of laser power, we are able to achieve trap depths of 1 mK, which corresponds to recoil energies of 2,120 on the blue transition. This, for example, enables imaging on the blue transition of a ground-state-cooled atom. In addition, the trap frequencies are quite high - along both the transverse and longitudinal directions, they are already larger than the linewidth of the $^1S_0 \rightarrow {}^3P_1$ transition.

This enables the ability to address single trap levels, which we use in order to achieve resolved sideband cooling on the $^1S_0 \rightarrow {}^3P_1$ transition. Depending on its per-

formance, this could potentially realize higher cooling rates than one recoil per scattering event, which finally enables scattering of many photons on the ${}^1S_0 \rightarrow {}^1P_1$ transition while we cool continuously.

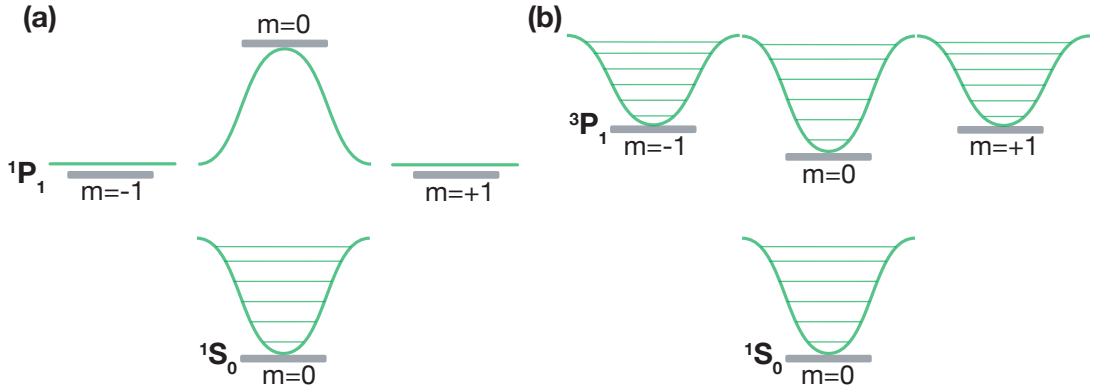

Figure 6.1: Light shifts illustrated for the two relevant states. **(a)** ${}^1S_0 \rightarrow {}^1P_1$ level scheme with light shifts for a given π polarization of the tweezer light. **(b)** ${}^1S_0 \rightarrow {}^3P_1$ level scheme for π-polarized tweezer light in magic conditions for the $m = 0 \rightarrow m = 0$ transition.

For this proposed cooling scheme, we need the magic wavelength conditions (as discussed in section 3.3 and illustrated in fig. 6.1), since addressing of a sideband independent of trap levels is only possible for the case in which the atom experiences the same trap in both the ground and excited states.

In the following sections, this cooling method is investigated quantitatively.

6.2 Cooling of strontium in deep magic traps

The coupling matrix element describing atom-light interaction for atoms trapped in a deep potential is different than in the Doppler cooling case (which is simply described as $\langle p_1 \mid e^{ikx} \mid p_2 \rangle = \delta(p_1 - p_2 - \hbar k)$) in several ways. Momentum p is not a good quantum number, since concepts such as momentum conservation (and consequently, Doppler shifts) no longer apply. In addition, the energy spectrum as well as the coupling strengths become discrete. Since these discrete levels are resolved in both the transverse and longitudinal directions (listed in table 6.1), this provides the possibility for efficient cooling. Fig. 6.2 illustrates the principle of sideband cooling for the simplest case.

A good figure of merit to quantify the coupling strength is Lamb-Dicke parameter $\eta = z_0 k_L$, where $z_0 = \sqrt{\frac{\hbar}{2m\omega_{trap}}}$ is the spread of the zero-point wavefunction and k_L is the k-vector of the cooling laser, projected on the trap direction [84]. For the exemplary tweezer in table 6.1, z_0 as well as the Lamb-Dicke parameter are $z_{0,r} = 17$ nm, $z_{0,l} = 44$ nm and $\eta_{0,r} = 0.15$, $\eta_{0,l} = 0.40$ (assuming the k-vector of the cooling laser is parallel

for both transverse and longitudinal directions). In both cases, the spread of zero-point wavefunction is much smaller than the tweezer width, indicating that only the first few sidebands are coupled and can be driven efficiently.

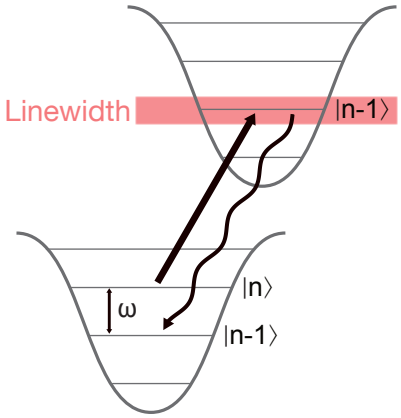

Figure 6.2: Simplest case of sideband cooling in 1D and magic conditions. The cooling laser excites Rabi oscillations coherently between the ground and excited states on the first red sideband $n \rightarrow n-1$. Spontaneous decay, on the other hand, is centered on the $n-1 \rightarrow n-1$ transition, which incoherently transfers the atoms back to the $n-1$ level within the ground state. This effectively cools the atom by the energy of one phonon $\hbar\omega_{trap}$ within the timescale of the exited state lifetime.

Given the parameters shown above, we performed simulations in both directions by considering the simplest 1D magic case as shown in fig. 4.7. In the rotating frame, the Hamiltonian (including both internal and external degrees of freedom) is

$$H = \hbar\omega_{trap}\left(a^{+}a + \frac{1}{2}\right) - \hbar\frac{\delta}{2}\sigma_z + \frac{\hbar\Omega}{2}\left(\sigma_{+}e^{i\eta(a+a^{+})} + \sigma_{-}e^{-i\eta(a+a^{+})}\right)$$

where a, a^{+} are the annihilation and creation operators for the harmonic trap, $\delta = \omega_L - \omega$ and Ω are the detuning and Rabi coupling of the cooling laser, and $\sigma_z = |\, g\rangle\langle g\,| - |\, e\rangle\langle e\,|$, $\sigma_{+} = |\, e\rangle\langle g\,|$ and $\sigma_{-} = |\, g\rangle\langle e\,|$ are the Pauli matrices based on the internal atomic states. Sideband cooling is then described by the master equation:

$$\frac{d\rho}{dt} = -\frac{i}{\hbar}[H,\rho] + L^{d}\rho$$

where the Lindblad operator $L^{d}\rho = \frac{\Gamma}{2}\{2\sigma^{-}\tilde{\rho}\sigma^{+} - \sigma^{+}\sigma^{-}\rho - \rho\sigma^{+}\sigma^{-}\}$ assumes a dipole decay pattern.

Results of the simulations are shown in fig. 6.3, from which we extracted the cooling rates for the transverse and longitudinal directions to be $r_t = 4.23 \times 10^5 E_{\text{recoil},461}/s$ and $r_l = 1.07 \times 10^5 E_{\text{recoil},461}/s$ with the cooling laser parameter optimized for the transverse case. Remarkably, this implies that both directions can be cooled with only one

laser setting close to the theoretically optimal rates $\frac{\Gamma}{2} n\hbar\omega_{trap}$, where $n = 1$ and $n = 7$ for the transverse and longitudinal directions, respectively.

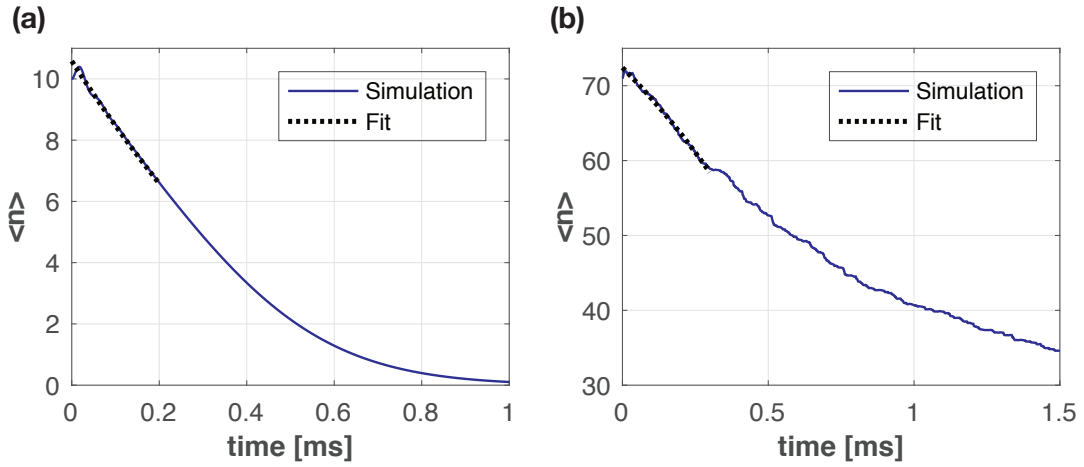

Figure 6.3: Sideband cooling simulations for the simplest 1D magic case in **(a)** transverse and **(b)** longitudinal directions with the same cooling laser parameters $s = 2(\frac{\Omega}{\Gamma})^2 \sim 90$ and $\delta = -203$ kHz (first red sideband), optimized for the cooling rate in the transverse direction. The initial occupation number in the tweezer is chosen for a 0.1 mK atom, or 1/10 of the tweezer depth. The curve in **(b)** is not smooth because the simulation is performed using stochastic wavefunction methods due to the large dimensionality of the Hilbert space. Linear fits to the initial points of both cases yield cooling rates of **(a)** $r_t = 4.23 \times 10^5 E_{\text{recoil},461}/s$ and **(b)** $r_l = 1.07 \times 10^5 E_{\text{recoil},461}/s$.

6.3 Imaging technique

With this cooling method, we aim to realize a robust technique to image strontium while keeping atoms close to the ground state. For this, we keep the ${}^1S_0 \rightarrow {}^3P_1$ transition dedicated for cooling and additionally use on-resonant light that scatters on the ${}^1S_0 \rightarrow {}^1P_1$ transition for the imaging. A sketch of this scheme is shown in fig. [**?**].

The on-resonant light will due to the very high Doppler temperature in a typical envisioned tweezer depth unavoidably heat up the atom. In the regime near to a ground state of a tweezer which has a depth on the order of the depth of the tweezer this leads to a heating rate on the order of $1 - 2\,\frac{E_{\text{recoil}}}{\text{Photon}}$ where the exact heating rate is determined by trap shape of the excited state and how high the scattering rate is compared to the time scale of the trap frequency.

Assuming that to balance the cooling and heating rates with just a classical rate equation gives a good estimation for a possible equilibrium situation(where imaging over a long time period is possible) we can estimate a final photon scattering rate. Using the the maximum heating of $2\,\frac{E_{\text{recoil}}}{\text{Photon}}$ and the smaller cooling rate we calculated for the shallow longitudinal direction of $r_l = 1.07 \times 10^5 E_{recoil,461}/s$ we can a final scatter-

ing rate of blue photons of $f_{sc} = 5.04 \times 10^4$ *Photons*/s. Regarding a typical efficiency of a high resolution imaging system with an NA between 0.5 and 0.7 of $5 - 10\%$ what means still thousands of photons per second are collected. This should enable us imaging of single atoms in tweezers in well below 100 ms with a high possibility to keep the atom on a low trap level inside the trap.

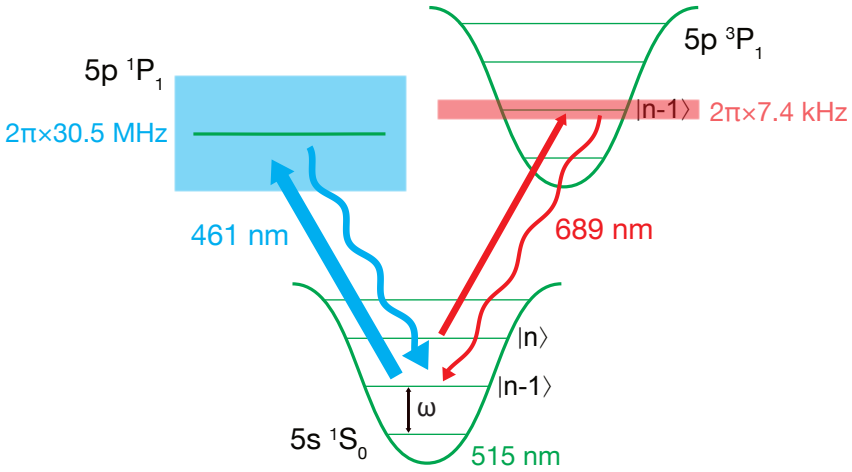

Figure 6.4: Proposed scheme to image single strontium tweezers inside optical tweezers at a wavelength of 515 nm. The tightly-confined tweezer has trap levels higher then the linewidth of the ${}^1S_0 \rightarrow {}^3P_1$ transition. On the ${}^1S_0 \rightarrow {}^1P_1$ transition no trap levels are resolved.

Everything simulated so far is for the 1D case where we demonstrated that for the same detuning for the transversal and longitudinal trap conditions both good cooling can be reached. The next step is to consider the real 2D/3D cases where the coexistence of both trap confinements together with cooling beams with different k-vectors increases the complexity to the simulations. This is the logical next step while on the experimental side we will be able soon to make first investigations on the ${}^1S_0 \rightarrow {}^3P_1$ transition.

7 Results

This chapter presents our initial experimental results taken to characterize the MOT and to image atoms inside the optical tweezers.

In order to run experimental sequences, we use a real-time-based digital-to-analog converter[1], which allows us to generate arbitrary sequences on a computer and interface them with our experiment via TTL pulses and analog outputs. With this, we are not only able to control our laser beams and coils, but also to perform precisely-timed data acquisition. The sequences and the corresponding data is shown in this chapter.

7.1 MOT

After completing the assembly of the laser system shown in section 3 and the vacuum setup shown in section 4, we realized the MOT on the broad ${}^1S_0 \rightarrow {}^1P_1$ transition of ^{88}Sr. An image of a typical MOT is shown in fig. 7.1.

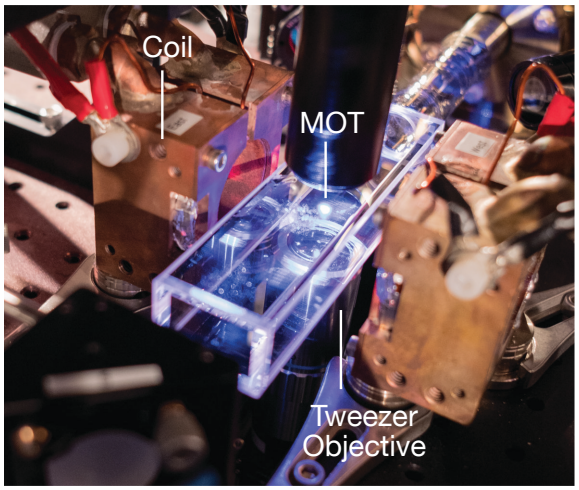

Figure 7.1: Picture of the loaded MOT (with typical parameters that we use) with both repumpers.

In order to perform quantitative analysis of the MOT, we used the imaging system which has been introduced in sec. 4.4. Beginning from the photon collection efficiency (which we already calculated), the final relationship to extract the number of atoms is:

[1] *Jäger GmbH* product series *Adwin pro*

$$N = \frac{\alpha_{\mathrm{CMOS}} N_{\text{Pixel counts}}}{\Gamma_{\mathrm{sc}}(\Delta, S) T_{\mathrm{Exposure}}} \tag{7.1}$$

where α_{CMOS} is the conversion factor previously mentioned, $N_{\mathrm{Pixelcounts}}$ is the pixel counts on the CMOS camera, $\Gamma_{\mathrm{sc}}(\Delta, S)$ is the scattering rate of the atoms in the MOT (for given beam intensities and MOT detuning) and T_{Exposure} is the chosen exposure time of the CMOS.

This can be applied either for global atom counts (by summing over all pixel counts on the camera) or for the spatial resolution as a column density. Using this conversion, all density plots in the following subsections have been calibrated.

7.1.1 Repumpers

After we observed our initial MOT with only 461 nm light, we began optimizing our two repumping lasers. Images of the atom clouds from our imaging system are shown in fig. 7.2 with their total corresponding atom numbers and fitted cloud sizes (shown in table 7.1). The data was taken at an oven temperature of 480° C.

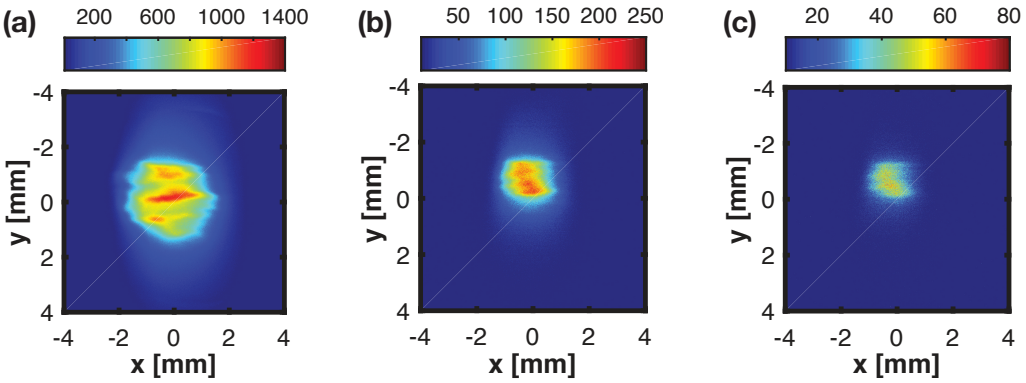

Figure 7.2: Picture of the MOT following sufficient loading time, with different repumper configurations. **(a)** MOT with both repumpers. **(b)** MOT with only the 707 nm repumper. **(c)** MOT without repumpers.

For both repumpers, we observe a significant enhancement in atom numbers within the MOT (at a factor of $\approx 5 \times 10^2$ for the 707 nm repumper and $\approx 1 \times 10^3$ for the 679 nm repumper), as well as in the MOT lifetime (i.e. the amount of time the atoms remain in the trap). We cross-checked this by measuring the decay of atom numbers in the MOTs after switching off both the 2D-MOTs and the Zeeman slower. We measured lifetimes of up to 0.7 s with both repumpers, as well as ≈ 30 ms without. For a naive rate equation describing the MOT (where the rate is simply proportional to the atom number), this corresponds well with our measurements for the number of atoms

observed and the short MOT lifetime of 30 ms, which has also been observed by other groups [45].

	Max. atom number	**Size [mm^2]**
461 nm	5.04×10^6	0.504×0.788
461 nm + 707 nm	1.87×10^7	0.697×0.803
461 nm + 707 nm + 679 nm	1.95×10^8	1.036×1.217

Table 7.1: Comparison between MOT atom numbers and sizes with and without repumpers. The values are evaluated from the fluorescence images shown in fig. 7.2

7.1.2 MOT loading time

For the final experiment, the loading time of the MOT provides an important figure of merit, in which faster rates can significantly accelerate data acquisition during a typical tweezer sequence.

To model the loading time, we assume that the MOT is loaded by a constant flux. By taking into account the decay rate previously discussed, we define a characteristic loading time $N(t) = N_{\max}(1 - e^{-t/\tau})$ where N is the atom number, $N_{\max}$ is the maximum atom number, and τ is the loading time.

In order to measure this, we varied the loading time of the MOT before taking images of the atom cloud. A short exposure time of 0.1 ms was selected to ensure that the imaging time is shorter than the timescale over which loaded atoms leave the MOT (see MOT temperature estimation). The sequence for this is shown in fig. 7.3.

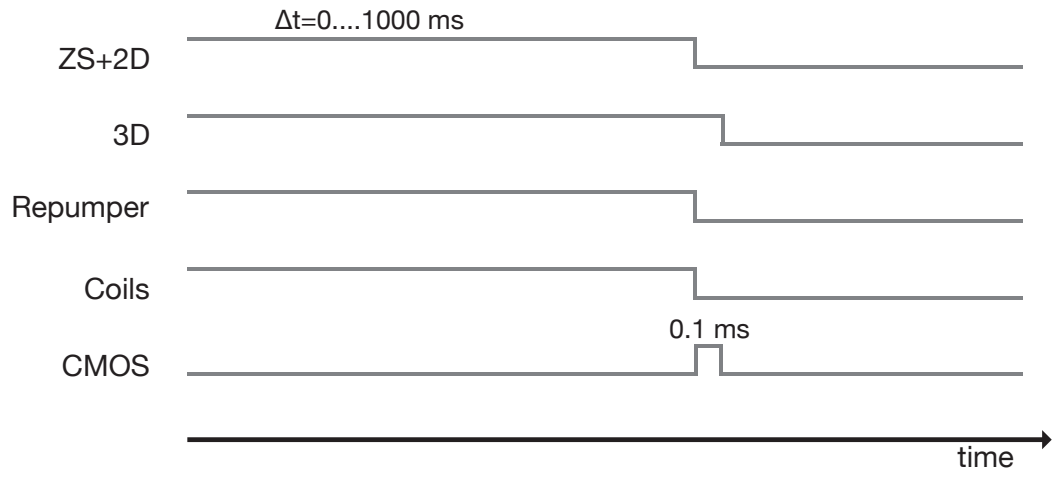

Figure 7.3: Sequence to measure the loading time of the MOT, which is varied between 0 and 1000 ms. The Zeeman slower, 2D MOT and coils are then turned off to prevent further loading. The 3D MOT beams deliver the near-resonant light to observe fluorescence. Following, an image is taken to subtract the background, during which no atoms are loaded (which is not shown in the sequence).

With this method, we measured the loading rates for two oven temperatures at 420 °C and at 480 °C. The data is shown in fig. 7.4.

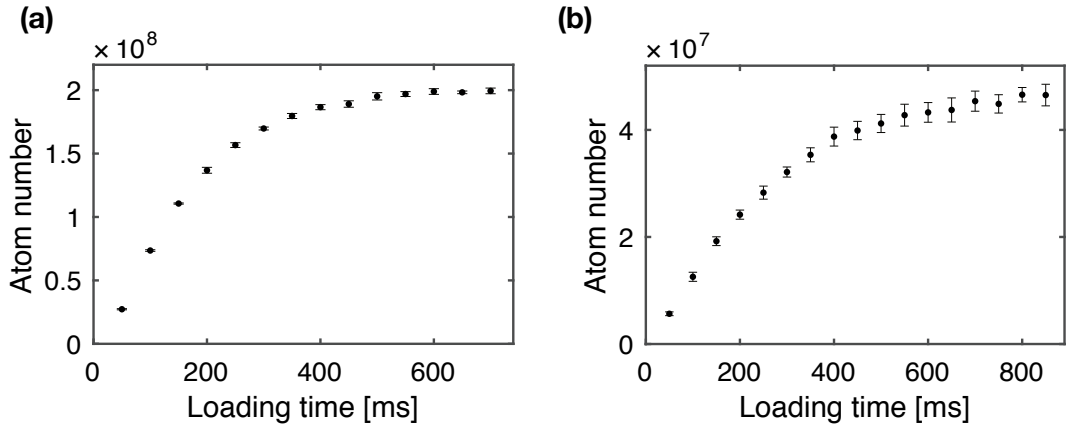

Figure 7.4: Loading curves for the two different oven temperatures **(a)** 420 °C and **(b)** 480 °C. Each data point represents the average over ten realizations. The statistical errors for each point are shown by the error bars.

Following acquisition, the data was fitted to the aforementioned model with $N_{\max}$ as a fixed parameter, and τ as a free parameter. For oven temperatures of 480 °C and 420 °C, this gives us loading rates of (170 ± 3) ms and (260 ± 18) ms, respectively. Here, the given errors are that of the fit. For 420 °C, they are significantly larger due to the smaller atom numbers. Therefore, the absolute shot-to-shot fluctuation of the background counts became subsequently larger. To improve this, however, the exposure time of the camera must be increased, which is not ideal.

As expected, the measurement shows significant changes in loading rates for different oven temperatures. However, since both rates are comparable, whether the enhanced oven temperature is needed will be discussed explicitly in the vacuum lifetime section.

7.1.3 Temperature estimate

In order to estimate the temperature of our MOT, we used a time-of-flight measurement, in which the expansion of an atom cloud depends on the temperature of the gas. With our setup, this is quite challenging since we have the capabilities for fluorescence imaging only, which requires longer exposure times. For MOT temperatures on the order of 1 mK, the expansion velocities (and thus the change in MOT size) are significant during a typical exposure period. For this, we selected the lowest possible exposure time of 0.1 ms. However, this did not allow for investigations into long expansion times due to the low signal-to-noise ratio for the increasingly dilute atom clouds. The sequence is explained in fig. 7.5.

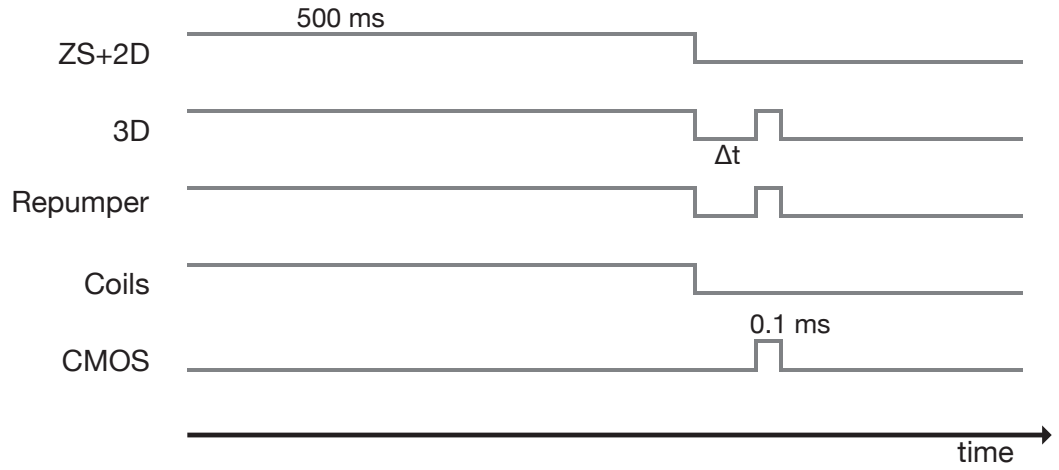

Figure 7.5: Sequence to take time-of-flight images of the MOT. The MOT is released for a time step Δt prior to imaging (while expanding) over an exposure time of 100 μs.

For each single shot of the acquired images, We fit a Gaussian profile to extract the size of the two principle axes of the MOT. Plotted as a function of time, the MOT sizes provide expansion curves which can be modeled as the convolution of the Gaussian at $t = 0$ (from which each point expands isotropically) with a thermal distribution of velocities (whose width evolves with an average velocity of $k_B T/2$). As a result, the width of the convoluted curve follows:

$$\sigma(t) = \sqrt{\sigma_{t=0}^2 + (vt)^2} = \sqrt{\sigma_{t=0}^2 + \frac{k_B T}{m} t^2} \tag{7.2}$$

where $\sigma_{t=0}$ is the initial size of the atom cloud, T is the temperature of the cloud, and m is the mass of a single atom. In the regime of significant expansion, this function is well-approximated by a linear function, where the temperature can be extracted by fitting a linear slope to the tail of the curve:

$$\sigma(t) = \sqrt{\sigma_{t=0}^2 + \frac{k_B T}{m} t^2} \approx \sqrt{\frac{k_B T}{m}} t \tag{7.3}$$

With this model, we evaluated the data that is shown in fig. 7.6 and finally achieve an estimate for the temperature of:

$$T = (1.52 \pm 0.03)\ \text{mK} \tag{7.4}$$

Here, the error is given by the fit and does not reflect the statistical error of the single data points.

This temperature is significantly higher than the Doppler temperature of 753 μK, however, this can be explained with our selected detuning of 25 MHz, which is approximately 10 MHz higher than the ideal detuning of $\Gamma/2$.

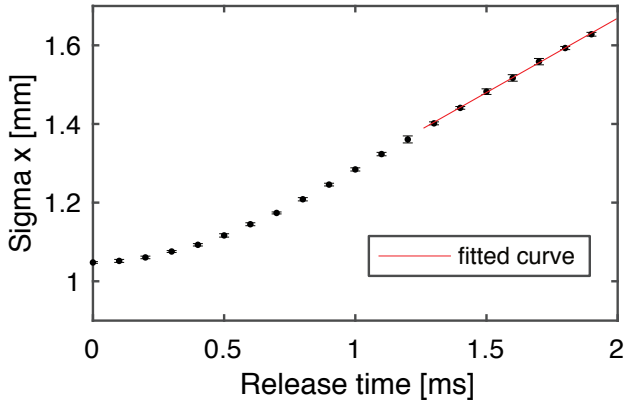

Figure 7.6: Time-of-flight data to measure temperature of the MOT. The y-axis shows one of two principle axes of the 2D Gaussian that is fitted to the MOT images. Each data point represents the average of 10 points, where the error bars are the statistical errors of these 10 measurements.

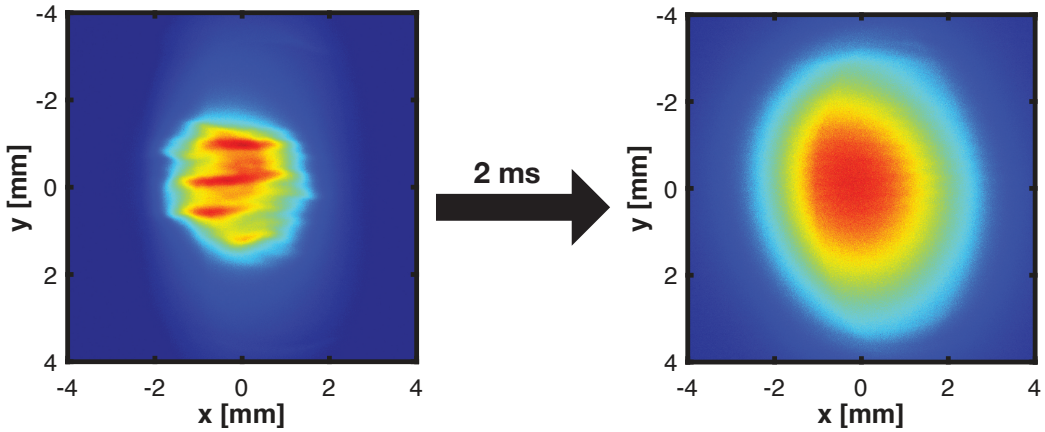

Figure 7.7: Exemplary images of the time-of-flight measurement. The left picture shows the picture of a typical unreleased MOT with a diameter of $\approx$ 1 mm compared to the atom cloud after a two millisecond expansion.

7.1.4 Vacuum lifetime

The final realization of the MOT permits measurements of the vacuum lifetime of the atoms inside the glass cell, which is a relevant figure of merit for our future experiments. Typically, these must be performed in a conservative trap (such as a magnetic trap or an optical dipole trap) in order to overcome the limitation imposed by the lifetime of the MOT itself. Unfortunately, the ground state of ^{88}Sr does not have angular momentum nor spin, and therefore cannot be trapped in a static magnetic field. To

achieve a magnetic trap, however, we make use of the meta-stable states in the triplet manifold. By running the MOT on the ${}^1S_0 \rightarrow {}^1P_1$ transition, we can populate the ${}^3P_2$ state, which is magnetically trapped by the quadrupole field of the MOT. To recapture atoms into the MOT for imaging, we apply the 707 nm laser to repump the atoms to the relevant MOT cycle. This method is shown in ref. [45] and the corresponding sequence is shown in fig. 7.8.

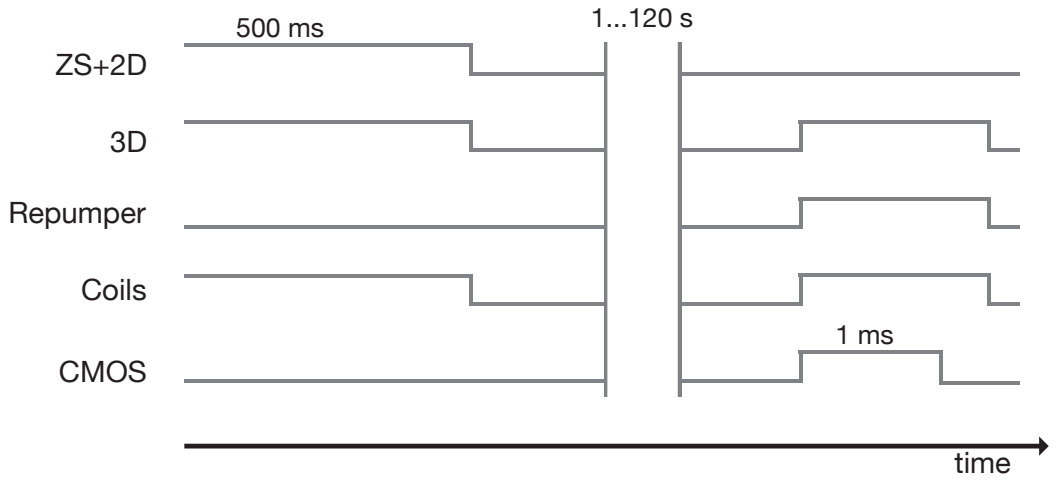

Figure 7.8: Sequence to measure the vacuum lifetime of the atoms in the glass cell. The atoms are optically pumped into the ${}^3P_2$ state by switching off the repumpers. The atoms in this state are then held within the magnetic trap for varying amounts of time. We finally repump them back to the MOT cycle to collect the fluorescence signal, which corresponds to the number of remaining atoms in the ${}^3P_2$ state.

With this method, we were able to compare the vacuum lifetimes for different oven temperatures. We model the decay of the atoms inside the trap with an exponential decay function ($N(t) = N_0 e^{-t/\tau}$). In table 7.2, the measured lifetimes are listed, which were extracted from the decay curves shown in fig. 7.9.

	Vacuum lifetime [s]
480° K	(25.8 ± 1.5)
420° K	(42.5 ± 3.5)

Table 7.2: Comparison between vacuum lifetimes for oven temperatures of 420 °K and 480 °K. The values are extracted from the decay curves shown in fig. 7.2. The given errors are fit errors.

The significant difference between lifetimes measured for the two oven temperatures is contrary to our readings describing the ion pump (i.e. our only direct indication of the vacuum pressure inside the chamber), which should not change for oven temperatures between 420 °K and 480 °K.

Our explanation for this is the underestimation of the pressure in the glass cell, which may be caused by ballistic transport of background pressure through the differential pumping stage between the oven and the main chamber, which has a direct line of sight of the glass cell. Due to the direct stream of atoms into the glass cell, the pumps in the main chamber do not have any effect on these atoms. In principle, this could cause the shorter lifetimes for high oven temperatures. However, for colder oven temperatures, the lifetimes (for which our measurements range from $40 - 60$ s) are likely affected by the loss of atoms from the $^3P_2$ level due to coupling to the 4d $^3D_2$ state via blackbody radiation, which is described in ref. [45]. Here, we are certain that our final lifetimes for cold oven temperatures are on the order of > 60 s. Here, measurements of atom lifetimes in large optical dipole traps could be performed to confirm these values.

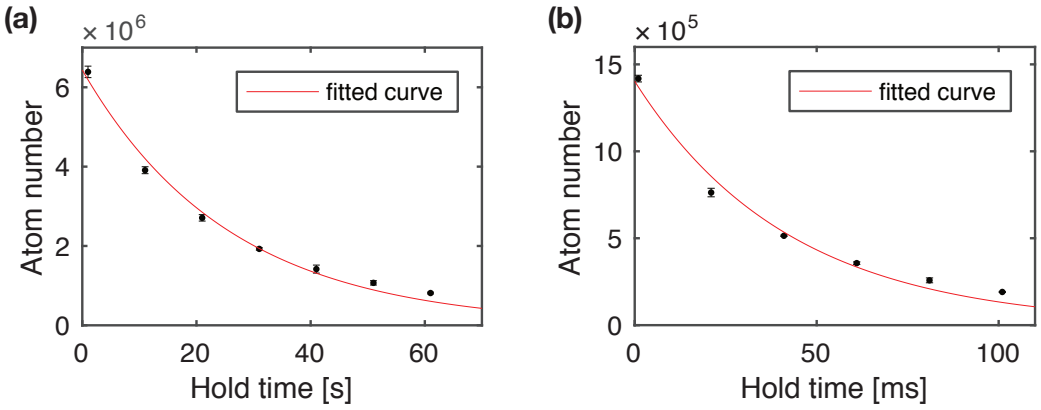

Figure 7.9: Lifetime measurements of atoms in the magnetic trap of the $^3P_2$ state for **(a)** 480 °K and **(b)** 420 °K.

7.2 Imaging Atoms in Tweezers

After characterizing our MOT, we attempted to image atoms in tweezers for the first time. While we have yet to include the 689 nm red system into the optical layout surrounding our glass cell, we hoped to be able to image atoms by loading them from the $^1S_0 \rightarrow {}^1P_1$ blue MOT into deep optical tweezers and using strongly saturated on-resonant $^1S_0 \rightarrow {}^1P_1$ light. This approach is orthogonal to our proposed imaging method in ch. 6, in which we use low saturated blue imaging light while we cool on the $^1S_0 \rightarrow {}^3P_1$ transition to keep the atoms close to the ground state. With this technique, we exploit the broad linewidth of the $^1S_0 \rightarrow {}^1P_1$ MOT where we hope to scatter a sufficient number of photons prior to the atom diffusing out of the volume of the tweezer.

In order to maximize the effective trap depth, we decided to use linear polarization for the trap light with a probe beam that drives only $\sigma^{+/-}$-transitions to prevent from exciting the atoms into the anti-trapped $m = 0$ state (see ch. 6). The sequence we used is shown in fig. 7.10. We load our MOT for a sufficient period of time to ensure we reach the highest possible atom density. During the MOT loading, the tweezer is already switched on. After switching off the MOT beams, we wait a short period time (to avoid imaging the remaining atoms in the MOT) before finally probing atoms with a smaller beam (to avoid stray light on our EMCCD) [2].

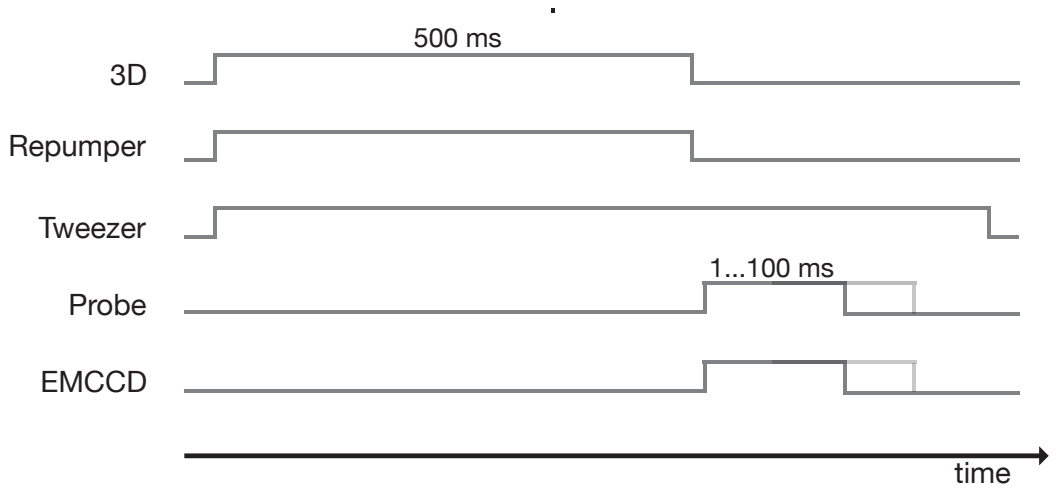

Figure 7.10: Sequence we use to image atoms inside the tweezer. The tweezer is switched on over the entire sequence, while the probe time is varied as a free parameter to be optimized.

We aim to optimize the atom signal in our optical tweezer by varying the saturation of the 461 nm probe beam, the detuning of the probe beam, as well as the exposure time of the camera. For the parameters which were finally selected, the trap depths

[2] *Andor* model *iXon 888*

and the corresponding light shifts were so large (on the order of a few GHz) that it was not practical to adjust the probe light.

By exploring this parameter space, we were able to observe atoms inside the tweezers. A typical single shot image for this is shown in fig. 7.11. In addition, the figure shows a histogram over a sequence of 10,000 repetitions with the same parameters.

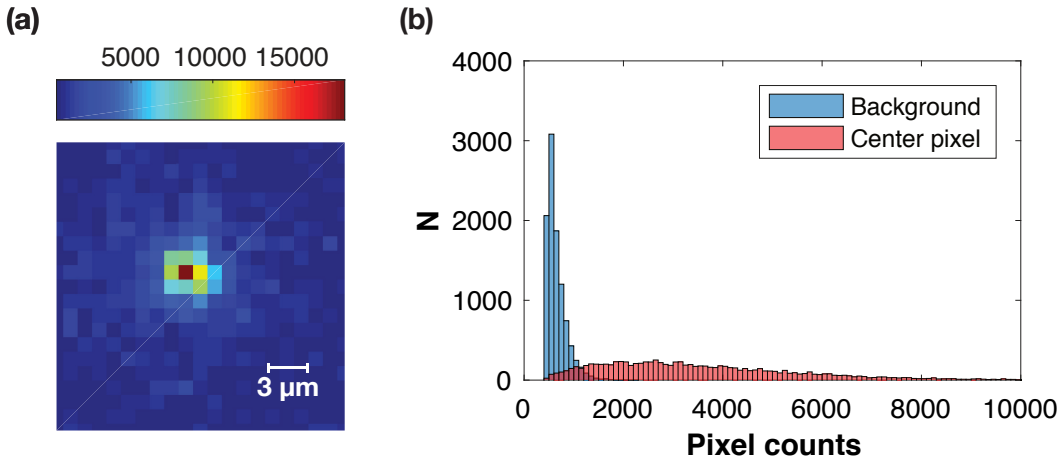

Figure 7.11: **(a)** Single shot image of atoms inside the optical tweezer. The color bar shows counts on the EMMCD camera. **(b)** Histogram with pixel counts over 10,000 realizations of the sequence, where the red bars show the counts of the central pixel of the tweezer compared to the counts of an arbitrary pixel outside of the tweezer in blue.

The parameters which were finally selected include a 432.4 mW tweezer (which corresponds to a trap depth of 892.5 mK for a diffraction-limited tweezer), probe light with a saturation parameter of $\approx 200\ I_{\mathrm{sat}}$, a detuning of the probe light of $+180$ MHz relative to the bare transition, and an exposure time on the camera of 100 ms.

The broad count distribution of the tweezer pixels on the EMCCD along with the high probability of single shot detection of atoms (on the order of 75%, which depends on the selected threshold to distinguish between shots with and without atoms) suggest that we have more than one atom inside the tweezer. The long exposure time that yields the best signal can be interpreted as a result of light shifts that cause significant detuning of atoms from our probe light, where the scattering rates achieved are relatively small. Both of these interpretations require further investigation due to the weak single shot signal, the limitations in the tunability of our probe light, as well as our inability to draw conclusive statements regarding the true trap depth.

This extreme parameter space is very unattractive for future work since the required trap depth does not permit scaling up the size of the system. This did provide, however, a proof-of-principle for our tweezer setup. Our ability to image strontium atoms with a measurable fidelity without cooling provides us with a powerful experimental tool to later optimize our tweezer and the probe beams.

At the 689 nm light, the next logical step is to test our calculated magic wavelength at 515 nm and demonstrate cooling on the $^1S_0 \rightarrow {}^3P_1$ transition. Here, we aim to have a better understanding of the loading mechanism of the optical tweezer. Typically, for alkali atoms (or for the $^1S_0 \rightarrow {}^3P_1$ transition in strontium), the light shifts of the trap light significantly disturbs the MOT within the volume of the tweezer. However, for a magic wavelength, the atom experiences no change in detuning due to the optical tweezer. By adding the 689 nm light to the system, we can determine whether these light shifts are essential in the loading mechanism, whether the microscopic picture is exactly the opposite, and whether a transition that does not experience light shifts could enhance loading. This will be investigated in the near future.

8 Summary

Throughout the course of this work, we designed and built a new experiment towards the realization of defect-free arrays of strontium atoms.

We begin by introducing the basics of laser cooling to motivate our polarizability calculations, which were used to calculate a magic wavelength at around 515 nm.

Taking into account our design considerations, the second part of the thesis provides a detailed overview of our laser systems that were built to cool and trap our atoms, while addressing all the unique features of atomic strontium. Low maintenance is required due to simplifications made to the design of our system, such as omitting absorption spectroscopy of the narrow $^1S_0 \rightarrow {}^3P_1$ transition and using a wavemeter to stabilize our repumping lasers.

Following, we describe how we successfully designed and built our UHV system, where we achieve pressures on order of 10^{-11} mTorr inside the steel chamber. In addition, we measured atom lifetimes of up to 42.5 s, which we believe to be dominated by decay mechanisms other than the vacuum lifetime. As a result, we are capable of performing experiments that are longer than typical tweezer sequences, such as those involving evaporative cooling to prepare degenerate gases.

In order to produce diffraction-limited optical tweezers, we characterized our high resolution objectives as well as our glass cell with a separate setup. Here, we realized tweezers with a waist of 536 nm and a longitudinal confinement of 3.8 μm at our trapping wavelength of 515 nm. We then implemented an AOD into our high resolution system to realize arrays of optical tweezers through multi-tone frequency signals. This will enable the generation of arrays of tens of tweezers at an early stage of the experiment, paving the way for rearrangement within a few milliseconds.

In parallel, we began developing a scheme to implement resolved sideband cooling on the $^1S_0 \rightarrow {}^3P_1$ transition. From this, we found conclusive evidence demonstrating that sideband cooling in the resolved regime is capable of out-performing Doppler cooling on the same transition. This could serve as a method to cool atoms in tweezers during imaging, which ultimately permits imaging on a 100 ms timescale without heating the atoms out of the trap.

Moving forward, we realized our first MOT with ^{88}Sr on the broad $^1S_0 \rightarrow {}^3P_1$ transition in which we achieved a trap with atom numbers of up to 2×10^8 and loading rates of up to 300 ms. The large atom number is a good starting point for future work in which we aim to realize a red MOT on the narrow $^1S_0 \rightarrow {}^3P_1$ transition to reach very low temperatures, which should be favorable to load atoms into tweezers.

Finally, to demonstrate proof-of-principle, we loaded atoms from the MOT into our optical tweezers and imaged them via fluorescence imaging by illuminating them with a near-resonant beam. There, we successfully observed initial signals from atoms, with

a rising signal for increasing trap depths. This provides a platform to implement and demonstrate our proposed cooling strategies, concluding perhaps on the uncertainties in our magic wavelength calculations.

9 Outlook

Our initial results have confirmed our proposed ideas towards the realization of single strontium atoms in optical tweezers. However, this remains only as the starting point in constructing a versatile apparatus, with the ability to generate large arrays of tweezers that allow for unprecedented simulations of interacting spin systems.

In the near future, we aim to realize the next steps to improve upon the experimental apparatus, and to investigate its future prospects. These plans will be outlined in this chapter.

Towards a new setup

With the proof of principle for the coexistence of a large MOT and the two high resolution objectives, we look to implement custom breadboards and coils that will make the full use of this approach. A drawing of the design is shown in fig. 9.1.

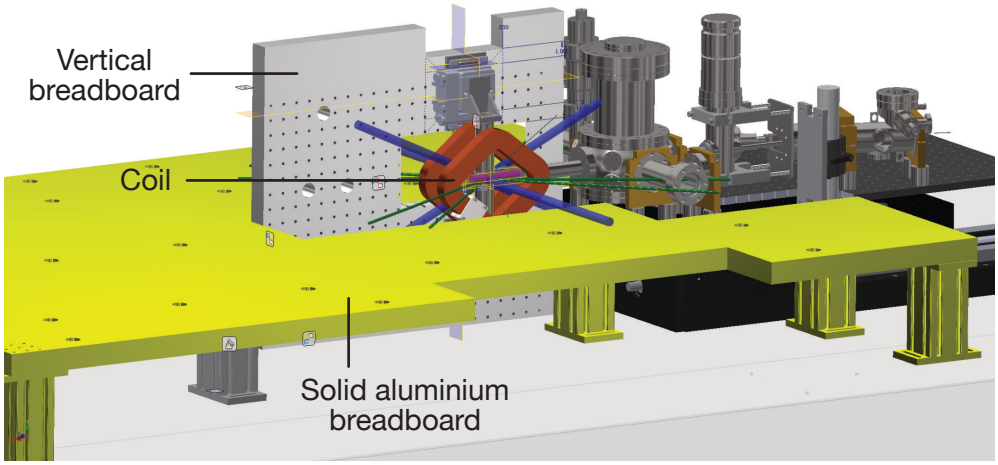

Figure 9.1: Drawing of the core of the future setup with two of the custom breadboards (a third top breadboard has been omitted for simplicity). The preliminary design of the coils is shown together with the essential beams.

Diamond knotted coils that maximize the horizontal optical access to the glass cell will also be implemented. Moving from externally-cooled coils to coils constructed using water-flooded wire, we will be able to generate magnetic fields on the order of 1,000 G. This should enhance our existing toolbox by allowing for e.g. the possibilities to create significant state-mixing within the triplet manifold. This could allow us drive

the transition from $^1S_0$ to $^3P_0$, even within the bosonic isotopes.

Another upgrade will be the integration of customized aluminum breadboards with our existing setup, since a large connected structure will improve the stability. This is especially important for the two high resolution objectives, which are sensitive to changes on the order of 1 μm in absolute distance. Future beams (e.g. additional lattices or longitudinal confinement beams) must be stable with respect to the tweezers.

2D Arrays

To further develop the tweezer technology, we look to extend our current AOD approach to produce tweezers in 2D by using two AODs in an orthogonal configuration. The *Browaeys* group currently uses two crossed AODs to rearrange atoms within a fixed 2D array of tweezers, which they generate using a Spatial Light Modulator (SLM) [27].

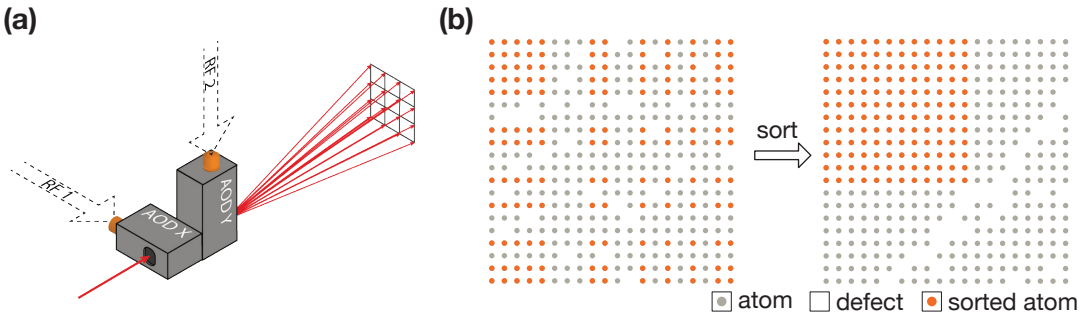

Figure 9.2: a Illustration of tweezer generation with two crossed AODs. **(b)** Example to show rearrangement with two crossed AODs for a 20 × 20 array with an initial filling fraction of 95%. The AOD allows for shifting of rows and columns of tweezers at arbitrary locations, which - in this example - leads to a 12 × 12 array. Shifted atoms are indicated in orange, which lead to the generation of a defect-free sub-array that can be finally used for the experiment.

Since they perform rearrangement in an atom-by-atom fashion by transporting atoms one after another, this technique is finally limited by the vacuum lifetimes of the tweezers. Analogous to our 1D AOD approach, we would overcome this limitation through the use of multi-tone RF signals to realize 2D array of tweezers, which would be rearrangeable in real-time. This could be an exciting extension to the current scheme since the rearrangement process would be extremely fast, however, the shifting operations of our crossed AODs would be limited in comparison to that of the *Browaeys* group. This is illustrated in fig. 9.2.

An alternative way to make use of this multi-tone approach could involve a static array of tweezers created by e.g. an SLM, while rearrangement is performed with two crossed AODs to manipulate entire rows or small blocks. This allows for the freedom of the presented scheme in ref. [27], but with a reduction in the number of rear-

rangement steps. This could accelerate the rearrangement process significantly, which enables scaling up to larger array sizes without the limitation of vacuum lifetimes.

Rydberg Interactions

To introduce interactions between the neutral atoms, we want to excite atoms to Rydberg states to exploit the strong dipole-dipole interactions between them [85]. As demonstrated with QGMs [86] and most recently with large tweezer systems [29, 87], it is possible to simulate coherent evolution of strongly correlated spin systems. With further improvements in control, coherence and read-out fidelities, this could become a powerful tool to explore spin dynamics in the context of quantum magnetism, or even to carry out gate operations towards Rydberg-based quantum computing [88].

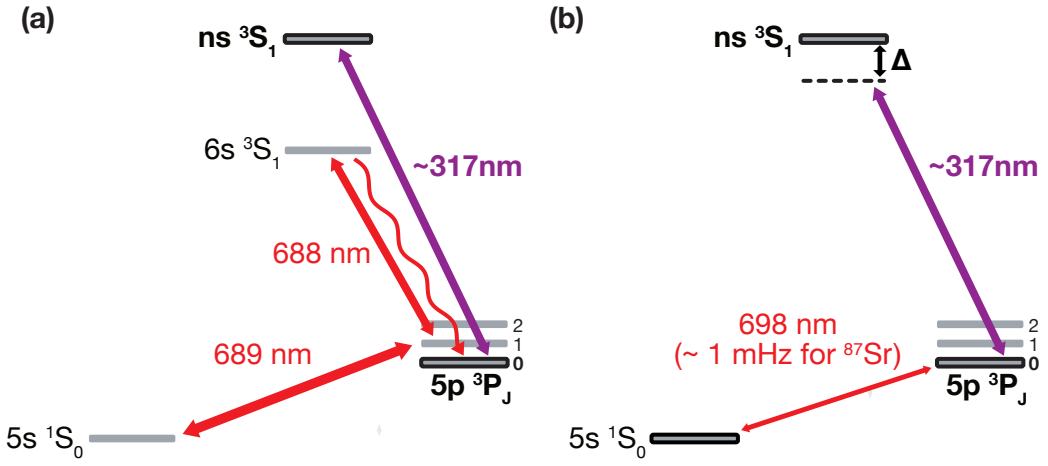

Figure 9.3: **(a)** Scheme to pump ground state atoms into the metastable $^3P_0$ state, to use as a starting point for on-resonant Rydberg excitations into the $ns\ ^3S_1$ manifold. **(b)** Alternative scheme in which transitions between $^1S_0$ and $^3P_0$ occur via either the naturally-emerging transition in the fermionic isotope, or actively introduced state-mixing with magnetic fields. The $^3P_0$ state will be dressed to a state in the $ns\ ^3S_1$ manifold to introduce interactions.

To realize this with strontium, we outline two main schemes that are shown in fig. 9.3. The greatest appeal in the level structure of strontium lies in the following: starting from the triplet manifold, the Rydberg states of the $ns\ ^3S_1$ manifold can be reached with single photon transitions at wavelengths of approximately $317 - 321$ nm, which lie within a range at which powerful laser systems can be built based on third or fouth harmonic generation [89]. This allows for large coupling strengths in comparison to widely used two-photon schemes in Alkali atoms.

With these transitions, we must first explore schemes in which we transfer bosonic strontium atoms inside the tweezers to the $^3P_0$ state via optical pumping, which is

required to be able to drive resonant excitations to the Rydberg states. This effective two-level system in an externally-driven laser field leads to effective spin models [88].

Alternatively, we could also investigate Rydberg dressing [90], in which the relevant transition is from the ground state $^1S_0$ to the clock state $^3P_0$, and the interaction is induced by adding an off-resonant laser field that induces a state admixture to the Rydberg states. This could be especially interesting as an extension to the typical Ramsey sequence used for optical clocks as proposed in ref. [91].

10 Bibliography

[1] J Ignacio Cirac and Peter Zoller. Goals and opportunities in quantum simulation. *Nature Physics*, 8(4):264–266, 2012.

[2] Rainer Blatt and Christian F Roos. Quantum simulations with trapped ions. *Nature Physics*, 8(4):277–284, 2012.

[3] Andrew A Houck, Hakan E Türeci, and Jens Koch. On-chip quantum simulation with superconducting circuits. *Nature Physics*, 8(4):292–299, 2012.

[4] Immanuel Bloch, Jean Dalibard, and Sylvain Nascimbene. Quantum simulations with ultracold quantum gases. *Nature Physics*, 8(4):267–276, 2012.

[5] Andreas Wallraff, David I Schuster, Alexandre Blais, L Frunzio, R-S Huang, J Majer, S Kumar, Steven M Girvin, and Robert J Schoelkopf. Strong coupling of a single photon to a superconducting qubit using circuit quantum electrodynamics. *Nature*, 431(7005):162–167, 2004.

[6] L DiCarlo, JM Chow, JM Gambetta, Lev S Bishop, BR Johnson, DI Schuster, J Majer, A Blais, L Frunzio, SM Girvin, et al. Demonstration of two-qubit algorithms with a superconducting quantum processor. *Nature*, 460(7252):240–244, 2009.

[7] S Nadj-Perge, SM Frolov, EPAM Bakkers, and Leo P Kouwenhoven. Spin-orbit qubit in a semiconductor nanowire. *Nature*, 468(7327):1084–1087, 2010.

[8] Ferdinand Schmidt-Kaler, Hartmut Häffner, Mark Riebe, Stephan Gulde, Gavin PT Lancaster, Thomas Deuschle, Christoph Becher, Christian F Roos, Jürgen Eschner, and Rainer Blatt. Realization of the cirac–zoller controlled-not quantum gate. *Nature*, 422(6930):408–411, 2003.

[9] Dietrich Leibfried, Rainer Blatt, Christopher Monroe, and David Wineland. Quantum dynamics of single trapped ions. *Reviews of Modern Physics*, 75(1):281, 2003.

[10] Diego Porras and J Ignacio Cirac. Effective quantum spin systems with trapped ions. *Physical review letters*, 92(20):207901, 2004.

[11] Ben P Lanyon, C Hempel, D Nigg, Markus Müller, R Gerritsma, F Zähringer, P Schindler, JT Barreiro, M Rambach, G Kirchmair, et al. Universal digital quantum simulation with trapped ions. *Science*, 334(6052):57–61, 2011.

[12] Kendall B Davis, M-O Mewes, Michael R Andrews, NJ Van Druten, DS Durfee,

DM Kurn, and Wolfgang Ketterle. Bose-einstein condensation in a gas of sodium atoms. *Physical review letters*, 75(22):3969, 1995.

[13] Mike H Anderson, Jason R Ensher, Michael R Matthews, Carl E Wieman, Eric A Cornell, et al. Observation of bose-einstein condensation in a dilute atomic vapor. *science*, 269(5221):198–201, 1995.

[14] Franco Dalfovo, Stefano Giorgini, Lev P Pitaevskii, and Sandro Stringari. Theory of bose-einstein condensation in trapped gases. *Reviews of Modern Physics*, 71(3):463, 1999.

[15] Markus Greiner, Olaf Mandel, Tilman Esslinger, Theodor W Hänsch, and Immanuel Bloch. Quantum phase transition from a superfluid to a mott insulator in a gas of ultracold atoms. *nature*, 415(6867):39–44, 2002.

[16] U Schneider, L Hackermüller, S Will, Th Best, Immanuel Bloch, TA Costi, RW Helmes, D Rasch, and A Rosch. Metallic and insulating phases of repulsively interacting fermions in a 3d optical lattice. *Science*, 322(5907):1520–1525, 2008.

[17] Waseem S Bakr, Jonathon I Gillen, Amy Peng, Simon Fölling, and Markus Greiner. A quantum gas microscope for detecting single atoms in a hubbard-regime optical lattice. *Nature*, 462(7269):74–77, 2009.

[18] Jacob F Sherson, Christof Weitenberg, Manuel Endres, Marc Cheneau, Immanuel Bloch, and Stefan Kuhr. Single-atom-resolved fluorescence imaging of an atomic mott insulator. *Nature*, 467(7311):68–72, 2010.

[19] Anton Mazurenko, Christie S Chiu, Geoffrey Ji, Maxwell F Parsons, Márton Kanász-Nagy, Richard Schmidt, Fabian Grusdt, Eugene Demler, Daniel Greif, and Markus Greiner. A cold-atom fermi–hubbard antiferromagnet. *Nature*, 545(7655):462–466, 2017.

[20] M Eric Tai, Alexander Lukin, Matthew Rispoli, Robert Schittko, Tim Menke, Dan Borgnia, Philipp M Preiss, Fabian Grusdt, Adam M Kaufman, and Markus Greiner. Microscopy of the interacting harper–hofstadter model in the two-body limit. *Nature*, 546(7659):519–523, 2017.

[21] Adam M Kaufman, Brian J Lester, and Cindy A Regal. Cooling a single atom in an optical tweezer to its quantum ground state. *Physical Review X*, 2(4):041014, 2012.

[22] AM Kaufman, BJ Lester, M Foss-Feig, ML Wall, AM Rey, and CA Regal. Entangling two transportable neutral atoms via local spin exchange. *Nature*, 527(7577):208–211, 2015.

[23] Simon Murmann, Andrea Bergschneider, Vincent M Klinkhamer, Gerhard Zürn, Thomas Lompe, and Selim Jochim. Two fermions in a double well: Exploring a fundamental building block of the hubbard model. *Physical review letters*, 114(8):080402, 2015.

[24] Daniel Barredo, Henning Labuhn, Sylvain Ravets, Thierry Lahaye, Antoine Browaeys, and Charles S Adams. Coherent excitation transfer in a spin chain of three rydberg atoms. *Physical review letters*, 114(11):113002, 2015.

[25] Nicolas Schlosser, Georges Reymond, Igor Protsenko, and Philippe Grangier. Sub-poissonian loading of single atoms in a microscopic dipole trap. *Nature a-z index*, 411(6841):1024–1027, 2001.

[26] Brian J Lester, Niclas Luick, Adam M Kaufman, Collin M Reynolds, and Cindy A Regal. Rapid production of uniformly filled arrays of neutral atoms. *Physical review letters*, 115(7):073003, 2015.

[27] Daniel Barredo, Sylvain de Léséleuc, Vincent Lienhard, Thierry Lahaye, and Antoine Browaeys. An atom-by-atom assembler of defect-free arbitrary two-dimensional atomic arrays. *Science*, 354(6315):1021–1023, 2016.

[28] Manuel Endres, Hannes Bernien, Alexander Keesling, Harry Levine, Eric R Anschuetz, Alexandre Krajenbrink, Crystal Senko, Vladan Vuletic, Markus Greiner, and Mikhail D Lukin. Atom-by-atom assembly of defect-free one-dimensional cold atom arrays. *Science*, page aah3752, 2016.

[29] Hannes Bernien, Sylvain Schwartz, Alexander Keesling, Harry Levine, Ahmed Omran, Hannes Pichler, Soonwon Choi, Alexander S Zibrov, Manuel Endres, Markus Greiner, et al. Probing many-body dynamics on a 51-atom quantum simulator. *Nature*, 551(7682):579, 2017.

[30] Hidetoshi Katori, Koji Hashiguchi, E Yu Il'inova, and VD Ovsiannikov. Magic wavelength to make optical lattice clocks insensitive to atomic motion. *Physical review letters*, 103(15):153004, 2009.

[31] Masao Takamoto, Feng-Lei Hong, Ryoichi Higashi, and Hidetoshi Katori. An optical lattice clock. *Nature*, 435(7040):321–324, 2005.

[32] YY Jiang, AD Ludlow, Nathan D Lemke, Richard W Fox, Jeffrey A Sherman, L-S Ma, and Christopher W Oates. Making optical atomic clocks more stable with 10-16-level laser stabilization. *Nature Photonics*, 5(3):158–161, 2011.

[33] BJ Bloom, TL Nicholson, JR Williams, SL Campbell, M Bishof, X Zhang, W Zhang, SL Bromley, and J Ye. An optical lattice clock with accuracy and stability at the 10-18 level. *Nature*, 506(7486):71–75, 2014.

[34] Andrew J Daley, Martin M Boyd, Jun Ye, and Peter Zoller. Quantum computing with alkaline-earth-metal atoms. *Physical review letters*, 101(17):170504, 2008.

[35] William D. Phillips. Nobel lecture: Laser cooling and trapping of neutral atoms. *Rev. Mod. Phys.*, 70:721–741, Jul 1998.

[36] David J Wineland and Wayne M Itano. Laser cooling of atoms. *Physical Review A*, 20(4):1521, 1979.

[37] Brian Harold Bransden and Charles Jean Joachain. *Physics of atoms and molecules*. Pearson Education India, 2003.

[38] Harold J Metcalf and Peter Van der Straten. *Laser cooling and trapping*. Springer Science & Business Media, 2012.

[39] Y Castin, H Wallis, and Jean Dalibard. Limit of doppler cooling. *JOSA B*, 6(11):2046–2057, 1989.

[40] Steven Chu, L. Hollberg, J. E. Bjorkholm, Alex Cable, and A. Ashkin. Three-dimensional viscous confinement and cooling of atoms by resonance radiation pressure. *Phys. Rev. Lett.*, 55:48–51, Jul 1985.

[41] E. L. Raab, M. Prentiss, Alex Cable, Steven Chu, and D. E. Pritchard. Trapping of neutral sodium atoms with radiation pressure. *Phys. Rev. Lett.*, 59:2631–2634, Dec 1987.

[42] William D Phillips and Harold Metcalf. Laser deceleration of an atomic beam. *Physical Review Letters*, 48(9):596, 1982.

[43] K. Dieckmann, R. J. C. Spreeuw, M. Weidemüller, and J. T. M. Walraven. Two-dimensional magneto-optical trap as a source of slow atoms. *Phys. Rev. A*, 58:3891–3895, Nov 1998.

[44] Rudolf Grimm, Matthias Weidemüller, and Yurii B Ovchinnikov. Optical dipole traps for neutral atoms. *Advances in atomic, molecular, and optical physics*, 42:95–170, 2000.

[45] Simon Stellmer. *Degenerate gases of Strontium*. PhD thesis, 2013.

[46] Alexey Vyacheslavovich Gorshkov, M Hermele, V Gurarie, C Xu, Paul S Julienne, J Ye, Peter Zoller, Eugene Demler, Mikhail D Lukin, and AM Rey. Two-orbital su (n) magnetism with ultracold alkaline-earth atoms. *Nature physics*, 6(4):289–295, 2010.

[47] Hidetoshi Katori, Tetsuya Ido, Yoshitomo Isoya, and Makoto Kuwata-Gonokami. Magneto-optical trapping and cooling of strontium atoms down to the photon recoil temperature. *Physical Review Letters*, 82(6):1116, 1999.

[48] Simon Stellmer, Benjamin Pasquiou, Rudolf Grimm, and Florian Schreck. Laser cooling to quantum degeneracy. *Physical review letters*, 110(26):263003, 2013.

[49] Martin M. Boyd. *High Precision Spectroscopy of Strontium in an Optical Lattice: Towards a New Standard for Frequency and Time*. PhD thesis, 2002.

[50] Christopher B. Osborn. *The Physics of Ultracold Sr2 Molecules: Optical Production and Precision Measurement*. PhD thesis, 2013.

[51] Thomas H Loftus, Tetsuya Ido, Martin M Boyd, Andrew D Ludlow, and Jun Ye. Narrow line cooling and momentum-space crystals. *Physical Review A*, 70(6):063413, 2004.

[52] Takashi Mukaiyama, Hidetoshi Katori, Tetsuya Ido, Ying Li, and Makoto Kuwata-Gonokami. Recoil-limited laser cooling of s r 87 atoms near the fermi temperature. *Physical review letters*, 90(11):113002, 2003.

[53] Andrew D Ludlow, T Zelevinsky, GK Campbell, S Blatt, MM Boyd, Marcio HG de Miranda, MJ Martin, JW Thomsen, Seth M Foreman, Jun Ye, et al. Sr lattice clock at $1\times$ 10–16 fractional uncertainty by remote optical evaluation with a ca clock. *Science*, 319(5871):1805–1808, 2008.

[54] Xiaoji Zhou, Xia Xu, Xuzong Chen, and Jingbiao Chen. Magic wavelengths for terahertz clock transitions. *Physical Review A*, 81(1):012115, 2010.

[55] JE Sansonetti. Wavelengths, transition probabilities, and energy levels for the spectra of strontium ions (sr ii through sr xxxviii). *Journal of Physical and Chemical Reference Data*, 41(1):013102–013102, 2012.

[56] WH Parkinson, EM Reeves, and FS Tomkins. Neutral calcium, strontium and barium: determination of f values of the principal series by the hook method. *Journal of Physics B: Atomic and Molecular Physics*, 9(2):157, 1976.

[57] WRS Garton, JP Connerade, MA Baig, J Hormes, and B Alexa. Measurement of oscillator strengths in the ultraviolet by magneto-optical rotation. *Journal of Physics B: Atomic and Molecular Physics*, 16(3):389, 1983.

[58] HGC Werij, Chris H Greene, CE Theodosiou, and Alan Gallagher. Oscillator strengths and radiative branching ratios in atomic sr. *Physical Review A*, 46(3):1248, 1992.

[59] Tetsuya Ido, Yoshitomo Isoya, and Hidetoshi Katori. Optical-dipole trapping of sr atoms at a high phase-space density. *Physical Review A*, 61(6):061403, 2000.

[60] JP Connerade, MA Baig, and M Sweeney. Many-body effects in the 4p spectrum of strontium. *Journal of Physics B: Atomic, Molecular and Optical Physics*, 23(4):713, 1990.

[61] J. D. Thompson, T. G. Tiecke, A. S. Zibrov, V. Vuletić, and M. D. Lukin. Coherence and raman sideband cooling of a single atom in an optical tweezer. *Phys. Rev. Lett.*, 110:133001, Mar 2013.

[62] U Schünemann, H Engler, R Grimm, M Weidemüller, and M Zielonkowski. Simple scheme for tunable frequency offset locking of two lasers. *Review of Scientific Instruments*, 70(1):242–243, 1999.

[63] Yosuke Shimada, Yuko Chida, Nozomi Ohtsubo, Takatoshi Aoki, Makoto Takeuchi, Takahiro Kuga, and Yoshio Torii. A simplified 461-nm laser system using blue laser diodes and a hollow cathode lamp for laser cooling of sr. *Review of Scientific Instruments*, 84(6):063101, 2013.

[64] CJH Pagett, PH Moriya, R Celistrino Teixeira, RF Shiozaki, M Hemmerling, and Ph W Courteille. Injection locking of a low cost high power laser diode at 461 nm. *Review of Scientific Instruments*, 87(5):053105, 2016.

[65] CR Vidal and J Cooper. Heat-pipe oven: A new, well-defined metal vapor device for spectroscopic measurements. *Journal of Applied Physics*, 40(8):3370–3374, 1969.

[66] RWP Drever, John L Hall, FV Kowalski, J_ Hough, GM Ford, AJ Munley, and H Ward. Laser phase and frequency stabilization using an optical resonator. *Applied Physics B*, 31(2):97–105, 1983.

[67] Francisco Camargo. *Rydberg Molecules and Polarons in Ultracold Strontium Gases*. PhD thesis, 2017.

[68] Ingo Nosske, Luc Couturier, Fachao Hu, Canzhu Tan, Chang Qiao, Jan Blume, YH Jiang, Peng Chen, and Matthias Weidemüller. Two-dimensional magneto-optical trap as a source for cold strontium atoms. *Physical Review A*, 96(5):053415, 2017.

[69] Matthew A Norcia and James K Thompson. Simple laser stabilization to the strontium 88sr transition at 707 nm. *Review of Scientific Instruments*, 87(2):023110, 2016.

[70] Kai Bongs, Yeshpal Singh, Lyndsie Smith, Wei He, Ole Kock, Dariusz Świerad, Joshua Hughes, Stephan Schiller, Soroosh Alighanbari, Stefano Origlia, et al. Development of a strontium optical lattice clock for the soc mission on the iss. *Comptes Rendus Physique*, 16(5):553–564, 2015.

[71] Janis Alnis, Arthur Matveev, Nikolai Kolachevsky, Th Udem, and TW Hänsch. Subhertz linewidth diode lasers by stabilization to vibrationally and thermally compensated ultralow-expansion glass fabry-pérot cavities. *Physical Review A*, 77(5):053809, 2008.

[72] GD Miller, RG Batchko, WM Tulloch, DR Weise, MM Fejer, and RL Byer. 42%-efficient single-pass cw second-harmonic generation in periodically poled lithium niobate. *Optics letters*, 22(24):1834–1836, 1997.

[73] Michael Gregory Pullen, Justin James Chapman, and Dave Kielpinski. Efficient generation of> 2 w of green light by single-pass frequency doubling in ppmgln. *Applied optics*, 47(10):1397–1400, 2008.

[74] M Bernardini, S Braccini, R De Salvo, A Di Virgilio, A Gaddi, A Gennai, G Genuini, A Giazotto, G Losurdo, HB Pan, et al. Air bake-out to reduce hydrogen outgassing from stainless steel. *Journal of Vacuum Science & Technology A: Vacuum, Surfaces, and Films*, 16(1):188–193, 1998.

[75] Kevin Chen. *Constructing a One-Dimensional Array of Optical Tweezers for Trapping Single Strontium Atoms*. Senior thesis, Caltech, 2017.

[76] Yvan RP Sortais, H Marion, C Tuchendler, AM Lance, M Lamare, P Fournet, C Armellin, R Mercier, G Messin, A Browaeys, et al. Diffraction-limited optics for single-atom manipulation. *Physical Review A*, 75(1):013406, 2007.

[77] Adam Kaufman. *Laser cooling atoms to indistinguishability: Atomic Hong-Ou-Mandel interference and entanglement through spin exchange*. PhD thesis, 2015.

[78] AW Warner, DL White, and WA Bonner. Acousto-optic light deflectors using optical activity in paratellurite. *Journal of Applied Physics*, 43(11):4489–4495, 1972.

[79] T Yano, M Kawabuchi, A Fukumoto, and A Watanabe. Teo2 anisotropic bragg light deflector without midband degeneracy. *Applied Physics Letters*, 26(12):689–691, 1975.

[80] Z Hu and HJ Kimble. Observation of a single atom in a magneto-optical trap. *Optics letters*, 19(22):1888–1890, 1994.

[81] Lawrence W Cheuk, Matthew A Nichols, Melih Okan, Thomas Gersdorf, Vinay V Ramasesh, Waseem S Bakr, Thomas Lompe, and Martin W Zwierlein. Quantum-gas microscope for fermionic atoms. *Physical review letters*, 114(19):193001, 2015.

[82] Maxwell F. Parsons, Florian Huber, Anton Mazurenko, Christie S. Chiu, Widagdo Setiawan, Katherine Wooley-Brown, Sebastian Blatt, and Markus Greiner. Site-resolved imaging of fermionic ^{6}Li in an optical lattice. *Phys. Rev. Lett.*, 114:213002, May 2015.

[83] Ryuta Yamamoto, Jun Kobayashi, Takuma Kuno, Kohei Kato, and Yoshiro Takahashi. An ytterbium quantum gas microscope with narrow-line laser cooling. *New Journal of Physics*, 18(2):023016, 2016.

[84] Ch Monroe, DM Meekhof, BE King, Steven R Jefferts, Wayne M Itano, David J Wineland, and P Gould. Resolved-sideband raman cooling of a bound atom to the 3d zero-point energy. *Physical Review Letters*, 75(22):4011, 1995.

[85] E Urban, Todd A Johnson, T Henage, L Isenhower, DD Yavuz, TG Walker, and

M Saffman. Observation of rydberg blockade between two atoms. *Nature Physics*, 5(2):110–114, 2009.

[86] Peter Schauß, Marc Cheneau, Manuel Endres, Takeshi Fukuhara, Sebastian Hild, Ahmed Omran, Thomas Pohl, Christian Gross, Stefan Kuhr, and Immanuel Bloch. Observation of spatially ordered structures in a two-dimensional rydberg gas. *Nature*, 491(7422):87–91, 2012.

[87] Vincent Lienhard, Sylvain de Léséleuc, Daniel Barredo, Thierry Lahaye, Antoine Browaeys, Michael Schuler, Louis-Paul Henry, and Andreas M Läuchli. Observing the space-and time-dependent growth of correlations in dynamically tuned synthetic ising antiferromagnets. *arXiv preprint arXiv:1711.01185*, 2017.

[88] Hendrik Weimer, Markus Müller, Igor Lesanovsky, Peter Zoller, and Hans Peter Büchler. A rydberg quantum simulator. *arXiv preprint arXiv:0907.1657*, 2009.

[89] Jieying Wang, Jiandong Bai, Jun He, and Junmin Wang. Development and characterization of a 2.2 w narrow-linewidth 318.6 nm ultraviolet laser. *JOSA B*, 33(10):2020–2025, 2016.

[90] G Pupillo, A Micheli, M Boninsegni, I Lesanovsky, and P Zoller. Strongly correlated gases of rydberg-dressed atoms: quantum and classical dynamics. *Physical review letters*, 104(22):223002, 2010.

[91] LIR Gil, R Mukherjee, EM Bridge, MPA Jones, and T Pohl. Spin squeezing in a rydberg lattice clock. *Physical review letters*, 112(10):103601, 2014.

Acknowledgments

Fist of all, I would like to thank Prof. Manuel Endres. He gave me in the framework of this Master thesis the chance to become a full member of his research group. Starting from my first day he gave me the same trust and responsibility as I was a PhD student which enabled me the great opportunity to learn about all the aspects of building a new cold atom experiment. His great confidence in us while being an infinite source of new ideas and answers is one of the main reasons we reached all the results presented in this thesis. I also want to thank him especially for his helpful advices in- and outside the lab which always helped me to stay on the right track on my way to become a responsible physicist.

Here I also want to thank Prof. Markus Oberthaler who gave me the selfless chance to go on this journey by taking the full responsibility of this project.

All the results shown in this thesis were the result of the great team work of our group. Here I want to thank especially:

Alexandre, for his tireless work attitude that motivated all of us in the lab together with his skill to think outside the box which always brought new ideas to our lab. I always enjoyed his positiveness and his thirst of knowledge, which finally helped anyone in the lab to stay updated in topics like block chain currencies and machine learning.

Ivaylo, for the time where we wore daily hair nets and multiple gloves to built our vacuum setup and he teached me everything I have to know about vacuum hardware. Besides that he gave me the chance to work with an brilliant mind that never stopped questioning what we but especially what he is doing, what always inspired me.

Zeren, for the endless discussions about the right way to built optical setups and the persistance to find answers to arbitrary hard questions. Her curiosity about every small detail of our experiment helped my own understanding of our experiment a lot.

Brian, for his unique humor which always made it fun to work with you while he also found amazingly fast into our team and his contributions are already indispensable for our experiment. I also thank him for introducing me into the world of titanium camping equipment, which gave me completely new possibilites for my camping trips.

Jacob, for his immediate enrichement of our group and for all the answers to my questions about cold atoms. He joined our team directly as a leader and I am sure this will not be the last experiment he will lead.

Emily, for being an oustanding tweezer uniformizer and a nice lab partner with who I shared the last weeks of my stay at the lab. I want to thank your for your selfless help to correct my english and I feel sorry for all your desperate tries to teach me proper

english. Besides your help with my thesis you also made the time of writing this thesis with all the fancy food and boba milk tea much more enjoyable.

In the end I also want to thank Loly - the true backbone of our lab. Without her patience to teach us how to use the caltech buying system properly and the hundreds of orders she had to make for us she was a big part of our success.